

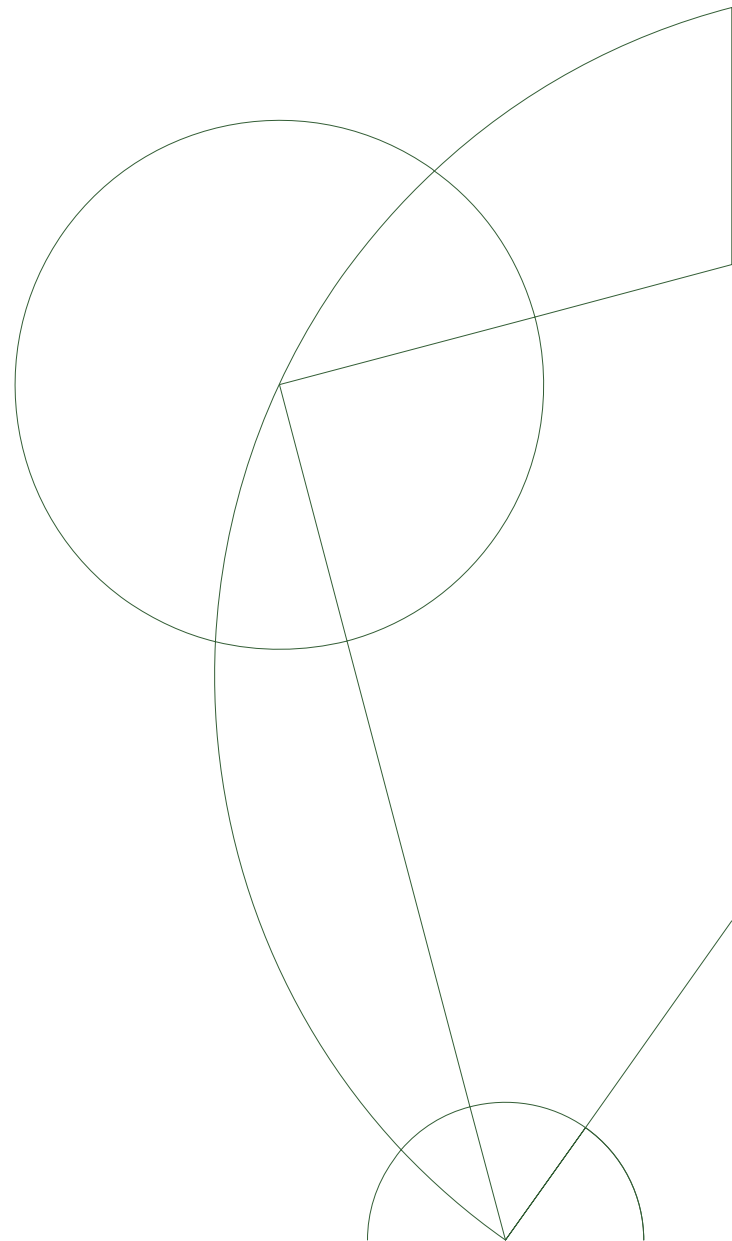


Master thesis

Christine Overgaard Rasmussen

Next-to-leading order matrix element reweighting

A study on $q\bar{q} \rightarrow ZZ \rightarrow e^+e^-\mu^+\mu^-$



Academic Advisor: Jørgen Beck Hansen

August 9, 2013

Contents

Abstract	a
Dansk resumé	b
1 Introduction	1
1.1 Physics teaser	1
1.2 Thesis teaser	2
1.3 Units	2
2 Theory	4
2.1 Basics of quantum field theory	5
2.1.1 Symmetries of a quantum field theory	8
2.1.2 Building a model: The Yang-Mills lagrangian	8
2.1.3 Calculating amplitudes and cross sections	11
2.2 The Standard Model of Particle Physics	12
2.2.1 Particle content	13
2.2.2 Symmetries of the Standard Model	14
2.2.3 Quantum Chromo Dynamics	14
2.2.4 Electroweak theory	15
2.2.5 Electroweak symmetry breaking	16
2.3 Parton density functions	18
2.4 Next to leading order corrections	20
2.4.1 Divergencies in next-to-leading order corrections	21
2.4.2 Making the divergent theory finite	22
2.5 Running couplings	24
2.6 Classification of the renormalisabilities	24
3 Anomalous triple gauge boson couplings	26
3.1 Leading order helicity amplitudes for $q\bar{q} \rightarrow ZZ \rightarrow e^+e^-\mu^+\mu^-$	28
3.2 Operator expansion in the ZZ sector	34
3.3 Leading order helicity amplitudes for $q\bar{q} \rightarrow Z^*/\gamma^*Z^*/\gamma^* \rightarrow e^+e^-\mu^+\mu^-$	36
3.3.1 Single resonant diagrams	37
3.4 Virtual QCD corrections to $q\bar{q} \rightarrow Z(^*/\gamma^*)Z(^*/\gamma^*) \rightarrow e^+e^-\mu^+\mu^-$	37
3.5 Real emission corrections: $ZZ + j$ contributions	40
3.6 Gluon-gluon fusion	41
3.7 Ranking the loop diagrams	42

4	Monte Carlo event generators	44
4.1	Multichannel Monte Carlo generators	45
4.2	SHERPA	45
4.2.1	The GoSam-SHERPA interface	46
4.3	MADGRAPH	47
4.3.1	The aMC@NLO interface	47
4.4	MCFM	48
4.5	BHO and BR	48
4.6	GoSam	48
4.6.1	The GoSam conventions	49
5	The generic reweighting algorithm	50
5.1	The reweighting method	50
5.2	Structure of the program	51
5.3	Interface description and C++ binding description	52
5.4	Compiling issues	53
5.5	The PDF weight	54
5.6	Functionality study of the GoSam matrix elements	55
5.6.1	GoSam timing: Creation of the process tarballs	55
5.6.2	Creation of the test program DiBosonStudy	57
6	Benchmarking the GoSam matrix element	58
6.1	WW leading order comparisons	58
6.2	ZZ leading order comparisons	60
6.2.1	Validation of the TGC model implemented in GoSam	60
6.2.2	Reweighting tests	62
7	Reweighting Standard Model samples to next-to-leading order	66
7.1	Including the next-to-leading order contributions	66
7.2	Effects of the single resonant diagram	67
7.3	Real emission effects	69
7.4	Effects of the virtual corrections	72
7.5	Testing the reduction libraries in GoSam	75
7.6	On-shell ZZ samples	76
7.7	Observables affected by the next-to-leading order corrections	81
8	Next-to-leading order corrections in TGC samples	83
8.1	$pp \rightarrow e^+e^-\mu^+\mu^-$ at next-to-leading order	84
8.2	Reweighting the $f_5^Z = -0.25$ sample to the Standard Model	86
8.3	The TGC samples at next-to-leading order	87
8.4	Discussion of the off-shell matrix element	92
9	Conclusion and outlook	93
10	Acknowledgment	95
	Appendices	iv
A	Validation of the GoSam matrix element	iv
B	Technical information of the reweighting algorithm	vi
B.1	Prerequisites	vi
B.2	Source codes	vi

C	Interface description of the reweighting algorithm	viii
D	C++ binding description	xi
D.1	Creating the GoSam tarballs	xiii
D.1.1	GoSam installation issues	xiv
D.2	Test program manual	xiv

Abstract

At high center of mass energies in particle collisions the probability of creating virtual particles greatly increases. These virtual particles disturb the initial and final state particles such that one cannot neglect the effects of their interferences with the colliding particles. The description of the particle collisions is based on the concept of Feynman diagrams, from which the matrix element (or probability) can be calculated for any process. This matrix element contains all possible information of the process and extracting this from a simulation or a dataset would result in acquiring the maximum possible information available in the collision. For precision measurements a full matrix element with the virtual corrections must be generated but because of the huge amount of virtual, or next-to-leading order, diagrams this is lacking in many calculations and event generators.

In this thesis a generalised method of including the next-to-leading order corrections has been developed building on the reweighting technique. This technique assigns a weight to each event in a sample by taking the ratio of the differential cross sections calculated from eg. two different models or two different parameter values of the models. The reweighting technique can thus in a fast way include the next-to-leading order effects in a leading order Monte Carlo sample, or be used as a discriminator amongst theories when used on a dataset.

A performance study of the developed algorithm has been done in the $ZZ \rightarrow e^+e^-\mu^+\mu^-$ channel at LHC energies. This is a Standard Model process, but beyond the Standard Model physics have been included in the form of anomalous gauge boson vertices and couplings. The matrix element for on-shell Z-pair production is tested against two other generators, where one of them includes next-to-leading order effects. This benchmarking of the matrix element and algorithm leads to the study of the full next-to-leading order effects in off-shell pair produced Z^*/γ^* -bosons at Standard Model and new physics coupling values, where the last study is the first of its kind.

Dansk resumé

Ved partikelkollisioner med høje center-of-mass-energier er sandsynligheden for at producere virtuelle partikler øget. Disse virtuelle partikler reagerer med de indkommende og udgående partikler i kollisionen. For at få præcise malinger og korrekte teoretiske forudsigelser er man nødt til at inkludere alle virtuelle effekter, men på grund af deres kompleksitet udelades de i de fleste simuleringer. Både de primære og de virtuelle partikler kan beskrives matematisk ved hjælp af en metode udviklet af Feynman, hvori man kan tegne et sæt diagrammer over processen. Disse Feynmandiagrammer bruges til at beregne et såkaldt matrixelement, altså sandsynligheden for at processen finder sted. Denne teoretiske beskrivelse kan anvendes på data eller i simuleringer og giver den maksimale information om kollisionen.

I denne afhandling er der udviklet en metode til at inkludere de manglende virtuelle effekter i simuleringer af partikelkollisioner. Metoden kaldes revægtning og benytter det teoretiske matrixelement til at udregne processens tværsnit for hver enkelt begivenhed. Begivenheden får således en vægt og denne vægt kan benyttes til at forudsige hvordan fordelingen af partiklerne i begivenheden ændrer sig hvis de teoretiske forudsætninger ændres. I denne afhandling er revægtningsmetoden benyttet til at inkludere de virtuelle korrektioner i et sæt begivenheder, der er genereret uden disse korrektioner.

Den udviklede algoritmes ydeevne er undersøgt ved at betragte processen $pp \rightarrow ZZ \rightarrow e^+e^-\mu^+\mu^-$ ved LHC energier. Denne proces kan beskrives ved hjælp af standardmodellen, men effekter der stammer fra en uspecificeret ny fysik er inkluderet i form af anomale tre-boson-vekselvirkninger og dertilhørende koblinger. Matrixelementet, der er benyttet i afhandlingen, er testet mod to andre generatorer for samme proces, hvoraf en af disse inkluderer et mindre sæt af de virtuelle korrektioner. Valideringen af matrixelementet i algoritmen leder til det fulde studie af de virtuelle korrektioner i processen $pp \rightarrow Z^*/\gamma^*Z^*\gamma^* \rightarrow e^+e^-\mu^+\mu^-$ i både standardmodellen og den anomale koblingsmodel. Det sidste af disse studier er det første af sin slags.

Introduction

1.1 Physics teaser

Particle physics is the study of the fundamental constituents of matter and their interactions. The idea of everything being made of small 'unbreakable' parts originates in Ancient Greece where the term *atomos*, meaning indivisible, was first used. But the idea of what the smallest things are has changed numerous times. Today scientists believe everything is built from the following matter constituents, the three generations of *quarks* and *leptons*, while the forces are carried by *bosons*. Most of what is present in our everyday world is built from the first generation of quarks, the up and down quarks, as well as the one of the particles in the first generation of leptons, the electron. The other two generations of quarks and leptons are mostly produced at high energy scales such as in stars and at accelerators. Inherently the most important tool to probe these basic constituents is the accelerator.

Currently one of the most important accelerators is the Large Hadron Collider (LHC) at the European Organisation for Nuclear Research (CERN) located at the border of France and Switzerland. This accelerator collides beams of protons for particle physics as well as lead beams for heavy ion physics.

The LHC was built to probe our current theory of Nature, the Standard Model. This is a model describing the particles and forces of Nature and was formulated in the last century. It is a mathematical formulation based on symmetries of Nature and has proven to be a great success predicting new particles found in accelerator experiments many years after. But of course it still has some problems. One of the biggest problems of the Standard Model is that in its basic form it does not allow particles to have mass. It describes the short-range forces well, but does not include the long-ranged force gravity. Also it does not describe the dark matter and dark energy, believed to form up to 95% of our Universe. Nevertheless the Standard Model has major advantages and is widely believed to be true, at least as an effective theory of Nature.

The Standard Model predicts the existence of gauge bosons. These are the force carriers of the theory and the familiar photon is one of these. The photon mediates the electromagnetic force, first described by Maxwell in 1873. Besides the electromagnetic force the Standard Model includes the strong and the weak nuclear forces. The strong force is mediated by gluons and is responsible for keeping the quarks locked inside the particles they form, such as the protons and neutrons. The weak force is mediated by the Z^0 and W^\pm bosons and is responsible for nuclear decay. Unification of the weak and the electromagnetic forces was done in the second half of the 20th century and was awarded with the Nobel Price in 1979. The combination of these two forces only arises at high energies and they are separable in

our normal everyday world. But at accelerators one probes the high energy regime and must therefore associate both the photon and the W^\pm and Z^0 bosons as force carriers for this electroweak theory. This combination of forces led to the idea of a Grand Unification Scale, an energy scale where all known forces will combine into one Grand Unification Theory (GUT). But so far, no one knows the GUT scale and no widely convincing GUTs have been proposed.

Generally tests of new theories can be done in two ways: Either one can choose a theory before the experiment, and then use the theoretical predictions to look for signs of this theory, or one can look for deviations from the Standard Model in a theory-independent way, and then afterwards compare the experimental results to known theoretical predictions. The former method is widely used, eg. when looking for supersymmetric partners to the known particles or when one looks for signs of the Higgs boson. The latter method is used in this thesis, and thus it will not be concerned with the theories creating the possible deviations from the Standard Model.

This thesis will probe new physics through diboson production at LHC energies. Two bosons can be produced at the LHC through boson emission from two incoming quarks or one incoming (anti)quark and one gluon, through quark annihilation or finally through gluon induced processes. The probability of the pair production is of course related to which bosons are produced, but is generally very low compared to single boson production. The cross sections lie in the range from 10 to 10^3 pb, corresponding to 50.000 - 5.000.000 diboson pairs/year produced at ATLAS if 5 inverse femtobarn of data is recorded. The statistics here are much better than eg. Higgs searches, where a total number of Higgses/year are expected to be 5 - 5.000, depending on the decay channel. Thus the statistics allow for delicate precision measurements. These precision measurements provide very efficient tests of the Standard Model, since only certain diboson combinations are allowed. The electroweak symmetries in the Standard Model strongly constrain the combinatorics of particles as well as the strength of the couplings between the particles. Any deviations from the predicted parameter values could be a sign of new physics.

1.2 Thesis teaser

Following this introduction the thesis is divided in to three parts: A theoretical part, concerning the Standard Model, anomalous couplings between gauge bosons and next-to-leading-order predictions. Then a more technical part follows, describing the aspects of Monte Carlo simulations, a presentation of the developed algorithm for event-by-event reweighting and benchmarking of this algorithm. Finally a part is dedicated to using the algorithm on Monte Carlo simulations, and results obtained on the chosen diboson process, $ZZ \rightarrow e^+e^-\mu^+\mu^-$. The thesis concludes with a discussion of results, models, algorithms and future aspects of the diboson analysis and searches for new physics.

1.3 Units

Throughout the thesis Natural Units will be used: $\hbar = c = 1$. These units give mass and energy same unit and will be described in the energy unit electron volts (eV). This is the kinetic energy an electron receives when accelerated through a charge potential of one Volt. Since particles usually are heavy, most expressions will be given in units of GeV (10^9 eV). The natural units also give rise to length and time being expressed as inverse energy. Probabilities of finding specific particles are expressed as cross sections with units of area, ie. inverse energy squared.

When multiplying the cross section with the luminosity (total number of events produced) at a given accelerator one gets the number of expected events $N = \mathcal{L} \cdot \sigma$, the equation used to estimate the number of diboson events in the previous section. Usually cross sections are given in barns, where one barn equals 10^{-28} m^2 and thus luminosities are given in inverse barns. As stated above diboson cross sections are of the order $10\text{-}10^3$ picobarn (pb) where one pb equals 10^{-12} b . Luminosities are usually given in inverse femtobarn (fb^{-1}) and thus correspond to 10^{15} b^{-1} .

Theory

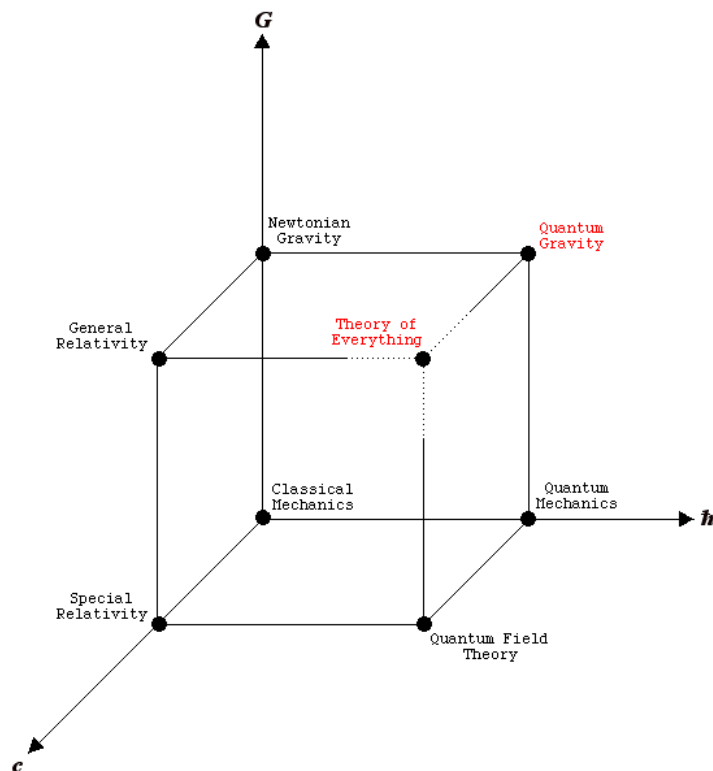


Figure 2.1: Cube showing the fundamental theories of physics. The ones in red are yet to be constructed [1]

The theories of fundamental physics can in general be described as a cube with axis corresponding to the fundamental constants, \hbar (Planck's constant), c^{-1} (the inverse speed of light) and G (the gravitational constant). The different theories known can be set as points in this coordinate system depending on which constants the theory includes. Take classical mechanics as an example: This theory will be located in the origin, since the everyday world of rolling balls, springs and sliding objects cannot be bothered with any of these fundamental constants. Moving on to larger scales, one must include the gravitational constant, since this determines the motion of planets, stars, comets etc. Thus Newtonian Gravity will be located in the point $(c, \hbar, G) = (0, 0, 1)$. Consider then the motion of massless particles or very,

very fast objects on large scales. These objects will be determined by both the gravitational constant and the speed of light. Thus in the point $(c, h, G) = (1, 0, 1)$ lies Einsteins theory of General Relativity. This theory arose from his theory of Special Relativity, concerning massless or very fast objects on small scales, ie. the Special Relativity is located in the point $(c, h, G) = (1, 0, 0)$. Going from large scale structures to small scale structures one obtains Quantum Mechanics. This is a classical theory in the sense that it only concerns itself with slowly moving objects. Thus Quantum Mechanics is located in the point $(c, h, G) = (0, 1, 0)$. Applying quantum mechanics on fast objects leads to Quantum Field Theory on which the Standard Model is based. The Standard Model is flawed though, with problems and difficulties not thoroughly explained in its cleanest form. But it has been used to predict particles and interactions later discovered at accelerators. In the corners $(c, h, G) = (0, 1, 1)$ and $(c, h, G) = (1, 1, 1)$ no widely convincing theories have been proposed. But efforts are being made to combine all three fundamental constants in to one big theory, the Theory of Everything or the Grand Unification Theory.

This chapter begins with a brief discussion of the topics and notations of quantum field theory and how one constructs a model in quantum field theory. It then continues with a discussion of the Standard Model, the model describing the elementary particles and their interactions. Then follows a description of how one makes predictions based on the matrix element of a process and how these predictions are affected when proton-proton collisions occur. Then comes a section dedicated to higher order corrections to processes, describing in turn the divergencies arising, how one locates them and removes them to obtain a finite theory.

2.1 Basics of quantum field theory

Here follows a short review of the basics of quantum field theories. It is not meant as a full mathematical description, but rather as a brief introduction to the notation of the topic. A more formal description can be found in eg. [2, 3, 4] where, unless otherwise stated, this section is based on the findings in [4].

The Standard Model is a theory of the elementary particles. Where quantum mechanics describes very small scales well, it breaks down when relativistic effects are taken into account. Thus one has to move from the world of quantum mechanics to the world of quantum field theory, where particles no longer describe our world, but one sees it rather as a world made of fields, where particles are quanta of these fields. The change of viewpoint may sound strange, but one can overcome the strangeness of fields by imagining them as a sea or a mattress filling the world. Then imagine something disturbing this sea or mattress, such that ripples are created. These ripples, or excitations, are then the particles of the theory, and it is now easy to imagine particle propagation through fields as a ripple spreading outward. It is now evident why there is a need for a formulation of the theory based on some sort of probability, since the ripples may start out very peak-like and then later spread out to be more flat than it might have been at first. This means that from a given set of initial conditions (peak height, width etc. of the ripple) and knowledge of the sea (viscosity, energy etc.) one can predict the probability of finding the ripple in another state (in another place or in the same place after a given time has passed), by calculating the squared amplitude of this scenario.

Mathematically all this is expressed using a fundamental quantity called the action, \mathcal{S} . The action is the time integral of the lagrangian, which contains all kinematical and dynamical information of the system under consideration. Working with local field theories,

where particles only exist as excitations of the field, allows us to write the lagrangian as the spatial integral of the lagrangian density, \mathcal{L} ¹.

$$\begin{aligned}\mathcal{S} &= \int L(\phi_i, \partial_\mu \phi_i) dt \\ &= \int \mathcal{L}(\phi_i, \partial_\mu \phi_i) d^4x\end{aligned}$$

where ϕ_i are the fields in the system. The equations of motion of the fields involved can be found using the principle of least action. This states that when a system evolves from one configuration into another it will do so along a path in the configuration space where the system uses the least amount of energy, ie. where the difference between the action in the two configurations, $d\mathcal{S}$, is an extremum. This can be written as $\delta\mathcal{S} = 0$ and leads to

$$\partial_\mu \left(\frac{\partial \mathcal{L}}{\partial (\partial_\mu \phi)} \right) - \frac{\partial \mathcal{L}}{\partial \phi} = 0$$

being the equation of motion for any field ϕ .

When constructing the lagrangian of a theory one starts by specifying its particle content. Having settled on a set of particles one imposes one or more symmetries on the theory. Any transformation of the particles is a symmetry if it leaves the action and the equations of motion invariant. Traditionally one will as a minimum invoke Lorentz and gauge symmetry to the theory such that the equations of motion are invariant under boosts and rotations, the Lorentz symmetry, and under phase transformations, the gauge symmetry. In some cases the transformation acting on the particles will not leave the equations of motion invariant. If one wishes to promote said transformation to a symmetry, a fix is required. This is done by introducing a field to the theory to exactly cancel the term that violated the symmetry. This matching is usually called setting a gauge and all theories, where this matching is needed, are gauge theories.

After imposing the particle content and the symmetries of the theory one has a lagrangian describing the particles, their motion as well as the interactions between the particles. The allowed interactions can then be read off from the lagrangian and from here be used to calculate the probability of an interaction, also known as the expectation value of the process. Assuming the interactions are weak allows us to calculate this expectation value as a perturbative expansion around the ground state. It can be shown that any (time-ordered) expectation value of N fields (ie. N fields squeezed in between two ground state kets and bras, $\langle \phi_1 \phi_2 \cdots \phi_N \rangle$), can be expressed as Feynman propagators², where the Feynman propagators are solutions to the kinematical equations of the field³.

Using this fact Feynman came up with a brilliant method of expressing the interactions as drawings, giving each line and connection in the drawing a mathematical formulation, such that one (more) easily can derive the amplitudes needed to calculate the probabilities for a given process. The probability of the process directly relates to the factors in the mathematical formulations. This means that the most probable interactions are the ones where the factors in front of the mathematical expressions have the lowest order, eg. an interaction with a factor of λ will be more probable than an interaction with a factor of λ^2 for weak couplings, $\lambda \ll 1$.

The idea behind the Feynman diagrams is that to each particle one assigns a line, be it straight, wavy, curly, and then only once calculate what the expression of the line is. One

¹From now on denoted the lagrangian

²This is Wicks theorem, see eg. [4].

³An example is the scalar propagator. This is found by looking at the solutions to the Klein-Gordon equation that describes the propagation of a scalar field without any interactions.

can use the same method for the connections, or vertices, between the lines, hence whenever one encounters that specific type of connection between lines one inserts the calculated mathematical expression in the equations. Thus the end results is a set of drawings specifying what the amplitude is. By doing a Fourier transformation from position-space to momentum-space the mathematical expression are simplified further. This moves the problem of hard calculations to a problem concerning imagining all the types of diagrams generating a specific process. Once you have thought up all possible combinations the actual calculation is simpler and shorter than before.

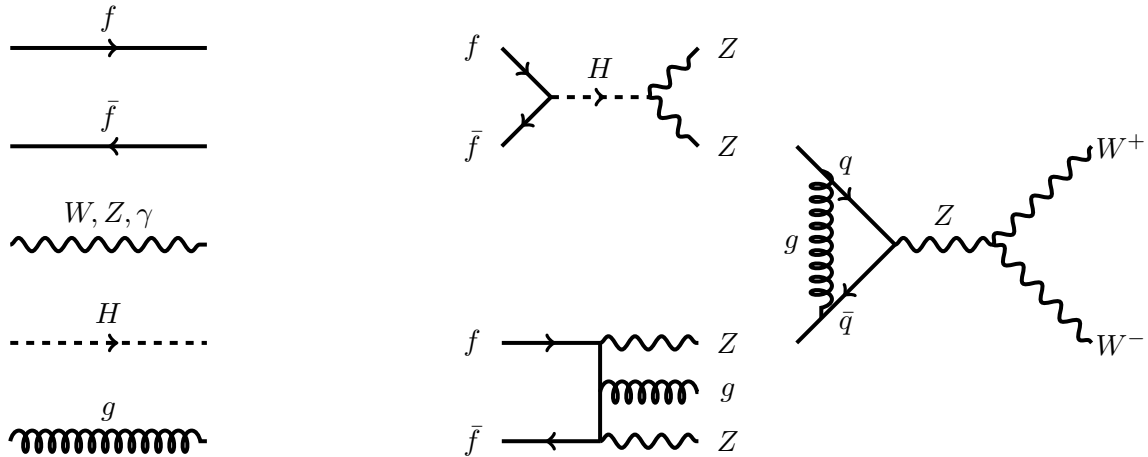


Figure 2.2: Illustrative example of Feynman diagram drawing. To the left the line styles for the various particles are shown. The middle top figure shows two fermions annihilating into a higgs then creating a pair of bosons. The middle bottom figure shows two quarks emitting two bosons and a gluon, making the process a real emission diagram, showing itself as a two boson plus a jet system. The right figure shows two quarks annihilating into a boson creating a pair of bosons. But notice here that before annihilation the quarks exchange a gluon, making the process less likely, since it is now suppressed with the coupling squared with respect to the diagram without such gluon exchange.

Since the theories are quantum theories the uncertainty principle allows for virtual particle-antiparticle pairs to be produced for a short time. This means that a line can be spontaneously split into two, evolve in time, and then combine into one again. This type of process makes the calculations more difficult, since the expressions of the virtual particles carry integrals over their propagators, often leading to divergencies. These divergencies pose a huge problem for quantum field theory, but sometimes one can eliminate these divergent terms by subtracting opposite sign divergent terms from other diagrams. These might seem like magical cancellations, but one must remember that any amplitude is given by many, many 'subdiagrams' each of which are allowed to diverge, as long as the total process amplitude is finite.

Some processes cannot be saved by these magical cancellations, and a method called renormalisation must be used instead. This is a handy mathematical tool invented to remove divergencies by 'renormalising' the constants of the theory. Thus the statement is that the measured 'constants' of the theory are not the actual constants, but they are values somehow fitted to make the observed world finite. In the formulation of the renormalised theory one must then introduce a new scale up to which the calculations are trusted. This scale is usually called Λ and defines the renormalisation scheme.

2.1.1 Symmetries of a quantum field theory

Before continuing into the territory of equations and formulations of the Standard Model, I would like to discuss the very beautiful theorem, *Noethers Theorem*. This is a theorem concerning symmetries and conserved quantities in a quantum field theory. Noethers theorem is the reason for imposing a transformation to a symmetry, because it states that whenever a transformation is a symmetry we have a conserved quantity.

Say the action is invariant under a transformation $\phi(x) \rightarrow \phi'(x) = \phi(x) + \alpha\Delta\phi(x)$. This means the lagrangian is invariant under the transformation up to a four-divergence: $\mathcal{L}(x) \rightarrow \mathcal{L}(x) + \alpha\partial_\mu\mathcal{J}^\mu(x)$. Comparison of this transformation and results of $\Delta\mathcal{L}$ by variation of the fields leads to the conclusion, that whenever a transformation leaves the action and equations of motion invariant, there is a conserved quantity:

$$\partial_\mu j^\mu(x) = 0 \quad \text{for}$$

$$j^\mu = \frac{\partial\mathcal{L}}{\partial(\partial_\mu\phi)} - \mathcal{J}^\mu$$

The conservation law can also be reformulated by stating that the charge Q is a constant in time,

$$Q \equiv \int j^0 d^3x$$

The conserved quantity is then a natural part of the lagrangian showing the symmetry under exploration. The Lorentz symmetry will give rise to angular momentum being conserved, while the gauge symmetry conserves the electrical charge. Hence the formalism of symmetries plays a very significant role in quantum field theories, since it naturally conserves the quantities one would like to be conserved. There exists two such types of symmetries, a *global* and a *local* symmetry. The former describes a symmetry independent of space-time coordinates, while the latter is dependent on the space-time coordinates.

2.1.2 Building a model: The Yang-Mills lagrangian

As described, the approach is to specify the particle content and then specify the symmetries of the theory. From these two ingredients everything else comes out 'natural'. Inspired by Nature (and [4]) in this example the particle content is a fermion doublet, since the fundamental fermions come in generations, each containing two particles:

$$\psi = \begin{pmatrix} \psi_1(x) \\ \psi_2(x) \end{pmatrix}$$

The fermions here could be an electron and its partner, the electron-neutrino. These are familiar particles from eg. nuclear beta decays and electric currents. The fermions are spin-half particles and thus governed by the Dirac equation, $(i\gamma^\mu\partial_\mu - m)\psi = (i\rlap{\not{D}} - m)\psi$, when propagating through free space. Here γ^μ are the Dirac gamma matrices⁴ and the shorthand notation $\rlap{\not{D}} = \gamma^\mu\partial_\mu$ have been introduced. After a choice of particles one chooses an appropriate symmetry. In this example let us chose an arbitrary phase transformation. This makes the fermions transform as

$$\psi \rightarrow \exp\left(i\alpha^i\frac{\sigma^i}{2}\right)\psi$$

⁴In the Weyl representation they are given as 4×4 matrices $\gamma^0 = \begin{pmatrix} 0 & 1 \\ 1 & 0 \end{pmatrix}$, $\gamma^i = \begin{pmatrix} 0 & \sigma^i \\ -\sigma^i & 0 \end{pmatrix}$ with σ^i being the Pauli matrices.

with σ^i being the familiar Pauli matrices and α arbitrary. Promoting α to be dependent of the spacetime coordinate x makes the symmetry local:

$$\begin{aligned}\psi &\rightarrow \exp\left(i\alpha^i(x)\frac{\sigma^i}{2}\right)\psi \\ &=V(x)\psi\end{aligned}$$

Promoting the symmetry to a local symmetry could in principle be dangerous. The requirement that the equations of motion are invariant under the transformation still holds, but since the transformation now depends on where in space the fields are, one could obtain different equations depending on the phase-space point. The Dirac equation also contain the derivatives of the field. These derivatives can also pose problems, since the fields at two different points transform differently under the phase transformation. Thus one must construct a meaningful method of comparing the values of the field at two different points. This however poses yet another difficulty, since the Pauli matrices do not commute⁵. Defining a *comparator* $U(x, y)$, allows for a comparison of the values of ϕ at two different phase-space points. The comparator transforms as $U(y, x) \rightarrow V(y)U(y, x)V^\dagger(x)$ making it possible to compare the values of the field at the points x and y . The meaningful derivative along a unit four-vector n^μ is given as:

$$\begin{aligned}n^\mu D_\mu \psi &= \lim_{\epsilon \rightarrow 0} \frac{1}{\epsilon} \left[\psi(x + \epsilon n^\mu) - U(x + \epsilon n^\mu, x)\psi(x) \right] \\ &= \lim_{\epsilon \rightarrow 0} \frac{1}{\epsilon} \left[\psi(x + \epsilon n^\mu) - (1 + i\epsilon g n^\mu A_\mu^i \frac{\sigma^i}{2})\psi(x) \right] \\ &= \lim_{\epsilon \rightarrow 0} \frac{1}{\epsilon} \left[\psi(x + \epsilon n^\mu) - \psi(x) - i\epsilon g n^\mu A_\mu^i \frac{\sigma^i}{2}\psi(x) \right] \\ &= n^\mu \partial_\mu \psi(x) - i g n^\mu A_\mu^i \frac{\sigma^i}{2} \psi(x) \\ &= n^\mu \left[\partial_\mu - i g A_\mu^i \frac{\sigma^i}{2} \right] \psi(x)\end{aligned}$$

and is known as the covariant derivate. In the second equality the expansion of the comparator for infinitesimal seperation has been used, $U(x + \epsilon n^\mu, x) = 1 + i g n^\mu A_\mu^i \frac{\sigma^i}{2} + \mathcal{O}(\epsilon^2)$. The *connections* A_μ^i have been introduced, in order to match up both the spacetime-index μ and the 'spinor' index i . This is a new field, a *vector* field since it carries the space-time index μ , and the covariant derivative needs three of these in order to match up all three of the Pauli matrices $\sigma_i, i = 1, 2, 3$.

By looking at the transformation of $U(x, y)$ one obtains the transformation of the connections:

$$A_\mu^i \rightarrow A_\mu^i \frac{\sigma^i}{2} + \frac{1}{g} (\partial_\mu \alpha^i) \frac{\sigma^i}{2} + i \left[\alpha^i \frac{\sigma^i}{2}, A_\mu^j \frac{\sigma^j}{2} \right] + \mathcal{O}(\alpha^2)$$

The propagation of the fields A_μ^i must now also enter in the model and be described by a gauge-invariant term. This term is constructed with the commutator of the covariant derivative, but because of the non-commutative structure of the Pauli matrices the covariant derivatives do not commute. The right-hand side of this commutator is the *field strength tensor*:

$$\begin{aligned}[D_\mu, D_\nu] &= -i g F_{\mu\nu}^i \frac{\sigma^i}{2} \\ F_{\mu\nu}^i &= \partial_\mu A_\nu^i - \partial_\nu A_\mu^i + g \epsilon^{ijk} A_\mu^j A_\nu^k\end{aligned}$$

⁵ $[\sigma_i, \sigma_j] = 2i\epsilon^{ijk} \sigma_k$

and will be used to construct the gauge invariant lagrangian describing the connection, A_μ^i . The field strength tensor however is not gauge invariant, but can be constructed in a gauge invariant form by taking the trace:

$$\begin{aligned}\mathcal{L} &= -\frac{1}{2}\text{tr}\left[\left(F_{\mu\nu}^i\frac{\sigma^i}{2}\right)^2\right] \\ &= -\frac{1}{4}(F_{\mu\nu}^i)^2\end{aligned}$$

Thus one obtains a gauge and Lorentz invariant lagrangian describing the fields ψ and A_μ^i by setting the gauge $igA_\mu^i\frac{\sigma^i}{2}$ and the final result is the complete Yang-Mills lagrangian:

$$\begin{aligned}\mathcal{L} &= \bar{\psi}(i\not{D} - m)\psi - \frac{1}{4}(F_{\mu\nu}^i)^2 \\ &= \bar{\psi}(i\gamma^\mu\left[\partial_\mu - igA_\mu^i\frac{\sigma^i}{2}\right] - m)\psi - \frac{1}{4}(\partial_\mu A_\nu^i - \partial_\nu A_\mu^i + g\epsilon^{ijk}A_\mu^j A_\nu^k)^2 \\ &= \bar{\psi}(i\gamma^\mu\left[\partial_\mu - igA_\mu^i\frac{\sigma^i}{2}\right] - m)\psi - \\ &\quad \frac{1}{4}\left[(\partial_\mu A_\nu^i - \partial_\nu A_\mu^i)^2 + 2(\partial_\mu A_\nu^i - \partial_\nu A_\mu^i)(g\epsilon^{ijk}A_\mu^j A_\nu^k) + (g\epsilon^{ijk}A_\mu^j A_\nu^k)^2\right] \\ &= \bar{\psi}(i\gamma^\mu\partial_\mu - m)\psi - \frac{1}{4}(\partial_\mu A_\nu^i - \partial_\nu A_\mu^i)^2 - \\ &\quad g\epsilon^{ijk}(\partial_\mu A_\nu^i)A_\mu^j A_\nu^k - \frac{1}{4}(g\epsilon^{ijk}A_\mu^j A_\nu^k)^2 + g\bar{\psi}\gamma^\mu A_\mu^i\frac{\sigma^i}{2}\psi\end{aligned}$$

Here one recognises the first term as the Dirac equation, and the second as the Klein-Gordon equation for a massless field. Thus the first two terms describes each of the fields propagating through free space. The last three terms describes the interactions in the model: The interactions between three vector fields described in the third term, the interaction between four vector fields described by the fourth term and finally the interaction between the fermion doublet and the vector fields.

The Feynman rules can now (almost) be read of from the lagrangian. The interaction between the fermion doublet is written directly, while the interactions between the vector fields are a bit harder to see. To get those interactions one must contract the indices in all possible ways. The derivative contributes with a factor of $-ip_\mu$ for a vector field with momentum p . The contractions between spacetime indices contributes with a factor of $g^{\mu\nu}$, and thus one obtains the following vertex rules:

$$\begin{aligned}A\psi\bar{\psi} &= ig\gamma^\mu\frac{\sigma^i}{2} \\ AAA &= ig\epsilon^{ijk}\left[g^{\mu\nu}(p_1 - p_2)^\alpha + g^{\nu\alpha}(p_2 - p_3)^\mu + g^{\alpha\mu}(p_3 - p_1)^\nu\right] \\ AAAA &= ig^2\left[\epsilon^{ijm}\epsilon^{klm}(g^{\mu\alpha}g^{\nu\beta} - g^{\mu\beta}g^{\nu\alpha}) + \right. \\ &\quad \left. \epsilon^{ikm}\epsilon^{jlm}(g^{\mu\nu}g^{\alpha\beta} - g^{\mu\beta}g^{\nu\alpha}) + \epsilon^{ilm}\epsilon^{jkm}(g^{\mu\nu}g^{\alpha\beta} - g^{\mu\alpha}g^{\nu\beta})\right]\end{aligned}$$

The propagators are the free field propagators:

$$\begin{aligned}D_\psi &= \frac{i(\not{p} + m)}{p^2 - m^2 + i\varepsilon} \\ D_A &= \frac{-ig_{\mu\nu}}{p^2 + i\varepsilon}\end{aligned}$$

Thus all the building blocks of the theory are present, and one can use these terms to calculate the amplitudes of a given process.

2.1.3 Calculating amplitudes and cross sections

Once the Feynman rules of a theory have been constructed the framework for calculating process amplitudes is as follows: The diagrams for the process under consideration are drawn. This is then converted into a mathematical expression using the Feynman rules of the theory. This mathematical expression is known as the matrix element, \mathcal{M} , of the process. This matrix element holds all information of the process, such as momenta, spin and polarisation of the particles involved. The matrix element is also known as the amplitude of the process, the quantity described in the beginning of this chapter.

Once the matrix element is formed, the differential cross section, $d\sigma$, can be calculated. The differential cross section is a measure of how likely a process is, ie. a form of probability. It is found from the matrix element through:

$$d\sigma = \frac{1}{2s} |\mathcal{M}|^2 d\Phi$$

$$d\Phi = (2\pi)^4 \delta(k_1 + k_2 - \sum_{i=1}^N p_i) \prod_{i=1}^N \frac{d^3 \vec{p}_i}{(2\pi)^3 2E_i}$$

where the phase-space function Φ contains the Dirac delta function explicitly demanding momentum conservation in the process. It is known as the N -body phase-space function, and fortunately any N -body phase-space function can be decomposed into the simpler two-body or three-body phase-space functions. Letting k_1, k_2 denote the incoming momentum and p_1, p_2 denote the outgoing momentum, one can calculate the two-body phase space function in the rest frame of the two-body system, $k_1 + k_2 = (\sqrt{s}, 0, 0, 0)$ [4]:

$$\begin{aligned} \int d\Phi_2 &= \int (2\pi)^4 \delta(k_1 + k_2 - p_1 - p_2) \frac{d^3 \vec{p}_1}{(2\pi)^3 2E_1} \frac{d^3 \vec{p}_2}{(2\pi)^3 2E_2} \\ &= \frac{\lambda}{8\pi} \int \frac{d \cos \theta}{2} \frac{d\phi}{2\pi} \\ &= \frac{\lambda}{64\pi^2} \int d\Omega \end{aligned}$$

with $\lambda = \sqrt{1 - \frac{2(m_1^2 + m_2^2)}{s} + \frac{(m_1^2 - m_2^2)^2}{s}}$. Hence the differential cross section becomes

$$\frac{d\sigma}{d\Omega} = \frac{1}{64\pi^2 s} \lambda |\mathcal{M}|^2$$

and it is thus evident that the most informative quantity of a process is the matrix element. Integrating over the scattering angle, $d\Omega$, gives the total scattering cross section of the process, σ . One can from this cross section estimate the total number of events produced in a collision by multiplying the cross section with the luminosity:

$$\sigma = \int \frac{d\sigma}{d\Omega}$$

$$N = \mathcal{L}\sigma$$

When the colliding particles are elementary particles, such as photons and electrons, this scattering cross section is the final result. But when colliding particles built from the elementary particles, other effects must be taken into account. This is because one must estimate the probability of taking out an elementary particle from its mother particle, eg. taking out a quark from a proton. The distribution of the elementary particles inside the protons are not exactly known, and one must estimate them using *parton density functions*. This topic will be described in Sec. 2.5.

2.2 The Standard Model of Particle Physics

The scene has now been set such that one is able to construct the Standard Model lagrangian. Following the method of field theory construction, I will start out with describing the particle content of the Standard Model, proceed to describing the symmetries of the theory and then finally write down the lagrangian and use this to describe the interactions allowed in the Standard Model.

mass →	≈2.3 MeV/c ²	≈1.275 GeV/c ²	≈173.07 GeV/c ²	0	≈126 GeV/c ²
charge →	2/3	2/3	2/3	0	0
spin →	1/2	1/2	1/2	1	0
	u up	c charm	t top	g gluon	H Higgs boson
QUARKS	≈4.8 MeV/c ²	≈95 MeV/c ²	≈4.18 GeV/c ²	0	
	-1/3	-1/3	-1/3	0	
	1/2	1/2	1/2	1	
	d down	s strange	b bottom	γ photon	
	0.511 MeV/c ²	105.7 MeV/c ²	1.777 GeV/c ²	91.2 GeV/c ²	
	-1	-1	-1	0	
	1/2	1/2	1/2	1	
	e electron	μ muon	τ tau	Z Z boson	
LEPTONS	<2.2 eV/c ²	<0.17 MeV/c ²	<15.5 MeV/c ²	80.4 GeV/c ²	
	0	0	0	±1	
	1/2	1/2	1/2	1	
	ν_e electron neutrino	ν_μ muon neutrino	ν_τ tau neutrino	W W boson	
				GAUGE BOSONS	

Figure 2.3: Table showing the particles of the Standard Model and their quantum numbers [5]

The Standard Model is the theory of the smallest and fastest things. It was developed in the mid to late 20th century, and its current form was developed in the 1970's when unification of the weak and electromagnetic forces was made. It is a theory describing the fundamental particles, *quarks*, *leptons* and *gauge bosons*, and the interactions amongst them. The fermions are the matter particles and are split into two categories, quarks with charges that are multiples of 1/3 and leptons with integer charge. The bosons are the force carriers and have integer spin. Thus a division of the particles is made based on their quantum numbers, where the most relevant quantum numbers in the Standard Model are electrical charge, colour charge and spin, an intrinsic form of angular momentum. A further subdivision can be done based on other quantities such as mass, lifetime etc.

There are many other ways to describe and classify the particle content. Besides the quantum numbers the way they transform under a certain symmetry can classify them. If some particles in the theory do not preserve a symmetry while others do, there is an asymmetry in the theory. This breaking of symmetries has evolved into most parts of quantum field theory, where eg. the chiral symmetry breaking is responsible for generating almost all mass in protons and neutrons, consisting of light and massless particles. The electroweak symmetry breaking is responsible for the fundamental particles acquiring mass with the (in)famous Higgs boson as a much discussed companion to the symmetry breaking. The symmetries of the Standard Model will be described in Sec. 2.1.1. and its implications to the theory in Secs. 2.2.4 and 2.2.3.

2.2.1 Particle content

Particle	Symbol	Mass (MeV)	Lifetime (s)	Charge	Spin
Electron	e^-	$0.511 \pm 1.1 \cdot 10^{-8}$	Stable	-1	1/2
Muon	μ^-	$105.658 \pm 3.5 \cdot 10^{-6}$	$2.197 \cdot 10^{-6} \pm 2.2 \cdot 10^{-12}$	-1	1/2
Tau	τ	1776.82 ± 0.16	$(290.6 \pm 1.0) \cdot 10^{-13}$	-1	1/2
Electron neutrino	ν_e	< 0.0002	-	0	1/2
Muon neutrino	ν_μ	< 0.19	-	0	1/2
Tau neutrino	ν_τ	< 18.2	-	0	1/2
Down-quark	d	$4.8^{+0.7}_{-0.3}$	Stable	-1/3	1/2
Up-quark	u	$2.3^{+0.7}_{-0.5}$	Stable	2/3	1/2
Strange-quark	s	95 ± 5	Stable	-1/3	1/2
Charm-quark	c	1275 ± 25	Stable	2/3	1/2
Bottom-quark	b	4180 ± 30	Stable	-1/3	1/2
Particle	Symbol	Mass (GeV)	Width (GeV)	Charge	Spin
Top-quark	t	173.5 ± 0.6	$2.0^{+0.7}_{-0.6}$	2/3	1/2
Photon	γ	0	Stable	0	1
Z-boson	Z	91.1876 ± 0.086	2.4952 ± 0.0023	0	1
W-boson	W^\pm	80.385 ± 0.015	2.085 ± 0.042	-1	1
Gluon	g	0	Stable	0	1
Higgs	H	125.5	-	0	0

Table 2.1: List of particle properties from [6]. - indicates no measurements has been made.

The matter particles of the Standard Model are fermions. All fermions have half-integer spin and the fundamental fermions are subdivided into two classes, quarks and leptons. Each of these come in three generations consisting of two particles. To each of the fermions there exist a corresponding antiparticle with the same mass, but opposite electrical charge. The quarks have an additional feature, *colour*. This is a conserved quantity in the theory describing the quarks and comes in three variations *red*, *green* and *blue*.

The gauge bosons are the force carriers of the theory. They carry the three forces included in the Standard Model, the strong, the weak and the electromagnetic forces. The electromagnetic force is carried by the photon (γ) and interacts with all particles carrying electrical charge. Since the photon is massless the force is infinite in range. The force conserves the electrical charge, Q . The weak force is mediated by the Z^0 and the W^\pm particles. These are massive particles, and the force is thus short-ranged. The force conserves weak isospin, I_3 and is responsible for the familiar nuclear decays. The unification of these two forces lead to the fact that one cannot separate the two forces at high energies. This also means that all four bosons carry the electroweak force. This force conserves the weak hypercharge, Y , a combination of the quantum numbers of each of the two combined theories, $Y = 2(Q - I_3)$. The electroweak theory is an important part of this thesis and will be thoroughly explained in Sec. 2.2.4.

The final bosons to be described are the *gluons*. There are eight of these, corresponding to the eight connections of the symmetry group describing the strong force. The gluons are massless, making the strong force infinite in range. They interact with all particles carrying colour charge, since they themselves are coloured. Since the particles observes are colourless, the gluons are used to bind the quarks into protons and neutrons. From the same observation the coloured particles acquire an extra feature: They are confined. This means that if one tries to separate two coloured particles from the colourless state, the force potential between the particles grows as the distance between them grows. This will continue until enough energy is stored to create a new set of particles colour-combining with the old particles, hence creating two new colourless particles. This is a remarkable feature not seen in any of the other forces.

2.2.2 Symmetries of the Standard Model

In the Standard Model a global Poincaré symmetry is imposed [3], meaning that the Standard Model lagrangian should be invariant under space-time translations, rotations and boosts. The familiar Lorentz symmetry is imbedded in the Poincaré symmetry, hence the conserved quantities are linear and angular momentum. A local $SU(3)_C \otimes (SU(2)_L \otimes U(1)_Y)$ symmetry is also imposed [3], giving rise to the strong interactions and electroweak interactions respectively. These symmetries conserve colour and hypercharge. Symmetry under the global phase transformations ⁶ $\psi \rightarrow e^{i\alpha}\psi$ and $\psi \rightarrow e^{i\alpha\gamma^5}\psi$ are also imposed [4], the former conserving the electrical charge and the latter, the Chiral symmetry, conserving the fermion number.

A set of discrete symmetries is also imposed, being symmetry under *parity* and *charge* conjugation [4]. The parity operator performs a spatial inversion through the origin, ie. it changes the sign of the spatial coordinates. This results in a new quantum number, parity, to the particles of the theory. When applying the parity operator on a particle twice, the original state is obtained, hence the eigenvalues of the parity operator, \hat{P} , are $P = \pm 1$. Bosons and anti-bosons have the same parity, while fermions and anti-fermions have opposite parity.

The charge conjugation operator flips the sign of the charges, effectively turning a particle in to an antiparticle. As with parity, the transformation can be performed twice resulting in the original state. Thus the eigenvalues are $C = \pm 1$ for the operator \hat{C} . The strong and electromagnetic interactions both preserve P and C separately, while they are violated in the weak interactions.

2.2.3 Quantum Chromo Dynamics

The particle content of this theory is the quarks and the gluons. The imposed symmetry is the $SU(3)_C$ symmetry, resulting in the QCD lagrangian. This can be split into parts, one concerning the gauge bosons of the group and one describing how the particles interact with these gauge bosons. Starting with the bosonic term it can be written as follows [4]:

$$\begin{aligned}\mathcal{L} &= -\frac{1}{4}G_{\mu\nu}^a G^{a\mu\nu} \\ &= -\frac{1}{4}(\partial_\mu G_\nu^a - \partial_\nu G_\mu^a + g_S f^{abc} G_{b\mu} G_{c\nu})^2 \\ &= -\frac{1}{4}\left[(\partial_\mu G_\nu^a - \partial_\nu G_\mu^a)^2 + (g_S f^{abc} G_{b\mu} G_{c\nu})^2 + 2(\partial_\mu G_\nu^a - \partial_\nu G_\mu^a)(g_S f^{abc} G_{b\mu} G_{c\nu})\right]\end{aligned}$$

where $a = 1\dots 8$. From the lagrangian the gluon self couplings can be seen. There are two types of self-couplings, three and four gluon interactions. The factor g_S is the strong coupling constant, denoting how strongly the gluons couple to themselves.

The term involving quarks is as follows [4]:

$$\begin{aligned}\mathcal{L} &= \sum_{m=1}^3 i\bar{q}_m \not{D} q_m \\ &= \sum_{m=1}^3 i\bar{q}_m (\partial_\mu + ig_S G_\mu^a \frac{\lambda^a}{2}) \gamma^\mu q_m\end{aligned}$$

Here the q 's are Dirac spinors representing the flavours of the quarks ($q = u, c, t, d, s, b$), $m = 1, 2, 3$ denotes the colour of the quark and λ_a are the Gell-Mann matrices.

One may wonder why there is no mass terms of the form $m^2 \bar{q}q$ just as in the Yang-Mills lagrangian. The reason is that this type of mass term will break gauge invariance when electroweak interactions of the quarks are taken into account. Thus masses must be introduced in a different manner.

⁶ $\gamma^5 = i\gamma^0\gamma^1\gamma^2\gamma^3$.

2.2.4 Electroweak theory

The particle content of this theory is all the fundamental fermions. Imposing the $SU(2)_L \otimes U(1)_Y$ symmetry to the theory gives rise to the electroweak force, carried by the aforementioned gauge bosons, γ, Z^0, W^\pm . The group $SU(2)_L$ has three connections, $W^i, i = 1 \dots 3$ and $U(1)_Y$ has one connection B . $SU(2)_L$ carries the subscript L stating that it only acts on the lefthanded chiral representation, while the $U(1)_Y$ carry the subscript Y stating that the conserved quantity is hypercharge Y described earlier. Particles transforming under this symmetry group are said to be weakly interacting and all types of particles (except gluons) interact with the bosons of the symmetry group.

The bosonic terms of the electroweak theory is as follows [4]:

$$\begin{aligned} \mathcal{L} &= -\frac{1}{4}W_{\mu\nu}^iW^{i\mu\nu} - \frac{1}{4}B_{\mu\nu}B^{\mu\nu} \\ &= -\frac{1}{4}(\partial_\mu W_\nu^i - \partial_\nu W_\mu^i + g\epsilon^{ijk}W_{\mu j}W_{\nu k})^2 - \frac{1}{4}(\partial_\mu B_\nu - \partial_\nu B_\mu)^2 \\ &= -\frac{1}{4}\left[(\partial_\mu W_\nu^i - \partial_\nu W_\mu^i)^2 + (g\epsilon^{ijk}W_{\mu j}W_{\nu k})^2 + 2(\partial_\mu W_\nu^i - \partial_\nu W_\mu^i)(g\epsilon^{ijk}W_{\mu j}W_{\nu k})\right] \\ &\quad - \frac{1}{4}(\partial_\mu B_\nu - \partial_\nu B_\mu)^2 \end{aligned}$$

From this lagrangian the boson self-interactions are again found. But notice that only the $SU(2)_L$ connections interact amongst themselves. Thus a search for the three boson interactions will be a clear test of the Standard Model, since they are predicted to exist in specific ways. These can be observed directly compared to the three gluon interactions, where the colour charge of the gluons interfere with direct observations. Four boson interaction searches provide the same test, but are much less likely to occur, being suppressed with an additional factor of g .

The interaction between the force carriers and the matter particles is less trivial. This is because the electroweak theory is chiral. That a theory is chiral means there is an assymetry under the chiral phase transformations, ie. not all particles in the theory transform equally under this transformation. The chiral transformation was introduced in Sec. 2.2.2, and involves the γ^5 matrix. This matrix can be used to project out the chirality of the particles through the projection operators $P_\pm = \frac{1 \pm \gamma^5}{2}$ [4]. Thus a component of a two-component spinor can be projected out using $\psi_{L,R} = P_\pm \psi$. Without projecting the handedness out, the interaction term is very simple [4]:

$$\mathcal{L} = \sum_{m=1}^3 i\bar{q}_m \not{D} q_m + i\bar{l} \not{D} l$$

with $q = u, d, s, c, t, b$ and $l = e, \mu, \tau, \nu_e, \nu_\mu, \nu_\tau$. The covariant derivative is $D_\mu = \partial_\mu + ig\frac{\sigma^i}{2}W_\mu^i + i\frac{g'}{2}B_\mu$. If one chooses to project out the handedness the end result is that one obtains two different covariant derivatives, one acting on the left-handed particles and one acting on the righthanded particles. The covariant derivative for the righthanded particles will not include the connections W^i , since these do not act on the righthanded particles. Thus the chiral assymetry is evident through the covariant derivatives, which gives rise to the interactions amongst the particles and the connections.

This is the electroweak theory for massless particles. It is simple and descriptive in its form, but it does contain problems. The biggest problem is that the particles we observe

have a measured mass. But introducing a mass term by hand here, breaks gauge invariance and it is thus not possible to do. One also needs to split the theory at low energies into the weak and the electrodynamic theories, ie. the electroweak theory must be broken to these two separate components observed in our everyday world. The splitting is done by introducing a new matter particle to the theory, and by looking at how this new particle transforms under the symmetries of the theory. By setting an explicit gauge, the symmetric theory will become asymmetric and thus the symmetry of the theory have been broken. This is called *spontaneous symmetry breaking* and is widely used in the Standard Model. Spontaneous symmetry breaking means that a system goes from a symmetric state (eg. all particles are massless) to an asymmetric state (eg. some particles acquire mass, some do not). The asymmetric state now hides the internal symmetry of the system.

2.2.5 Electroweak symmetry breaking

Introducing a scalar field to the electroweak theory and selecting the potential of the field precisely, will result in spontaneous symmetry breaking. The field one chooses is a complex scalar doublet, $\phi = (\phi^1 + i\phi^2, \phi^0 + i\phi^3)$ and one chooses a gauge in which only the zero'th component of the field has a nonzero value: $\langle\phi\rangle = \frac{1}{\sqrt{2}}(0, v)$. It couples to the gauge bosons in the usual covariant way [4]:

$$\begin{aligned}\mathcal{L}_\phi &= (D^\mu\phi)^\dagger D_\mu\phi - V(\phi) \\ &= \phi^\dagger(\partial^\mu + ig\frac{\sigma^i}{2}W^{\mu i} + \frac{ig'}{2}B^\mu)^\dagger(\partial_\mu + ig\frac{\sigma^i}{2}W_\mu^i + \frac{ig'}{2}B_\mu)\phi - V(\phi)\end{aligned}$$

One could imagine all sorts of potentials for this scalar field. But the requirement is at least one stable minimum, otherwise the potential could become infinitely large. Thus the simplest potential imaginable is a $a\phi^2$ potential. Because of the chosen gauge, the potential obtains the form $V(\phi) = \frac{a}{2}v^2$. Thus there is only one minimum at $v = 0$. But this completely removes ground state of the scalar field and thus it cannot be responsible for ground state symmetry breaking. Thus one must seek the second best potential, $V(\phi) = a\phi^2 + b\phi^4$. Solving for $V'(\phi) = 0$ gives two solutions: $v^2 = 0$ or $v^2 = \frac{-2a}{b}$, leading to three extrema, $v = 0$ and $v = \pm\sqrt{\frac{-2a}{b}}$. An appropriate choice of $a < 0$ and $b > 0$ will lead to $v = 0$ being unstable and $v = \pm\sqrt{\frac{-2a}{b}}$ being stable. This is exactly the type of potential needed: Think of the unstable solution being the massless electroweak theory described above, and the stable minima giving rise to the massive electroweak theory. The end result for the lagrangian is:

$$\begin{aligned}\mathcal{L}_\phi &= (D^\mu\phi)^\dagger D_\mu\phi - V(\phi) \\ &= \phi^\dagger(\partial^\mu + ig\frac{\sigma^i}{2}W^{\mu i} + \frac{ig'}{2}B^\mu)^\dagger(\partial_\mu + ig\frac{\sigma^i}{2}W_\mu^i + \frac{ig'}{2}B_\mu)\phi \\ &\quad + \mu^2\phi^\dagger\phi - \frac{\lambda}{2}(\phi^\dagger\phi)^2\end{aligned}$$

where one requires $\mu^2 < 0$. The vacuum acquires an expectation value of $v = \frac{|\mu|}{\sqrt{\lambda}}$ making it possible to give masses to the gauge bosons via gauge boson - scalar field interactions. Concentrating only on the relevant terms for creating mass to the gauge bosons, one obtains

[4]:

$$\begin{aligned}
\mathcal{L}_\phi &= \phi^\dagger \left(-ig \frac{\sigma^i}{2} W^{a\mu} - \frac{i}{2} g' B^\mu \right) \left(ig W_\mu^i \frac{\sigma^i}{2} + \frac{i}{2} g' B_\mu \right) \phi \\
&= \frac{1}{\sqrt{2}} (0, v)^\dagger \left(-ig \frac{\sigma^i}{2} W^{a\mu} - \frac{i}{2} g' B^\mu \right) \left(ig W_\mu^i \frac{\sigma^i}{2} + \frac{i}{2} g' B_\mu \right) \frac{1}{\sqrt{2}} (0, v) \\
&= \frac{v^2}{8} [g^2 (W_\mu^1)^2 + g^2 (W_\mu^2)^2 + (-g W_\mu^3 + g' B_\mu)^2]
\end{aligned}$$

Wishing to identify the massless particles, W^i, B with the physical particles W^\pm, Z^0, γ observed requires a rotation of the fields:

$$\begin{aligned}
\begin{pmatrix} Z^0 \\ A \end{pmatrix} &= \begin{pmatrix} \cos \theta_W & -\sin \theta_W \\ \sin \theta_W & \cos \theta_W \end{pmatrix} \begin{pmatrix} W^3 \\ B \end{pmatrix} \\
\begin{pmatrix} W^+ \\ W^- \end{pmatrix} &= \begin{pmatrix} (\sqrt{2})^{-1} & -i(\sqrt{2})^{-1} \\ (\sqrt{2})^{-1} & i(\sqrt{2})^{-1} \end{pmatrix} \begin{pmatrix} W^1 \\ W^2 \end{pmatrix}
\end{aligned}$$

Thus one obtains three massive particles and one massless [4]:

$$\begin{aligned}
W_\mu^\pm &= \frac{1}{\sqrt{2}} (W_\mu^1 \mp i W_\mu^2) && \text{with } M_W = \frac{gv}{2} \\
Z_\mu^0 &= \frac{1}{\sqrt{g^2 + g'^2}} (g W_\mu^3 - g' B_\mu) && \text{with } M_Z = \sqrt{g^2 + g'^2} \frac{v}{2} \\
A_\mu &= \frac{1}{\sqrt{g^2 + g'^2}} (g W_\mu^3 + g' B_\mu) && \text{with } M_A = 0
\end{aligned}$$

One can now rewrite all covariant derivatives and lagrangians in terms of these mass eigenstates and see that the explicit gauge symmetries will have disappeared - the spontaneous symmetry breaking has hidden them underneath the mass eigenstates.

The angle used in the rotation above is called the weak mixing angle. Here $\cos \theta_W = \frac{g}{\sqrt{g^2 + g'^2}}$ and $\sin \theta_W = \frac{g'}{\sqrt{g^2 + g'^2}}$, which leads to $g = \frac{e}{\sin \theta_W}$ and the mass relation $M_W = M_Z \cos \theta_W$. Thus all of electroweak theory is described by just three parameters: The electron charge, e , the weak mixing angle, θ_W and the mass of the W boson, M_W .

It is known from electromagnetism how the electron and photon couple. Thus it would be interesting to see if the same coupling appears in the electroweak theory. This can be done by inserting the physical fields into the covariant derivative for leptons. Doing this one obtain a term proportional to the W bosons, one proportional to the Z boson and the following for the coupling to photons [4]:

$$D_\mu \propto -i \frac{gg'}{\sqrt{g^2 + g'^2}} A_\mu (I_3 + Y)$$

Comparing this with the QED result, $D_\mu \sim -ie A_\mu Q$, the relations are visible: $e = \frac{gg'}{\sqrt{g^2 + g'^2}}$, $Q = (I_3 + Y)$. Thus the $SU_{I_3}(2) \otimes U_Y(1)$ symmetry group has been broken to the $U_Q(1)$ symmetry group. Inserting $Q = -1$ for the electron the familiar form of the electron-photon coupling is obtained.

Unfortunately this scalar field does not automatically couple to the fermions in the Standard Model. But one can add, by hand, interactions between the scalar field and the fermions,

giving rise to the Yukawa terms and the Yukawa couplings:

$$\mathcal{L}_Y = - \sum_{i=1}^3 \left(m_u^i \bar{u}_L^i u_R^i + m_d^i \bar{d}_L^i d_R^i \right) - m_e^i \bar{e}_L^i e_R^i + h.c.$$

where u^i are the up-type quarks, d^i the down-type quarks and e^i are the leptons not including the neutrinos, $m_f = \frac{\lambda_f^i v}{\sqrt{2}}$ and finally λ_f^i are the eigenvalues of the Yukawa matrices. The strength of these Yukawa eigenvalues vary, making the scalar field couple more strongly to the heavier fermions (eg. top and tau).

Finally it must be said that the excitations of this field is known as the Higgs particle. During the writing of this thesis quite many things changed in particle physics. The long sought after boson hinted its existence at first in the summer of 2012, especially in two decay channels, $\gamma\gamma$ and $ZZ \rightarrow 4l$. From the mass distributions of the decay particles one could see bumps at around 125 GeV, making the Higgs a likely candidate for these bumps. The summer ended and more and more data was analysed, not only looking for the mass distribution, but also making spin and parity measurements. And in spring of 2013 it was confirmed that the ATLAS and CMS Collaborations most likely had found the Higgs boson. But whether it is the Standard Model Higgs or an exotic version of it, is yet to be claimed. This will most likely not be confirmed until the LHC starts up again in 2015 after the long shutdown.

2.3 Parton density functions

When colliding protons one collides bound particles. The quarks inside protons are bound by gluons, and thus one can imagine the proton at low energies as a sea of gluons and three valence quarks. Acceleration of the proton results in higher kinetic energy, and virtual quark-anti quark pairs can appear inside the proton. Thus the proton consists of a sea of gluons, virtual quark-antiquark pairs and the three valence quarks. Because of the large size of the protons, one now enters into a non-perturbative area of physics. This results in an approximate description of what happens inside the proton. What one does to overcome this non-perturbative problem is to factorise the constituents of the protons, the *partons*. Because the distribution of the partons change with energy, one must specify a *factorisation scale*, the energy to which the parton distributions are calculated.

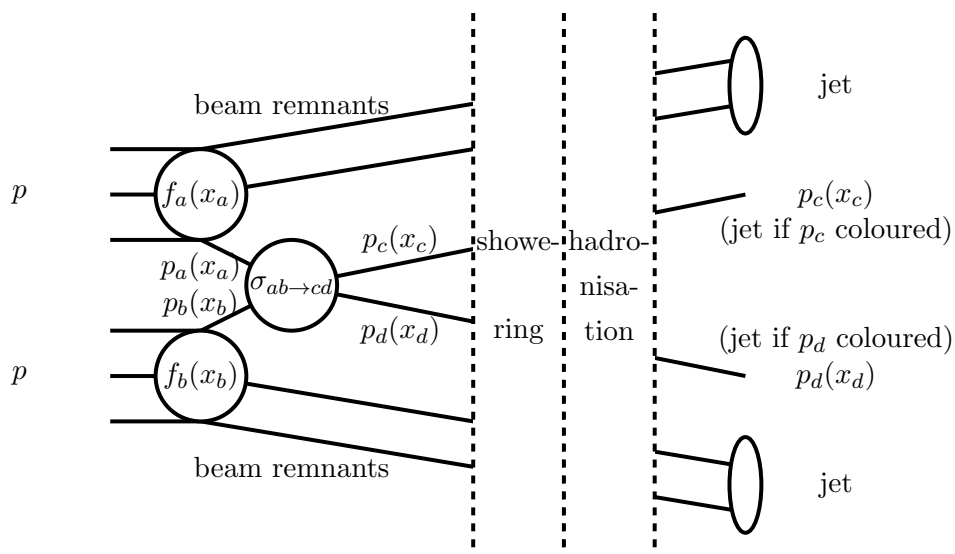


Figure 2.4: Schematic view of a proton-proton collision

The end result is, that the matrix element obtained from a given process is not the final result in a proton-proton collision. One must include how likely it is to extract a specific parton from the proton at a given energy. This results in multiplying the differential cross section with a probability factor known as the parton density functions (PDFs). At short distances (or large energy) the quantum effects inside the proton can be ignored, meaning that one can assume that the proton wave function is constant over the distance where the hard scattering process happens. If the wavefunction is not constant over the hard scattering process, quantum effects must be included, meaning that the PDFs no longer can describe the constituents of the protons. The quantum effects could be new virtual particles emerging inside the proton, interfering with the parton involved in the hard scattering, eg. by changing the momenta of the scattering parton.

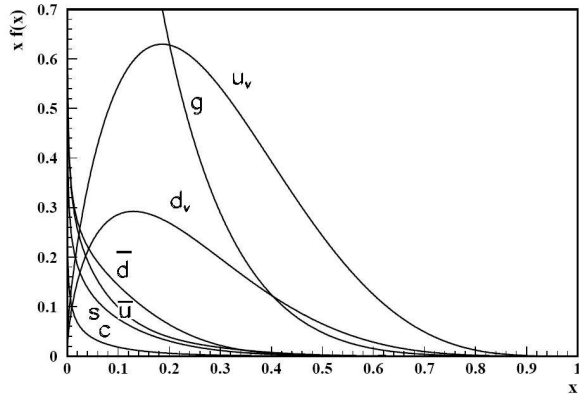


Figure 2.5: Distributions for partons inside a proton at different momentum fractions $x = \frac{p_{parton}}{p_{proton}}$ carried by the parton [7].

From the PDFs one can determine what fraction of the total momentum of the proton each parton carries at a given energy scale and from here calculate the cross section at hadron colliders [7]:

$$x = \frac{p_{parton}}{p_{hadron}}$$

$$\sigma_X = \sum_{a,b} \int_0^1 dx_1 dx_2 f_a(x_1, \mu_F^2) f_b(x_2, \mu_F^2) \times \sigma_{ab \rightarrow X}(x_1, x_2, p_i^\mu, \alpha_S(\mu_R^2), \alpha(\mu_R^2), \frac{Q^2}{\mu_R^2}, \frac{Q^2}{\mu_F^2})$$

with Q^2 being the energy scale probed, $\alpha_{S(EW)}$ is the strong (weak) coupling constant at a given energy scale, $\mu_{F(R)}$ being the factorisation (renormalisation) scale.

The cross section should in principle not rely on the factorisation scale μ_F nor the renormalisation scale μ_R . The calculation of the cross section is performed by using perturbation theory, thus if calculated to all orders the scale dependence will vanish and the cross section goes towards the 'true' value. But at leading order one expects the choice of scales to affect the results. Including higher order corrections decreases the effects of the scale choice and the result should become more precise.

If no (or only a limited set of) higher order corrections are present, one must estimate the error on the scale choice. Normally one chooses $\mu_R^2 = \mu_F^2 = Q^2$, with Q being the energy scale of your choice. A variation of the scales is then performed choosing $0.25\mu_R^2 = 4\mu_F^2 = Q^2$ and then evaluating the cross section at this scale. Then the reverse scaling is performed choosing $4\mu_R^2 = 0.25\mu_F^2 = Q^2$ and evaluating the cross section at this scale. The error on the cross section at the initial value is then half of the sum of the two divided with the initial value [8].

The PDFs are denoted f_a, f_b in the above, and tend to go as follows [7]:

$$f_{valence} \propto (1-x)^3 \qquad f_{sea} \propto (1-x)^7 \qquad f_{gluon} \propto (1-x)^5$$

There exists numerous ways of parametrizing the density functions, each having a connected theoretical uncertainty. Thus the choice of PDF could affect your final result and it should always be noted what choice one has taken and if possible an error estimate on the PDF choice should be calculated.

2.4 Next to leading order corrections

The first sections only describes the leading order description of a process. But at high energy scales one can imagine situations where virtual particle- antiparticle pairs can interfere with the scattering particles in the process diagrams. Gluons can also be emitted from the quarks either to combine with another quark line or showing up as jets in the system. All of these processes are denoted next-to-leading order (NLO) and are crucial for the full understanding of any process, when colliding particles at very high energies. There are two types of next-to-leading order corrections: QCD corrections, where the process is kept at the same order in couplings as the leading order process has, but increased in the order of α_S (eg. add gluons to the system), or electroweak corrections, where the process is increased the order of α (eg. make loops without gluons). The former is vastly used and in some processes even NNLO and NNNLO corrections have been made. The latter is less used, since it is much more likely to emit gluons from quark lines, than it is to create a massive quark/lepton/boson pair. But at LHC these situations exist, and a full next-to-leading order correction would need to include these diagrams along with the QCD corrections.

Whenever an additional virtual particle is added to a diagram, the Feynman rules describe that we must add an additional propagator to the matrix element. This propagator carries a virtual momentum, and it must be integrated out such that there still is overall momentum conservation. This results in expressions of integrals over the propagators, with the most basic given as:

$$\int \frac{d^4p}{(2\pi)^4} \frac{1}{p^2 - m^2}$$

This integral is divergent when $p^2 \rightarrow m^2$. All propagators are of this form, some even has instances of momentum in the numerator, such as the fermion propagator has. This poses a huge problem for the quantum field theory, since the measurable quantities are calculated from the matrix elements, many of which individually diverge. One could then imagine that the total sum of diagrams, the total process amplitude, could diverge. And thus one cannot predict anything beyond leading order, if these divergencies cannot be fixed.

Fortunately there exist a fix. The starting point when handling next-to-leading order processes is thus to locate the point, where the integral diverges. This method is called *regularisation*, and will be described in the next section. Once the points have been located, in which the integral diverges (the poles,) one can proceed to *renormalise* the theory. This is a method of absorbing the divergencies into the constants of the theory making the renormalised theory finite. This procedure and its effects will be described last in the last section. But before entering into these mathematical formulations, a short description of the divergencies in a quantum field theory is given.

2.4.1 Divergencies in next-to-leading order corrections

The divergencies occurring in the (next-to-leading order) momentum integrals can be classified into two categories, ultraviolet (UV) divergencies and infrared (IR) divergencies. Each divergency occurs on account of different reasons. The UV divergencies arise from the short distance or high energy behaviors of the loop integrals, and result from an attempt to apply our theory to an energy scale beyond its applicability. The IR divergencies are low energy or long distance behaviors of loop integrals or from real emission processes [4]. They are present only if the theory has massless particles.

These divergencies need fixing, otherwise one will end up with non-physical results. When the mathematical formulation has been developed the result is one of two scenarios: 'Fake' divergencies that cancel between diagrams and 'true' divergencies that needs fixing. IR divergencies always cancel within the theory, but usually UV divergencies will not. Hence one must renormalise the UV divergencies in order to make the theory finite.

The matrix element for the next-to-leading order process is a sum of the tree level, one loop and real emission diagrams, resulting in

$$\mathcal{M}_{NLO} = \mathcal{M}_{tree} + \mathcal{M}_{one-loop} + \mathcal{M}_{real}$$

where, strictly speaking, the real emission part has a different phase-space than the other two parts, since it has an extra particle in the final state. Thus, when calculating cross sections, this must be taken into account by integrating over another set of phase-space points. When calculating these cross sections, the matrix element must be squared:

$$\begin{aligned} \sigma_{NLO} &\sim \int_N |M_{NLO}|^2 \\ &= \int_N |\mathcal{M}_{tree} + \mathcal{M}_{one-loop} + \mathcal{M}_{real}|^2 \\ &= \int_N \mathcal{M}_{tree}^* \mathcal{M}_{tree} + \mathcal{M}_{one-loop}^* \mathcal{M}_{tree} + \mathcal{M}_{real}^* \mathcal{M}_{tree} + \mathcal{O}(g^2) \\ &= \int_N |\mathcal{M}_{tree}|^2 + \int_N |\mathcal{M}_{one-loop}|^2 + \int_{N+1} |\mathcal{M}_{real}|^2 + \mathcal{O}(g^2) \end{aligned}$$

where N denotes the number of particles in the final state. The one-loop matrix element squared and the real emission squared is not included, since these are a higher order in couplings than the other parts, and are then NNLO corrections. We can now have two terms of the cross section separately diverge, the interference term and the real emission term. When calculated properly the IR divergencies should cancel, but the cancellation is far from trivial, since the phase-space of the two parts giving IR-divergencies are different. To solve this a method of subtraction is used, where a well-chosen function F is added and subtracted to the integrals. For the real emission parts it is used to subtract out the divergent terms in the $(N + 1)$ phase-space and added to the interference terms, where it is integrated over the one particle phase-space.

$$\sigma_{NLO} \sim \int_N |\mathcal{M}_{tree}|^2 + \left(\int_N |\mathcal{M}_{one-loop}|^2 + \int_1 F \right) + \int_{N+1} (|\mathcal{M}_{real}|^2 - F)$$

Each of the terms are now individually IR finite and can be evaluated separately. The interference terms containing the UV divergencies will usually be highly non-trivial integrals and a ranking method has been developed [9] to separate the integrals into classes depending on the numerators. The numerator is split into two categories: *rank- r tensor integrals* with r instances of loop momenta in the numerator (eg. a fermion loop), and *scalar integrals* with no loop momenta in the numerator (eg. a photon loop or a scalar loop). The higher rank

the tensor integral has, the more difficult it is to evaluate.

Most times the matrix elements of a next-to-leading order process are so vast and difficult, that they cannot be evaluated analytically. But some of the integrals can, thus when evaluating loop integrals one always tries to reduce them to integrals that are possible to evaluate analytically. If the analytical evaluation is not possible, numerical evaluation must be done. Hence most next-to-leading order calculations are done by computer programs with hard-coded integral libraries.

In this thesis such a program is used. It is based on the integral libraries Golem95 [10] and Samurai [11], combining the two into a program called GoSam [9]. Each of the integral libraries has its preferred way of reducing the loop integrals and evaluating them. Both libraries use the dimensional regularisation scheme to locate the poles in the matrix element before renormalising the lagrangian and evaluating the integrals.

2.4.2 Making the divergent theory finite

The starting point is to locate the divergent poles in the theory. The method of dimensional regularisation (DR) can be used on both IR and UV divergencies, and respects both lorentz and gauge invariance. Instead of computing the virtual loop momentum integrals in $d = 4$ dimensions, one uses the fact that for sufficiently small dimensions d , any loop momentum integral will converge [4]. The change from 4 to $d = 4 - \varepsilon$ dimensions thus allows for an evaluation of the divergent integral [4]:

$$\begin{aligned} \int \frac{d^4 p}{(2\pi)^4} \frac{1}{p^2 - m^2} &\rightarrow \int \frac{d^d p}{(2\pi)^d} \frac{1}{p^2 - m^2} \\ &= \frac{-i}{(4\pi)^{d/2}} \frac{\Gamma(1 - d/2)}{\Gamma(1)} \left(\frac{1}{m^2}\right)^{1-d/2} \\ &= -i \frac{\Gamma(1 - \frac{4-\varepsilon}{2})(m^2)^{(4-\varepsilon)/2-1}}{(4\pi)^{(4-\varepsilon)/2}} \\ &= -i \Gamma(\varepsilon/2 - 1)(m^2)^{1-\varepsilon/2} (4\pi)^{\varepsilon/2-2} \\ &= -i \Gamma(\varepsilon/2 - 1) \frac{m^2}{(4\pi)^2} \left(\frac{4\pi}{m^2}\right)^{\varepsilon/2} \end{aligned}$$

The poles of the gamma function are known⁷, and thus the poles of the result can be located. For $\varepsilon \ll 1$ one can make use of the approximation [4]

$$\Gamma(\varepsilon/2 - 1) \approx \frac{2}{\varepsilon} - \gamma + \mathcal{O}(\varepsilon)$$

where γ is the Euler-Mascheroni constant⁸. The expansion of the mass term becomes [4]

$$\frac{m^2}{(4\pi)^2} \left(\frac{4\pi}{m^2}\right)^{\varepsilon/2} \approx \frac{m^2}{(4\pi)^2} \left(1 - \frac{\varepsilon}{2} \ln \left[\frac{4\pi}{m^2}\right] + \mathcal{O}(\varepsilon^2)\right)$$

⁷ $\Gamma(x) = \int_0^\infty t^{x-1} e^{-t} dt$ with poles at $x = 0, -1, -2 \dots$

⁸ $\gamma \simeq 0.5772$

Collecting the terms one obtains in the limit $\varepsilon \rightarrow 0$:

$$\begin{aligned} \int_{-\infty}^{\infty} \frac{d^d p}{(2\pi)^d} \frac{1}{p^2 - m^2} &= -i\Gamma(\varepsilon/2 - 1) \frac{m^2}{(4\pi)^2} \left(\frac{4\pi}{m^2}\right)^{\varepsilon/2} \\ &= -i \frac{m^2}{(4\pi)^2} \left(\frac{2}{\varepsilon} - \gamma + \mathcal{O}(\varepsilon)\right) \left(1 - \frac{\varepsilon}{2} \ln \left[\frac{4\pi}{m^2}\right] + \mathcal{O}(\varepsilon^2)\right) \\ &= -i \frac{m^2}{(4\pi)^2} \left(\frac{2}{\varepsilon} - \ln \left[\frac{4\pi}{m^2}\right] - \gamma + \mathcal{O}(\varepsilon)\right) \end{aligned}$$

Thus the pole⁹ has been located and needs to be cancelled by renormalisation. Otherwise all quantities are convergent and thus physical and meaningful. The method of renormalisation introduces counterterms to the lagrangian exactly cancelling the divergent pole. Subtracting the counterterms from the original lagrangian, the divergencies vanish and the renormalised lagrangian is finite. The subtraction method requires a reformulation of the terms involved in the lagrangian. This reformulation creates scale-dependent coupling 'constants', having interesting effects on our theory.

Various methods of subtraction exists, but in the method used in this thesis is modified minimal subtraction (\overline{MS}). Here one chooses to subtract factors of $\frac{1}{\varepsilon} = \frac{1}{\varepsilon} - \gamma + \log(4\pi)$ from the original lagrangian. The \overline{MS} will be used on the divergent integral from the above, but with an additional coupling:

$$\mathcal{M} = -\mu^\varepsilon \lambda \times \int \frac{d^d q}{(2\pi)^d} \frac{1}{q^2 - m^2} \Rightarrow \int_{-\infty}^{\infty} \frac{d^d p}{(2\pi)^d} \frac{\mu^\varepsilon \hat{\lambda}}{p^2 - m^2} = i\hat{\lambda} \frac{m^2}{(4\pi)^2} \left(\frac{2}{\varepsilon} - \ln \left[\frac{4\pi\mu^2}{m^2}\right] - \gamma + \mathcal{O}(\varepsilon)\right)$$

Assuming the divergent integral arises in scalar $\hat{\lambda}\phi^3$ theory, then the diagram containing the integral is the tadpole diagram:

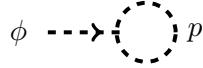


Figure 2.6: The tadpole diagram in $\hat{\lambda}\phi^3$ theory.

Adding terms to the original $\hat{\lambda}\phi^3$ lagrangian matching the pole cancel the divergencies.

$$\begin{aligned} \mathcal{L}(\phi, m, \lambda) &= \frac{1}{2}(\partial_\mu \phi)^2 + \frac{1}{2}m^2\phi^2 + \frac{1}{3!}\lambda\phi^3 \\ \mathcal{L}_{ct}(\phi, m, \lambda, \mu, \varepsilon) &= \frac{C}{2}(\partial_\mu \phi)^2 + \frac{B}{2}m^2\phi^2 + \frac{A}{3!}\mu^\varepsilon\lambda\phi^3 \\ \mathcal{L}_R(\phi_0, m_0, \lambda_0) &= \mathcal{L}(\phi, m, \lambda) - \mathcal{L}_{ct}(\phi, m, \lambda, \mu, \varepsilon) \\ &= \frac{1}{2}(\partial_\mu \phi_0)^2 + \frac{1}{2}m_0^2\phi_0^2 + \frac{1}{3!}\lambda_0\phi_0^3 \end{aligned}$$

where the renormalised parameters are:

$$\begin{aligned} \phi_0 &= \sqrt{1 - C}\phi \equiv \sqrt{Z_\phi}\phi \\ m_0^2 &= \frac{m^2(1 + B)}{Z_\phi} \\ \lambda_0^2 &= \frac{\mu^\varepsilon\lambda(1 + A)}{\sqrt{Z_\phi}} \end{aligned}$$

with $A, B, (C > 1)$ arbitrary. Obtained is a fully functioning finite lagrangian at hand, from where one can obtain new Feynman rules and recalculate matrix elements for finite results.

⁹ $\frac{1}{\varepsilon} \rightarrow \infty$ for $\varepsilon \rightarrow 0$ (which is the same as $d \rightarrow 4$)

2.5 Running couplings

The renormalised couplings are now explicitly dependent on μ , the renormalisation scale. Denoting the unrenormalised coupling as λ , we can write the physical couplings as a function of the unrenormalised couplings, the renormalisation scale and the regulator [4], ie. $\hat{\lambda} = f(\lambda, \mu, \varepsilon)$. This equation is known as the renormalisation group equation. It gives information on how the flow of the coupling behaves at various energies. If measured at a certain energy, $\hat{\lambda}(\mu = Q)$, we can by using the renormalisation group equations extrapolate the value of $\hat{\lambda}$ at different energies [4].

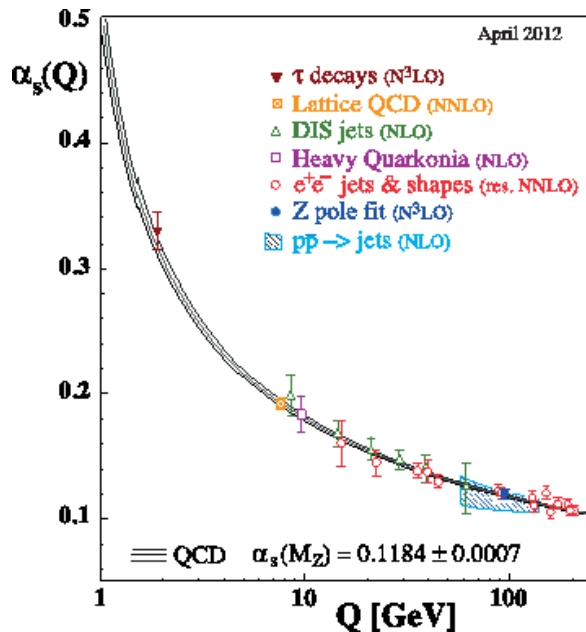


Figure 2.7: The running of α_S at different energies [6]

The flow of the couplings varies depending on which theory one investigates. As an example QED and the electroweak theories both have flows slowly increasing from low coupling values at low energies towards slightly higher coupling values at higher energies. Because the flow is slow the couplings will be weak at all experimentally relevant energies. This means that the perturbative Feynman approach can always be used.

On the other hand, the value of the QCD coupling decrease with increasing energy. Thus the perturbative method is not valid at low energies, resulting in the confinement of the quarks. At higher energies the coupling decreases fast, thus allowing for a perturbative description of QCD.

The flow equations can be used on any coupling, even if the lagrangian itself is not renormalisable. This allows for studying the flow of the couplings to see if a model behaves 'well' at different energy scales. If the model exhibits signs of improper behaviour at either low or high energy scales, it must be revisited to see if the improper behaviour can be controlled.

2.6 Classification of the renormalisabilities

With the description of the integrals in the renormalised scheme, the poles have been located in our lagrangian. This allows for a counting of UV divergencies and a further classification of a quantum field theory in the renormalisation scheme [4]:

- Super-Renormalisable QFTs: A finite number of Feynman diagrams diverge (or: The coupling constants of the theory have a positive mass dimension).

- Renormalisable QFTs: A finite number of amplitudes diverge, but divergencies occur in all orders of perturbation (or: The coupling constants of the theory are dimensionless).
- Non-Renormalisable QFTs: All amplitudes are divergent at high orders in perturbation theory (or: The coupling constants of the theory have a negative mass dimension)

Take QED as an example: In $d < 4$ all couplings have a positive mass dimension, hence the theory is super-renormalisable here. In $d = 4$ the dimension of e is zero, making the theory renormalisable. In higher dimensions e will have a negative mass dimension, making it non-renormalisable.

Once the lagrangian has been renormalised only IR singularities remain. These are consequences of our theory having massless particles, in the form of photons and gluons. The remaining singularities in both the virtual and real corrections arise from *soft* and *collinear* massless particles, soft denoting particles with a momentum smaller than some cut, while collinear denotes the particles radiated along one of the final state particles, such that it visually cannot be separated from the final state particle. The divergencies have to be treated individually but when properly done will cancel. A full description is beyond the scope of this thesis, but a very good introduction is given in [12].

The new physics (or beyond the-Standard Model, BSM) model used in this thesis, is a non-renormalisable theory. In order to generate all vertices needed in the model, one must introduce operators of mass dimension eight. The couplings must then have a negative mass dimension to make the action dimensionless, hence making it impossible to renormalise the theory. The couplings also exhibit signs of improper high energy behavior, such that it must be revisited. But more on this later.

Anomalous triple gauge boson couplings

In this section the concepts of the BSM model, the anomalous triple gauge boson couplings, are introduced. The particle content of the theory is the physical gauge bosons, and the symmetry of the theory is Lorentz symmetry. Based on this the most general lagrangian for three boson interactions can be obtained, and was first written in 1983 by Hagiwara et. al. exploring the $e^+e^- \rightarrow W^+W^-$ process for use at LEP [13]. In the paper the authors added the vertex for the ZZ and $Z\gamma$ production as well. But it should be noted, that the literature on these neutral couplings differs a bit (signs and factors of i) on the lagrangian and the Feynman rules coming out of this lagrangian.

The interactions amongst gauge bosons provide an efficient test of the Standard Model, since the model predicts interactions in a very specific way: Only WWZ and $WW\gamma$ interactions are allowed in the Standard Model, and the strengths of the couplings are proportional to the electric charge (and the cotangent of the weak mixing angle in the WWZ vertex). This is completely determined by the symmetries of the Standard Model and one can thus by studying this vertex obtain valuable information of the symmetries of the Standard Model.

Deviations from the Standard Model would imply that the group structure of the theory is not the structure expected. One can then wonder what the group structure is and what effect the symmetries connected to the group will have. But this will be a model-dependent way of looking for new physics. If one instead choses a model independent way of looking for new physics, one must write down the most general lagrangian for the particle content and the symmetry group and relate this to how particles would interact and behave under this new theory.

In this section I will use the physical basis for the electroweak bosons and will describe both the charged and the neutral pair productions in detail. Unless otherwise stated the contents in this section have been inspired by [13].

From the Standard Model electroweak lagrangian one can extract the terms where three bosons interact with each other [2]:

$$\begin{aligned} L_{WWZ} &= -ie \cot \theta_W \cdot (W_{\mu\nu}^+ W^{-\mu} Z^\nu - W_{\mu\nu}^- W^{+\mu} Z^\nu + W_\mu^+ W_\nu^- Z^{\mu\nu}) \\ L_{WWA} &= -ie \cdot (W_{\mu\nu}^+ W^{-\mu} A^\nu - W_{\mu\nu}^- W^{+\mu} A^\nu + W_\mu^+ W_\nu^- A^{\mu\nu}) \end{aligned}$$

where $V_{\mu\nu} = \partial_\mu V_\nu - \partial_\nu V_\mu$. These are the only allowed three boson vertices in the Standard Model. However, one can expand this to include other lorentz invariant terms. The full lagrangian for on-shell¹ boson pair production reads:

¹ $p^2 = m^2$

$$L_{VVV} = L_{WWV} + L_{ZVV}$$

where

$$\begin{aligned} L_{WWV} = g_{WWV} \cdot & \left[ig_1^V \cdot (W_{\mu\nu}^+ W^{-\mu} V^\nu - W_\mu^+ Z_\nu W^{-\mu\nu}) + i\kappa_V W_\mu^+ W_\nu^- V^{\mu\nu} + \right. \\ & \frac{i\lambda_V}{M_W^2} W_{\lambda\mu}^+ W_\nu^{-\mu} V^{\nu\lambda} - g_4^V W_\mu^+ W^{-\nu} (\partial^\mu V^\nu + \partial^\nu V^\mu) + \\ & \left. g_5^V \epsilon^{\mu\nu\rho\sigma} (W_\mu^+ \overleftrightarrow{\partial}_\rho W_\nu^-) V_\sigma + i\tilde{\kappa}_V W_\mu^+ W_\nu^- \tilde{V}^{\mu\nu} + \frac{i\tilde{\lambda}_V}{M_W^2} W_{\lambda\mu}^+ W_\nu^{-\mu} \tilde{V}^{\nu\lambda} \right] \\ L_{ZVV} = -\frac{e}{M_Z^2} \cdot & \left[f_4^V \partial_\mu V^{\nu\beta} Z_\alpha \partial^\alpha Z_\beta - f_5^V \partial^\sigma V_{\sigma\mu} \tilde{Z}^{\mu\beta} Z_\beta + \right. \\ & h_1^V \partial^\sigma V_{\sigma\mu} Z_\beta A^{\mu\beta} + h_3^V \partial_\sigma V^{\sigma\rho} Z^\alpha \tilde{A}_{\rho\alpha} + \\ & \left(\frac{h_2^\gamma}{M_Z^2} \partial_\alpha \partial_\beta \partial^\rho A_{\rho\mu} + \frac{h_2^Z}{M_Z^2} \partial_\alpha \partial_\beta (\partial^\lambda \partial_\lambda + M_Z^2) Z_\mu \right) Z^\alpha A^{\mu\beta} - \\ & \left. \left(\frac{h_4^\gamma}{2M_Z^2} \partial^\lambda \partial_\lambda \partial^\sigma A^{\rho\alpha} + \frac{h_4^Z}{2M_Z^2} (\partial^\lambda \partial_\lambda + M_Z^2) \partial^\sigma Z^{\rho\alpha} \right) Z_\sigma \tilde{A}_{\rho\alpha} \right] \end{aligned}$$

where $V = Z, \gamma$, $V_{\mu\nu} = \partial_\mu V_\nu - \partial_\nu V_\mu$ (likewise for A and Z), $\tilde{V}^{\mu\nu} = \frac{1}{2} \epsilon^{\mu\nu\alpha\beta} V_{\alpha\beta}$ (likewise for A and Z) and last $A \overleftrightarrow{\partial}_\mu B = A(\partial_\mu B) - (\partial_\mu A)B$. This lagrangian exhausts all possible lorentz invariant combinations and thus can be described as the full three boson vertex generating lagrangian.

The first line in L_{WWV} can be recognised as the Standard Model triple boson vertex lagrangian, and one fixes the coupling constants such that $g_{WW\gamma} = -e$ and $g_{WWZ} = -e \cot \theta_W$. The coupling constants $g_i^V, \kappa_V, \lambda_V, \tilde{\lambda}_V, \tilde{\kappa}_V, f_j^V, h_k^V$, where $i = 1, 4, 5, j = 4, 5$ and $k = 1 \dots 4$ are known as *triple gauge boson couplings* (TGC's) and one usually distinguishes between the charged TGC's belonging to L_{WWV} and the neutral TGC's belonging to L_{ZVV} . Of these only g_1^V and κ_V are non-zero in Standard Model and have the specific value of one.

In general these couplings are complex numbers, for which the imaginary part is the absorbtive part of the vertex function. These parts could in principle modify the complete diboson pair production amplitude. In the models used in this thesis all the TGC's are allowed to be complex numbers, thus allowing for this absorbtion. But in the calculation below, the couplings are assumed to be real, for simplicity.

The process under consideration in this thesis is $q\bar{q} \rightarrow ZZ \rightarrow e^+e^-\mu^+\mu^-$. This is an allowed process in the Standard Model, but by introducing the TGC lagrangian BSM effects can be taken into account. The section begins with the calculation of the matrix element for the on-shell process and explores the effects the BSM physics have on the matrix element as well as the differential cross section. It then proceeds to discuss the operator expansion of the TGC lagrangian, and a discussion of the high energy behaviour of the couplings. Then comes a discussion of including off-shell contributions to the process and how this relates the TGCs to each other. Finally the section ends with a description of another Standard Model process also giving rise to Z pair production before the next-to-leading order corrections are taken into account. These next-to-leading order corrections are particularly interesting in this channel, since they have never been explored before. A subset of the charged TGC sector includes real emission and virtual corrections, but the neutral ZZ TGC sector has never been explored beyond leading order.

3.1 Leading order helicity amplitudes for $q\bar{q} \rightarrow ZZ \rightarrow e^+e^-\mu^+\mu^-$

In this section the mathematical formulation of the matrix element used in this thesis is given. The matrix element is given in the helicity framework, such that the effects of the matrix element can be studied in each of the helicity configurations, before a sum over the Z helicities is performed to obtain a physical prediction. The helicity is generally speaking the projection of the spin of the particle onto the direction of the momentum vector, $\hat{h} = \vec{S} \cdot \hat{p}$. A particle with a positive helicity is said to be right-handed, while a particle with negative helicity is said to be left-handed. These concepts were introduced as components of the fermions² in Sec. 2.2.4 and it was shown that the W bosons only interact with the lefthanded part of the fermion doublet. Hence by writing the matrix element in the helicity formalism one can explicitly see the allowed interactions between the fermions and bosons. But since the physical particles are a combination of these helicity states, the sum over all possible helicities must be performed in the end.

One must also remember that massless particles only have two possible helicity states, the left and righthanded states. Massive particles on the other hand have a third possibility, the zero helicity. This means there is an additional component one has to take into account. Thus the combinatorics in the Z pair production results in nine Z helicity configurations: $(++, +-, +0, 00, 0+, 0-, -, -+, -0)$. The matrix element has to cover these combinations, but as we shall see, some combinations vanish and some are so small, they can be summed.

In the helicity framework the matrix element reduces to a set of complex matrices. By choosing an appropriate basis one can simplify the matrix element and study the helicity configurations in detail, before the sum is performed. This is also done in this section, where the angular distributions of the Z bosons are studied in the different helicity configurations. After this study the additional lepton decay matrix element is added and the complete matrix element for the process $q\bar{q} \rightarrow ZZ \rightarrow e^+e^-\mu^+\mu^-$ is presented.

As a starting point, the Feynman diagrams for the production of two Z bosons and their further decay into lepton pairs are shown in Fig. 3.1.

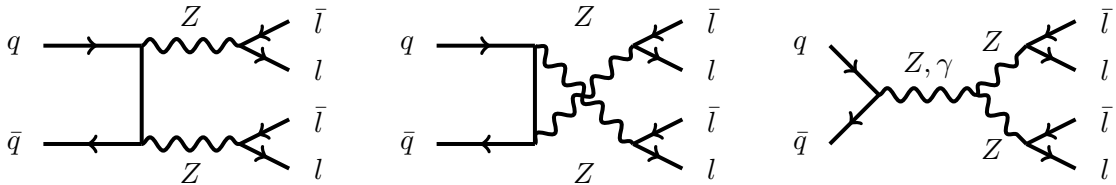


Figure 3.1: Tree level diagrams of Z boson pair production excluding diagrams with the Higgs. The two first diagrams are the Standard Model contribution, while the last includes the TGC vertex, not allowed in the Standard Model.

These four diagrams are the only on-shell tree level diagrams, if Higgs diagrams are excluded. This set of diagrams are denoted double resonant diagrams, since two bosons (or two resonances) are created at the same time. The single resonant diagram (a quark pair annihilating into a Z boson, decaying into a lepton pair, which then radiates a Z boson that further decays into a lepton pair) can also result in the production of two Z bosons, but this is excluded in the present section. The TGC vertex is only present in the last diagram(s) resulting in the interaction between the two Z bosons and another off-shell intermediate boson (Z^*, γ^*). Using the Feynman rules from [3] presented in Fig. 3.2 on the next page, the

²It was actually seen that the components of the fermions were the chirality states, but the two concepts are similar. The chirality is an intrinsic and conserved feature, while the helicity can change of a massive particle. But for massless particles the two concepts are equal.

Feynman diagrams can be converted into a matrix element.

$$\begin{array}{l}
 f \\
 \nearrow \\
 \bullet \\
 \nwarrow \\
 \bar{f}
 \end{array}
 V_\mu \quad VF\bar{F} = ie\gamma_\mu \left(C_L \frac{1-\gamma^5}{2} + C_R \frac{1+\gamma^5}{2} \right)$$

$$\begin{array}{l}
 V_\nu \\
 \nearrow \\
 \bullet \\
 \nwarrow \\
 V_\mu
 \end{array}
 V_\alpha \quad VVV = ie\Gamma_{VVV}^{\alpha\mu\nu}$$

$$\begin{array}{l}
 f \longrightarrow \bullet \\
 \bar{f} \longleftarrow \bullet \\
 V \text{ (wavy)} \bullet
 \end{array}
 \quad
 \begin{array}{l}
 F_{ij} = \frac{i(\not{p}+m)}{p^2-m^2+i\epsilon} \delta_{ij} \\
 V_{\mu\nu} = \frac{-i(g^{\mu\nu} - (\xi-1) \frac{p_\mu p_\nu}{p^2 - \xi M_V^2 + i\epsilon})}{p^2 - M_V^2 + i\epsilon}
 \end{array}$$

$$\begin{array}{l}
 f \longrightarrow \bullet \\
 \bar{f} \longleftarrow \bullet \\
 V \text{ (wavy)} \bullet
 \end{array}
 \quad
 \begin{array}{l}
 u(p) \\
 \bar{v}(p) \\
 \varepsilon_\mu(p)
 \end{array}$$

$$\begin{array}{l}
 f \longrightarrow \bullet \\
 \bar{f} \longleftarrow \bullet \\
 V \text{ (wavy)} \bullet
 \end{array}
 \quad
 \begin{array}{l}
 \bar{u}(p) \\
 v(p) \\
 \varepsilon_\mu^*(p)
 \end{array}$$

Figure 3.2: The Feynman rules needed in the process $q\bar{q} \rightarrow ZZ \rightarrow 4l$ [3].

The choice of gauge can vary. The present formulation allow for $\xi = 1$ (Feynman gauge) and $\xi = 0$ (Landau gauge), with the Feynman gauge reducing the instances of momenta in the boson propagator. This will in turn simplify the calculations a lot, especially when the next-to-leading order corrections are taken into account. The left- and righthanded fermion-boson interaction terms in the vertex rules are [3]:

$V\bar{F}_1F_2$	$Af_i f_j$	$Zf_i f_j$	$W^+ \bar{u}_i d_j$	$W^- d_i u_j$	$W^+ \bar{\nu}_i l_j$	$W^- l_i \nu_j$
C_L	$-Q\delta_{ij}$	$g_f^- \delta_{ij}$	$\frac{1}{\sqrt{2}\sin\theta_W} V_{ij}$	$\frac{1}{\sqrt{2}\sin\theta_W} V_{ij}^\dagger$	$\frac{1}{\sqrt{2}\sin\theta_W} \delta_{ij}$	$\frac{1}{\sqrt{2}\sin\theta_W} \delta_{ij}$
C_R	$-Q\delta_{ij}$	$g_f^+ \delta_{ij}$	0	0	0	0

Table 3.1: The coefficients C_L, C_R in different interactions. Here $g_f^- = \frac{I_3 - \sin^2\theta_W Q}{\sin\theta_W \cos\theta_W}$, $g_f^+ = -\frac{\sin\theta_W Q}{\cos\theta_W}$.

where the explicit non-interaction between the W boson and the righthanded fields are seen.

The Feynman rules, $\Gamma_{VVV}^{\alpha\mu\nu}$, for the TGC vertex is given in [14], where P is the ingoing momentum and q_1, q_2 are the outgoing momenta:

$$\Gamma_{ZZV}^{\alpha\beta\mu}(q_1, q_2, P) = \frac{s - M_V^2}{M_Z^2} [if_4^V (P^\alpha g^{\mu\beta} + P^\beta g^{\mu\alpha}) - if_5^V \epsilon^{\mu\alpha\beta\rho} (q_1 - q_2)_\rho]$$

It should be noted here, that the version of the ZZV vertex rule from [14] differs from the original version in [13]. The vertex rule from [14] differs in sign in front of f_5^V as well as in the $Z\gamma V$ couplings h_3^V, h_4^V and has introduced an additional factor of i in order for the new physics lagrangian to be hermitian³ [14]. This will require an effort when comparing the matrix elements against matrix elements obtained with the vertex rule from [13], but more on this later.

Specifying the momenta (k_i, q_i, p_i) and helicities $(\sigma_i, \lambda_i, \rho_i)$ of the particles involved in the process, the full matrix element, \mathcal{M} , is [13]:

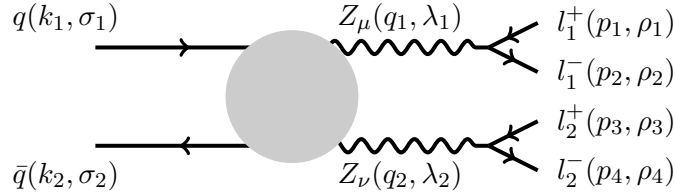


Figure 3.3: Z pair production with momenta and helicities for all particles.

$$\begin{aligned} \mathcal{M}(q\bar{q} \rightarrow l_1^+ l_1^- l_2^+ l_2^-) &= Z_{\alpha\mu}(q_1^2) Z_{\beta\nu}(q_2^2) \sum_{\lambda_1} \sum_{\lambda_2} \mathcal{M}(q\bar{q} \rightarrow Z_\alpha Z_\beta) \cdot \mathcal{M}(Z_\mu \rightarrow l_1^+ l_1^-) \cdot \mathcal{M}(Z_\nu \rightarrow l_2^+ l_2^-) \\ &= Z_{\alpha\mu}(q_1^2) Z_{\beta\nu}(q_2^2) \sum_{\lambda_1} \sum_{\lambda_2} [\mathcal{M}_t + \mathcal{M}_u + \mathcal{M}_{ZZZ} + \mathcal{M}_{\gamma ZZ}] \cdot \\ &\quad \mathcal{M}(Z_\mu \rightarrow l_1^+ l_1^-) \cdot \mathcal{M}(Z_\nu \rightarrow l_2^+ l_2^-) \end{aligned}$$

with $\mathcal{M}(q\bar{q} \rightarrow Z_\alpha Z_\beta)$ being the amplitude for the production of the Z-bosons, $\mathcal{M}(Z_\mu \rightarrow l_1^+ l_1^-)$ being the amplitude for a Z-boson decaying into a lepton pair and $Z_{\mu\nu}(p^2) = (p^2 - M_Z^2 + iM_Z\Gamma_Z)^{-1}$ being the Breit-Wigner propagator factor. This propagator factor allows the Z bosons to be off-shell, but as the function decreases as p^2 departs from the Z mass, the probability of creating an off-shell Z boson also decreases. Denoting a vertex as $[P_1 P_2 P_3]$, the production matrix element becomes:

$$\begin{aligned} \mathcal{M}_t &= \bar{\psi}(k_2, \sigma_2) [Z_\beta q\bar{q}] \varepsilon_\beta^*(q_2, \lambda_2) F_q(k_1 - q_1) [Z_\alpha q\bar{q}] \varepsilon_\alpha^*(q_1, \lambda_1) \psi(k_1, \sigma_1) \\ \mathcal{M}_u &= \bar{\psi}(k_2, \sigma_2) [Z_\alpha q\bar{q}] \varepsilon_\alpha^*(q_1, \lambda_1) F_q(k_1 - q_2) [Z_\beta q\bar{q}] \varepsilon_\beta^*(q_2, \lambda_2) \psi(k_1, \sigma_1) \\ \mathcal{M}_{ZZZ} &= \bar{\psi}(k_2, \sigma_2) [Z_\beta q\bar{q}] Z_{\beta\alpha}(k_1 + k_2) \Gamma_{ZZZ}^{\alpha\mu\nu} \varepsilon_\mu^*(q_1, \lambda_1) \varepsilon_\nu^*(q_2, \lambda_2) \psi(k_1, \sigma_1) \\ \mathcal{M}_{ZZ\gamma} &= \bar{\psi}(k_2, \sigma_2) [A_\beta q\bar{q}] A_{\beta\alpha}(k_1 + k_2) \Gamma_{\gamma ZZ}^{\alpha\mu\nu} \varepsilon_\mu^*(q_1, \lambda_1) \varepsilon_\nu^*(q_2, \lambda_2) \psi(k_1, \sigma_1) \end{aligned}$$

³A hermitian matrix (or lagrangian) is a complex matrix that is equal to its own conjugate transpose, ie. that $\mathcal{A} = \mathcal{A}^\dagger$. On physical grounds the eigenvalues of an observable or operator are expected to be real. The reality of the eigenvalues is guaranteed whenever the operator is hermitian, hence hermitian operators is preferred in quantum mechanics and quantum field theories. Proof: A is hermitian with eigenvalues a , $A|a'\rangle = a'|a'\rangle$. Since A is hermitian we also have $\langle a''|A = a''^* \langle a''|$. Looking at $\langle a''|A|a'\rangle = \langle a''|a'|a'\rangle = \langle a''|a''^*|a'\rangle \Rightarrow 0 = (a' - a''^*) \langle a''|a'\rangle$. Hence either $a''^* = a'$ (the reality condition) or $\langle a''|a'\rangle = 0$ (the orthogonality condition).

These matrix elements combine into the full production amplitude [14]:

$$\mathcal{M}_{t+u} = -e^2 (g_\sigma^{Zq\bar{q}})^2 \frac{A_{\lambda_1, \lambda_2}^\sigma}{4\beta^2 \sin^2 \vartheta^* + \gamma^{-4}}$$

$$\mathcal{M}_s = \frac{e^2 s^{3/2} \beta}{M_Z^3 2\sqrt{2}} B_{\lambda_1, \lambda_2}^\sigma$$

where $\beta = \sqrt{1 - \frac{4M_Z^2}{s}}$, $\gamma = \frac{1}{\sqrt{1-\beta^2}}$, ϑ^* is the center of mass scattering angle with respect to the quark beam axis and the coefficients $A_{\lambda_1, \lambda_2}^\sigma$, $B_{\lambda_1, \lambda_2}^\sigma$ are given in Table 3.2 on page 33.

Note the explicit s dependence in the s-channel matrix element. This will give rise to an increased effect of the TGC vertex with increasing energy. As the coefficient $B_{\lambda_1, \lambda_2}^\sigma$ is dependent on the scattering angle of the boson in the center-of-mass frame, we now have two possibilities of investigating the effects of the TGC vertex to the total production amplitude. In this section the angular dependency is shown, the energy dependence is shown in the Monte Carlo samples in Sec. 6.2.2.

Using the helicity amplitudes from Table 3.2 on page 33 the differential cross section can be found for each helicity configuration. For the Standard Model this is shown in Fig. 3.4. Notice here that the dominant helicity configurations for the Z-bosons are the $(+, -)$ and $(-, +)$ configurations, which do not contain the TGC vertex. The smaller contributions have been summed.

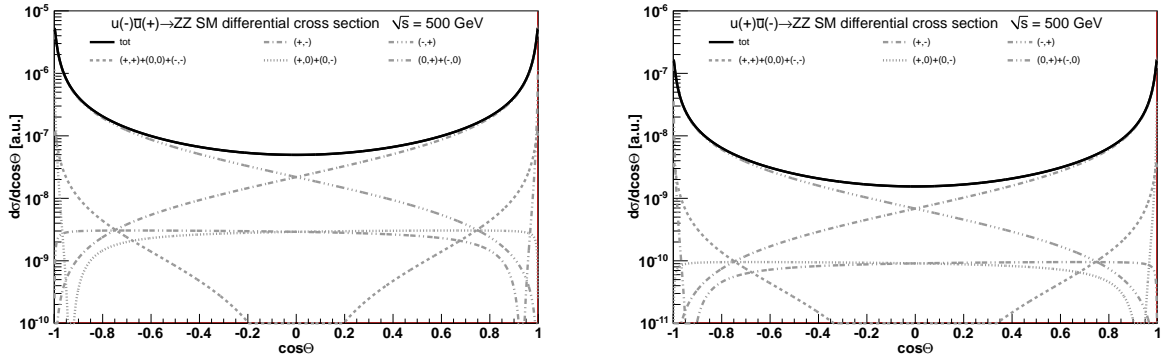


Figure 3.4: The differential cross section per scattering angle for the various Standard Model Z helicity configurations with a fixed $u\bar{u}$ helicity configuration of $u(+)\bar{u}(-)$ and $u(-)\bar{u}(+)$ [15].

The couplings are expected to change the individual helicity configuration distributions in the $Z(\pm)Z(0)$ and the $Z(0)Z(\pm)$ configurations through the $(1 - \cos \vartheta^*)$ dependency. Each helicity configuration will have a maximum at either -1 or 1, thus when performing the sum over the two, it will result in an overall increase in the entire range of the distribution. The results are shown in Fig. 3.5 on the next page.

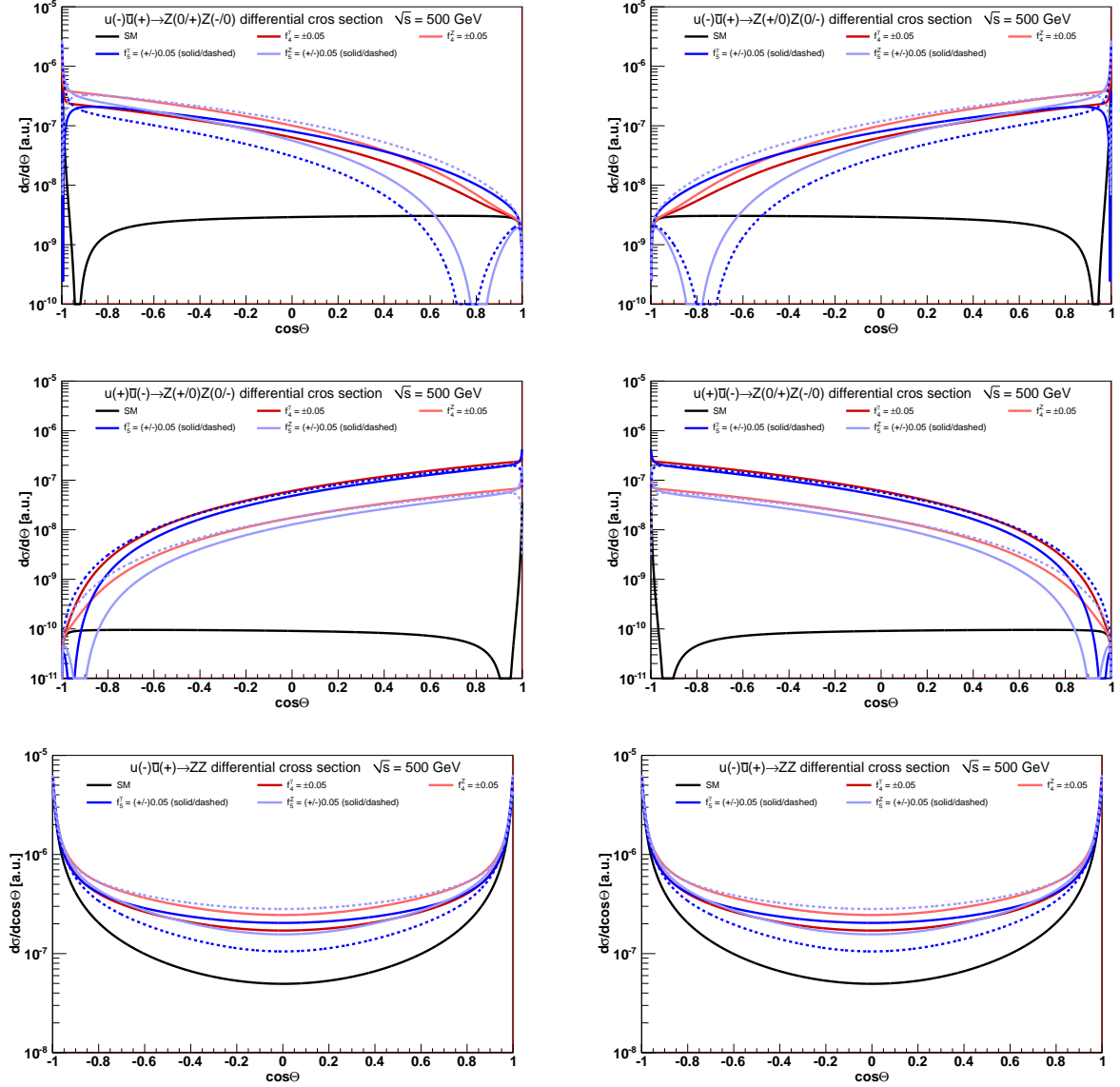


Figure 3.5: The differential cross section per scattering angle for the various TGC Z helicity configurations with a fixed $u\bar{u}$ helicity configuration of $u(+)\bar{u}(-)$ and $u(-)\bar{u}(+)$ and the sum of the Standard Model and TGC contributions summed [15].

$\lambda_1 \lambda_2$	$A_{\lambda_1, \lambda_2}^\sigma$	$B_{\lambda_1, \lambda_2}^\sigma$
+1 +1	$2 \sin \vartheta^* [2\sigma \cos \vartheta^* (\beta^2 - 1)]$	0
+1 -1	$2 \sin \vartheta^* [2\sigma \cos \vartheta^* (\beta^2 + 1) + 2(1 + \beta^2)]$	0
+1 0	$\frac{2\sqrt{2}}{\gamma} (1 - \sigma \cos \vartheta^*) [\sigma(1 + \beta^2) + 2 \cos \vartheta^*]$	$(1 + \sigma \cos \vartheta^*) [i(f_4^\gamma Q_f + f_4^Z g_\sigma^Z) - (f_5^\gamma Q_f + f_5^Z g_\sigma^Z) \beta]$
0 +1	$\frac{2\sqrt{2}}{\gamma} (1 - \sigma \cos \vartheta^*) [\sigma(1 + \beta^2) + 2 \cos \vartheta^*]$	$(1 + \sigma \cos \vartheta^*) [i(f_4^\gamma Q_f + f_4^Z g_\sigma^Z) - (f_5^\gamma Q_f + f_5^Z g_\sigma^Z) \beta]$
0 -1	$\frac{2\sqrt{2}}{\gamma} (1 + \sigma \cos \vartheta^*) [-\sigma(1 + \beta^2) + 2 \cos \vartheta^*]$	$(1 - \sigma \cos \vartheta^*) [i(f_4^\gamma Q_f + f_4^Z g_\sigma^Z) + (f_5^\gamma Q_f + f_5^Z g_\sigma^Z) \beta]$
0 0	$\frac{-4\sigma \sin(2\vartheta^*)}{\gamma^2}$	0
-1 +1	$2 \sin \vartheta^* [2\sigma \cos \vartheta^* (\beta^2 + 1) - 2(1 + \beta^2)]$	0
-1 -1	$2 \sin \vartheta^* [2\sigma \cos \vartheta^* (\beta^2 - 1)]$	0
-1 0	$\frac{2\sqrt{2}}{\gamma} (1 + \sigma \cos \vartheta^*) [-\sigma(1 + \beta^2) + 2 \cos \vartheta^*]$	$(1 - \sigma \cos \vartheta^*) [i(f_4^\gamma Q_f + f_4^Z g_\sigma^Z) + (f_5^\gamma Q_f + f_5^Z g_\sigma^Z) \beta]$
$\lambda_1 \lambda_2$	$l_{\lambda_1}^\rho$	$l_{\lambda_2}^{\bar{\rho}}$
+1 +1	$\frac{1}{\sqrt{2}} (1 - \rho \cos \theta) e^{i\phi}$	$\frac{1}{\sqrt{2}} (1 - \bar{\rho} \cos \bar{\theta}) e^{i\bar{\phi}}$
+1 -1	$\frac{1}{\sqrt{2}} (1 - \rho \cos \theta) e^{i\phi}$	$\frac{1}{\sqrt{2}} (1 + \bar{\rho} \cos \bar{\theta}) e^{-i\bar{\phi}}$
+1 0	$\frac{1}{\sqrt{2}} (1 - \rho \cos \theta) e^{i\phi}$	$-\bar{\rho} \sin \bar{\theta}$
0 +1	$-\rho \sin \theta$	$\frac{1}{\sqrt{2}} (1 - \bar{\rho} \cos \bar{\theta}) e^{i\bar{\phi}}$
0 -1	$-\rho \sin \theta$	$\frac{1}{\sqrt{2}} (1 + \bar{\rho} \cos \bar{\theta}) e^{-i\bar{\phi}}$
0 0	$-\rho \sin \theta$	$-\bar{\rho} \sin \bar{\theta}$
-1 +1	$\frac{1}{\sqrt{2}} (1 + \rho \cos \theta) e^{-i\phi}$	$\frac{1}{\sqrt{2}} (1 - \bar{\rho} \cos \bar{\theta}) e^{i\bar{\phi}}$
-1 -1	$\frac{1}{\sqrt{2}} (1 + \rho \cos \theta) e^{-i\phi}$	$\frac{1}{\sqrt{2}} (1 + \bar{\rho} \cos \bar{\theta}) e^{-i\bar{\phi}}$
-1 0	$\frac{1}{\sqrt{2}} (1 + \rho \cos \theta) e^{-i\phi}$	$-\bar{\rho} \sin \bar{\theta}$

Table 3.2: The coefficients $A_{\lambda_1, \lambda_2}^\sigma$, $B_{\lambda_1, \lambda_2}^\sigma$ from the ZZ production amplitude [14] and the coefficients $l_{\lambda_1}^\rho$, $l_{\lambda_2}^{\bar{\rho}}$ from the Z decay amplitude at different helicity combinations [13]. Notice the factor of i on the f_4^V couplings. This is responsible for the coupling being CP-violating and hence they will not interfere with the Standard Model. The couplings f_5 are CP-conserving and will thus interfere with the Standard Model.

Having studied the effects of the TGC vertex on the full production amplitude leaves only the decay amplitude to be calculated [13]:

$$\begin{aligned} \mathcal{M}(Z_\mu \rightarrow l_1^+ l_1^-) &= \bar{\psi}(p_2, \rho_2) [ZF\bar{F}] \varepsilon_\mu(q_1, \lambda_1) \psi(p_1, \rho_1) \\ \mathcal{M}(Z_\nu \rightarrow l_2^+ l_2^-) &= \bar{\psi}(p_4, \rho_4) [ZF\bar{F}] \varepsilon_\nu(q_2, \lambda_2) \psi(p_3, \rho_3) \end{aligned}$$

$$\begin{aligned} \mathcal{M}(Z_\mu \rightarrow l_1^+ l_1^-) &= e \sqrt{q_1^2} g_\rho^{Zl\bar{l}} l_\lambda^\rho \\ \mathcal{M}(Z_\nu \rightarrow l_2^+ l_2^-) &= -e \sqrt{q_1^2} g_{\bar{\rho}}^{Zl\bar{l}} l_\lambda^{\bar{\rho}} \end{aligned}$$

with $\rho \equiv \rho_1 = -\rho_2$, $\bar{\rho} \equiv \rho_3 = -\rho_4$ and the coefficients $l_{\lambda_1}^\rho$, $l_{\lambda_2}^{\bar{\rho}}$ given in Table 3.2. Adding all components gives the following process helicity amplitude:

$$\begin{aligned} \mathcal{M}(q\bar{q} \rightarrow l_1^+ l_1^- l_2^+ l_2^-) &= Z_{\alpha\mu}(q_1^2) Z_{\beta\nu}(q_2^2) \sum_{\lambda_1} \sum_{\lambda_2} \mathcal{M}(q\bar{q} \rightarrow Z_\alpha Z_\beta) \cdot \mathcal{M}(Z_\mu \rightarrow l_1^+ l_1^-) \cdot \mathcal{M}(Z_\nu \rightarrow l_2^+ l_2^-) \\ &= \frac{-e^4 \sqrt{q_1^2 q_2^2}}{(q_1^2 - M_Z^2 + iM_Z \Gamma_Z)(q_2^2 - M_Z^2 + iM_Z \Gamma_Z)} \\ &\quad \sum_{\lambda_1} \sum_{\lambda_2} \left[(g_\sigma^{Zq\bar{q}})^2 \frac{A_{\lambda_1, \lambda_2}^\sigma}{4\beta^2 \sin^2 \vartheta^* + \gamma^{-4}} + \frac{s^{3/2} \beta}{M_Z^3 2\sqrt{2}} B_{\lambda_1, \lambda_2}^\sigma \right] (g_\rho^{Zl\bar{l}} l_{\lambda_1}^\rho) (g_{\bar{\rho}}^{Zl\bar{l}} l_{\lambda_2}^{\bar{\rho}}) \end{aligned}$$

The differential cross section for an unpolarised $q\bar{q} \rightarrow ZZ \rightarrow 4l$ process is then found from the matrix element above:

$$d\sigma = \frac{1}{2s} \cdot \frac{1}{4} \sum_{\sigma, \rho, \bar{\rho}} |\mathcal{M}(q\bar{q} \rightarrow ZZ \rightarrow l_1^+ l_1^- l_2^+ l_2^-)|^2 d\Phi$$

$$d\sigma = \frac{\lambda}{64\pi^2 s} \cdot \frac{1}{4} \sum_{\sigma, \rho, \bar{\rho}} |\mathcal{M}(q\bar{q} \rightarrow ZZ \rightarrow l_1^+ l_1^- l_2^+ l_2^-)|^2 d\Omega$$

This differential cross section is denoted the *absolute weight* of each event. This weight is used in the reweighting technique (see Sec. 5.1 on page 50), allowing for extracting theoretical information from Monte Carlo samples or data on an event-by-event basis.

The observables most sensitive to the couplings, are observables that are s and ϑ^* dependent, since both of these terms are present in the s-channel matrix element. This makes the transverse momentum of each boson a very interesting variable, as well as the invariant mass of the bosons. In the Standard Model these variables peak around the Z -mass for p_T and around $2M_Z$ for M_{ZZ} and fall off at higher energies. The presence of the s-channel diagram would show itself at high p_T and M_{ZZ} and hence giving a rise in the tails of the distributions. A general increase of events in the scattering angle is expected as shown in Fig. ?? on page ??.

3.2 Operator expansion in the ZZ sector

Before continuing this chapter a discussion of the operators generating the vertices in the TGC lagrangian is needed. As explained when building the Yang-Mills lagrangian, the vertices are generated from operators built from the constituents of the theory. In the Yang-Mills lagrangian the operators were the covariant derivative and the field strength tensor. From these two operators all vertices in the model was generated, giving rise to self-interactions between the vector fields A_i as well as interactions between the vector fields and the matter field, the fermion doublet. From this example one would expect that the operators generating the TGC lagrangian also was built from these constituents, ie. the covariant derivate and the field strength tensors $W_{\mu\nu}^\pm$, $Z_{\mu\nu}$ and $F_{\mu\nu}$, with $F_{\mu\nu}$ being the field strength tensor for the photon field. This would result in interactions amongst the gauge bosons. But remember that we introduced the Higgs field in order to give the gauge bosons their mass. This also interacts in the usual covariant way, hence we could expect three-boson vertices arising from operators built from the covariant derivative and the Higgs field. Thus this field could also be included in the operator expansion.

The idea behind the operator expansion is that at a new physics scale there exist particles so heavy that they cannot be probed at any collider. The signatures of these particles will only be small anomalous effects at low energies, being described by the TGC lagrangian. As long as the energy at which the particles are collided is much smaller than this new physics scale, $\sqrt{s} \ll \Lambda$, the operators generating these low energy effects, are dominated by the ones lowest in order of dimension. Each of the operators in the expansion should be hermitian and be multiplied by a coupling constant. Operators of higher power n should also be suppressed by a factor of $\left(\frac{\sqrt{s}}{\Lambda}\right)^n$ [14].

Because the energy scale to which we probe these effects of the new physics is lower than the energy scale to which the new physics arise, one does not need to specify the particle content or the symmetries at the new physics scale. It is sufficient to describe these terms at

the low energies, since one will never probe the new physics scale. This results in a model-independent way of looking for new physics, since the content of the new physics theory is not specified.

At low energies the operators generating the TGC lagrangian can be realised in two ways: The linear realisation or the non-linear realisation [14]. In the former the Higgs is light, while in the latter the Higgs is absent or very heavy. Based on the knowledge present today, the linear realisation is used in this thesis. Thus one can construct operators from the field strength tensors, $W_{\mu\nu}^{\pm}$, $Z_{\mu\nu}$, $F_{\mu\nu}$, the Higgs field, Φ , and the covariant derivative, D_{μ} . Any operator built from these constituents will contain interactions amongst the fields. The process of finding operators is continued until all vertices present in the TGC lagrangian are obtained. In order to generate all couplings f_4^V, f_5^V , the lowest dimension of the operators generating the vertices is 8 [14]. Strictly speaking the operators built from the fields and their field strength tensors should only be used in the unitary gauge⁴. This restriction can be relaxed by making the transformation from the physical basis to the massless basis, such that the particle content of the low energy regime becomes the fields $W_{\mu\nu}^i$, $B_{\mu\nu}$ and Φ and the covariant derivative now is transformed to the same basis. Retaining only the lowest dimension operators reduces the number of operators to two [16]:

$$\begin{aligned}\mathcal{O} &= i\tilde{B}_{\mu\nu}(\partial_{\sigma}B^{\sigma\mu})(\Phi^{\dagger}D^{\nu}\Phi) \\ \mathcal{O} &= iB_{\mu\nu}(\partial_{\sigma}B^{\sigma\mu})(\Phi^{\dagger}D^{\nu}\Phi)\end{aligned}$$

where $\tilde{B}_{\mu\nu} = \frac{1}{2}\epsilon^{\mu\nu\alpha\beta}B_{\alpha\beta}$. These two are sufficient to obtain the vertices with the couplings f_4^V, f_5^V . The total number of operators and their couplings can be found in [16].

The neutral sector of the TGC lagrangian is further restricted by Bose statistics, since there is always at least two identical particles. This forbids ZZZ , $ZZ\gamma$ and $Z\gamma\gamma$ interaction vertices if all particles are on-shell⁵. Thus one must require that at least one of the particles is off-shell.

With the operators presented above one has constructed a gauge invariant lagrangian up the new physics scale, Λ . But since the couplings have a large mass dimension they could depart rapidly from the Standard Model predictions, reaching unreasonably high values. This can be cured by the introduction of form factors, which will suppress the couplings with a factor of $\left(1 + \frac{\sqrt{s}}{\Lambda}\right)^n$ and thus cure the unwanted high-energy behaviour [14].

$$f_i^V(s) = \frac{f_{i0}^V}{\left(1 + s/\Lambda^2\right)^n}$$

where an appropriate choice of n will constrain the high energy behaviour ($n = 3$ for $f_{4,5}^V$ [17]). These form factors are included in some event generators and are used when setting limits on the couplings. But they are in general not needed, since one works in an effective lagrangian scheme. The effective lagrangian was never written as a complete description of Nature, but

⁴The unitary gauge is a gauge where the physical fields W^{\pm}, Z, F are used as a basis and the Higgs field is in a basis, where the GoldStone bosons, bosons arising from the spontaneous symmetry breaking, of the physical fields are exactly zero.

⁵Bose statistics require that the vertex function is symmetric. This means it should be symmetric under change of particles, ie. under change of momenta. The vertex function is perfectly symmetric under the change $q_1 \rightarrow q_2$, where the term with f_4^V is unaffected and the term with f_5^V is changed as such: $\epsilon^{\mu\alpha\beta\rho}(q_1 - q_2)_{\rho} \rightarrow \epsilon^{\mu\beta\alpha\rho}(q_2 - q_1)_{\rho} = -\epsilon^{\mu\alpha\beta\rho}(q_2 - q_1)_{\rho} = \epsilon^{\mu\alpha\beta\rho}(q_1 - q_2)_{\rho}$. Interchanging eg. $P \rightarrow q_2$, the f_5^V term is not symmetric: $\epsilon^{\mu\alpha\beta\rho}(q_1 - q_2)_{\rho} \rightarrow \epsilon^{\beta\alpha\mu\rho}(q_1 - P)_{\rho} = -\epsilon^{\beta\mu\alpha\rho}(q_1 - P)_{\rho} = \epsilon^{\mu\beta\alpha\rho}(q_1 - P)_{\rho} = -\epsilon^{\mu\alpha\beta\rho}(q_1 - P)_{\rho} \neq \epsilon^{\mu\alpha\beta\rho}(q_1 - q_2)_{\rho}$. Hence the vertex function must vanish when all three bosons are on-shell, taken care of by the $s - m_V^2$ factor.

only as a description at a given energy scale and it is thus not valid to all probed energy scales. Hence one would expect improper high energy behavior of the effective lagrangian, especially when the probed energy scales become comparable with the new physics scale. By applying the lagrangian to energies near the new physics scale one violates the effective lagrangian approach where it is explicitly required that $s \ll \Lambda$. The additional s dependence introduced by the form factor could also translate as a higher dimensional operator creating a coupling of that specific form, also violating the effective lagrangian approach, where one explicitly demands to keep only the lowest dimensional operators.

It should be noted here that I have chosen not to work with form factors in this thesis.

3.3 Leading order helicity amplitudes for $q\bar{q} \rightarrow Z^*/\gamma^* Z^*/\gamma^* \rightarrow e^+e^-\mu^+\mu^-$

The lagrangian under consideration in Sec. 3.1 is only valid when the two outgoing Z 's are on-shell. This restricts the diagram selection and the TGC's to the subset described. Allowing for off-shell Z 's and photons increases the number of leading order diagrams from four to fifteen ⁶, while the four $ZZ\gamma^*$ couplings $f_i^Z, f_i^\gamma, i = 4, 5$ and the eight $Z\gamma\gamma^*$ couplings $h_i^Z, h_i^\gamma, i = 1 \dots 4$ expand to the a set of 43 couplings [16]. The new couplings are generated by an effective lagrangian which is split into the CP-conserving and the CP-violating parts [16]:

$$\mathcal{L} = e \left(\sum_i l_i \mathcal{O}_i + \sum_i \tilde{l}_i \tilde{\mathcal{O}}_i \right)$$

where l_i, \tilde{l}_i are the coupling constants. The 43 couplings are combinations of the l_i and \tilde{l}_i and the specific relations and operators can be found in [16]. From this set of new couplings one can generate relations between the new off-shell couplings and the old on-shell couplings by requiring that the off-shell vertex rule reduces to the on-shell vertex rule [16]:

$$\begin{aligned} \Gamma_{\mu\nu\alpha}^{Z^*Z^*Z^*} &\rightarrow \Gamma_{\mu\nu\alpha}^{Z^*ZZ} \\ \Gamma_{\mu\nu\alpha}^{\gamma^*Z^*Z^*} &\rightarrow \Gamma_{\mu\nu\alpha}^{\gamma^*ZZ} \\ \Gamma_{\mu\nu\alpha}^{\gamma^*\gamma^*Z^*} &\rightarrow \Gamma_{\mu\nu\alpha}^{\gamma^*\gamma^*Z} \end{aligned}$$

If one restricts the analysis to the lowest dimensional operators, the dimension eight operators, and require that the couplings preserve the $SU(2)_L \otimes U(1)_Y$ invariance, the remaining operators are the two given in Sec. 3.2 [16]. Setting two of the off-shell bosons on-shell reduce the set of off-shell couplings, and give relations amongst the on-shell couplings as follows [16]:

$$\begin{aligned} h_3^Z &= -\frac{\sin\theta_W}{\cos\theta_W} h_3^\gamma = -f_5^\gamma = \frac{\cos\theta_W}{\sin\theta_W} f_5^Z = M_Z^2 \frac{v^2}{4} f \\ h_1^Z &= -\frac{\sin\theta_W}{\cos\theta_W} h_1^\gamma = -f_4^\gamma = \frac{\cos\theta_W}{\sin\theta_W} f_4^Z = M_Z^2 \frac{v^2}{4} f \end{aligned}$$

with θ_W being the weak mixing angle and v the vacuum expectation value of the Higgs field. Hence when including off-shell bosons to the amplitude, setting one of the couplings

⁶Recall that the $\gamma\gamma\gamma$ vertex is not allowed in the TGC model.

f_4^V, f_5^V will result in an automatic contribution from the diagrams with h_3^V, h_1^V couplings. In general this means that one cannot distinguish between the case where two Z's decay into leptons or the case where one Z and one photon decay to two lepton pairs.

The off-shell contributions can be implemented to the helicity amplitude by including the off-shell vertex rule instead of using the on-shell vertex rule. Hence the general contribution to the Z pair production reads [16]:

$$\mathcal{M}(q\bar{q} \rightarrow l_1^+ l_1^- l_2^+ l_2^-) = -\frac{e}{M_Z^2} \sum_{ijk} \sum_{\lambda_1} \sum_{\lambda_2} \frac{\mathcal{V}_i^\mu(Z_\mu^{*\lambda_1}/\gamma_\mu^{*\lambda_1} \rightarrow l_1 \bar{l}_1)}{D_i} \frac{\mathcal{V}_j^\nu(Z_\nu^{*\lambda_2}/\gamma_\nu^{*\lambda_2} \rightarrow l_2 \bar{l}_2)}{D_j} \Gamma_{\mu\nu\alpha}^{ijk} \frac{\mathcal{V}_k^\alpha(q\bar{q} \rightarrow Z_\alpha^{*\lambda}/\gamma_\alpha^{*\lambda})}{D_k}$$

where ijk runs over Z^*, γ^* and the propagators are $D_i = q_i^2$ for a γ^* and $D_i = q_i^2 - M_Z^2 + iM_Z\Gamma_Z$ for a Z^* . The initial and final fermionic vertices are the usual fermionic vertices as written in Table 3.1 on page 29 and the Standard Model contribution to $q\bar{q} \rightarrow Z^*/\gamma^* Z^*/\gamma^*$ are present inside $\Gamma_{\mu\nu\alpha}^{ijk}$, ie. such that $\Gamma_{\mu\nu\alpha}^{ijk} \frac{\mathcal{V}_k^\alpha(q\bar{q} \rightarrow Z_\alpha^{*\lambda}/\gamma_\alpha^{*\lambda})}{D_k} \rightarrow \frac{\mathcal{V}_{ij}^{\mu\nu}(q\bar{q} \rightarrow Z_\mu^{*\lambda_1}/\gamma_\mu^{*\lambda_1} Z_\nu^{*\lambda_2}/\gamma_\nu^{*\lambda_2})}{D_i D_j}$ for the Standard Model contribution.

3.3.1 Single resonant diagrams

A final note on the leading order Z pair production process is the topic of single resonant diagrams. In the above sections only double resonant diagrams are considered, ie. where the Z bosons are created by the incoming quarks directly or through the virtual boson. But one must also include the case where one Z is produced by the incoming quarks, this then decays to a lepton pair, from which a Z is radiated, decaying into a lepton pair. The TGC vertex is

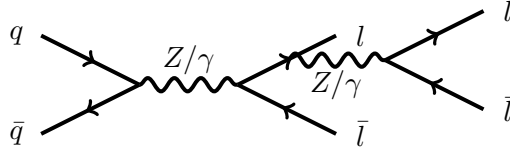


Figure 3.6: Z pair production in a single resonant diagram.

not present here, and this is thus just a simple Standard Model contribution. In the analysis presented in this thesis the single resonant diagrams are not allowed in the on-shell Z pair production process, while they are allowed in the off-shell Z pair production process. This is mainly because of the need for comparisons against other matrix element generators. In the on-shell case the single resonant diagrams are discarded, since the matrix element generators used for comparisons does not include these diagrams.

Even though the contribution of the single resonant diagram is a simple contributions, the crossing between these single resonant diagrams and the double resonant diagrams are non-trivial and hard to reduce. The benefit of studying the Z pair production at Monte Carlo level is, that one is able to generate samples without this contribution. But if the diagram is taken into account, ie. such as in a full $q\bar{q} \rightarrow e^+e^-\mu^+\mu^-$ sample or in data, care must be taken to remove these diagrams, if the TGC effects are to be studied. The effects of this diagram will be discussed in Sec. 7.2.

3.4 Virtual QCD corrections to $q\bar{q} \rightarrow Z(^*/\gamma^*)Z(^*/\gamma^*) \rightarrow e^+e^-\mu^+\mu^-$

We have now reached the point where we have retained all possible information of the leading order terms to the process of interest. Thus we enter the area of higher order corrections

to the leading order terms. This results in adding additional diagrams to the process and explaining what the effects of these diagrams are.

If one restricts the higher order terms to be of one order of magnitude higher in the couplings, one obtains the next-to-leading order corrections. These can be realised by either increasing the order of the electromagnetic coupling, e , or by increasing the order of the strong coupling, g_S . The former are known as electroweak corrections, while the latter are QCD corrections. Both are equally valid methods, but the QCD corrections are more probable to obtain, since the strength of the strong coupling is an order of magnitude higher than the strength of the electromagnetic coupling (~ 1.2 for the strong coupling compared to the ~ 0.3 of the electromagnetic coupling). Thus it is more likely to create loops with gluons in the process, than it is to create loops with photons and/or massive particles. As a result of this many studies are focused on the QCD corrections to processes. But in principle one should include both types of corrections, when discussing a full next-to-leading order correction. The electroweak corrections are beginning to find their way into various analyses, where a very interesting study is performed in [18] probing the electroweak corrections in vector-boson pair production at LHC energies. The results obtained in this paper have interesting (negative!) effects in the Z pair production channel even close to the production threshold of $M_{ZZ} \sim 200$ GeV. This effectively means that when including the electroweak corrections one would expect fewer Z pair events produced, because of this negative cross section.

A similar study was intended to be performed in this thesis, but for reasons evident later, the study could not be performed. A discussion on the subject can be found in Sec. 9. Hence only the QCD corrections are present in this analysis. These corrections appear when the incoming quarks emit gluons which are then either radiated as real emission or absorbed again, resulting in loop corrections. These loop correction will interfere with the leading order matrix element as described earlier. Thus one must investigate how the matrix element is affected by these next to leading order corrections. Thus one needs to know the Feynman rules describing QCD, given below:

$$\begin{array}{ll}
 \begin{array}{c} f \\ \swarrow \\ \bullet \\ \nwarrow \\ \bar{f} \end{array} \begin{array}{c} \text{---} \\ \text{---} \\ \text{---} \end{array} g & G_{q\bar{q}} = ig\gamma_\mu t^a \delta_{ij} \\
 g \begin{array}{c} \text{---} \\ \text{---} \\ \text{---} \\ \text{---} \\ \text{---} \end{array} & G_{ab} = \frac{-i(g^{\mu\nu} - (\xi-1)\frac{p^\mu p^\nu}{p^2 - \xi M_V^2 + i\varepsilon})}{p^2 - M_V^2 + i\varepsilon} \delta^{ab} \\
 g \begin{array}{c} \text{---} \\ \text{---} \\ \text{---} \\ \text{---} \\ \text{---} \end{array} & \varepsilon_\mu(p) \\
 g \begin{array}{c} \text{---} \\ \text{---} \\ \text{---} \\ \text{---} \\ \text{---} \end{array} & \varepsilon_\mu^*(p)
 \end{array}$$

Figure 3.7: The Feynman rules for QCD [3]. The t^a are the structure constants of QCD, just as $\frac{\sigma^i}{2}$ was for the Yang Mills lagrangian described in Sec. 2.1.2 and ϵ^{ijk} was for the electroweak lagrangian described in Sec. 2.2.4. The fermion lines can be seen in Sec. 3.2

Once the Feynman rules have been set, one must begin the process of imagining the possible diagrams. In the specific case study performed in this thesis, there are ten loop diagrams present for on-shell Z-boson pair production. These are given in the Fig. 3.8 on the next page:

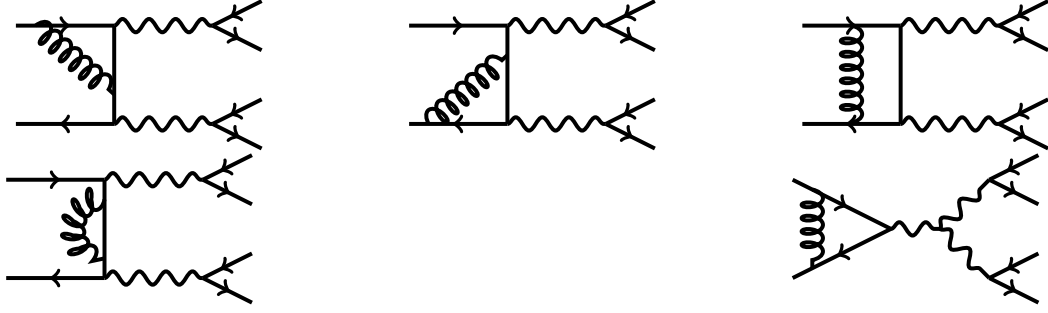


Figure 3.8: QCD next-to-leading order contributions to diboson production without jets. The u-channel diagrams can be found by an appropriate change of boson momenta in the t-channel diagrams, thus resulting in 10 unique diagrams.

One can further label the first two in the t- and u-channels as triangle diagrams, while the third diagram in the t- and u-channels is a box diagram. The last diagram correspond to a loop diagram. The s-channel diagram(s) is a triangle diagram. Present are also the next-to-leading order diagrams where an external quark emits a gluon and absorbs it again before the hard scattering process occurs, but in the dimensional regularisation scheme they equal zero [19]. Hence they are not included in this thesis.

The one-loop contribution can be obtained by constructing the matrix elements just as done in the leading order case. But one must be careful to include the proper couplings from the quark-antiquark-gluon vertex as well as integrate out the virtual momentum. The $[q\bar{q}g]$ vertex comes with a factor of $ig_S t^a$, with g_S being the strong coupling constant and t_a being the structure functions of QCD. The virtual diagrams are thus suppressed with a factor of g_S compared to the leading order amplitude. The interference terms between the leading order and virtual corrections will thus be suppressed with a factor of $g_S^2 \sim \alpha_S$ with respect to the leading order amplitude.

Allowing for off-shell bosons greatly increases the number of diagrams, since we now allow for four extra (sub)processes: $q\bar{q} \rightarrow Z^*Z^* \rightarrow e^+e^-\mu^+\mu^-$, $q\bar{q} \rightarrow \gamma^*Z^* \rightarrow e^+e^-\mu^+\mu^-$, $q\bar{q} \rightarrow Z^*\gamma^* \rightarrow e^+e^-\mu^+\mu^-$ and $q\bar{q} \rightarrow \gamma^*\gamma^* \rightarrow e^+e^-\mu^+\mu^-$. Thus naively one would expect 40 diagrams. But recall that the $\gamma\gamma\gamma$ vertex is not allowed in the TGC lagrangian, resulting in a final set of 39 next-to-leading order diagrams to the double resonant tree level process. Including the single resonant diagrams gives an additional sixteen loop diagrams, because each of the four subprocesses has four diagrams (emitting a boson from either the lepton or the anti-lepton = 2 diagrams, decaying to first electrons, then muons=1 diagram or the reverse=1 diagram), summed up in Fig. 3.9. The number of loop correction diagrams to the entire off-shell study totals to 55 diagrams, each of which contribute to the total next-to-leading order matrix element.

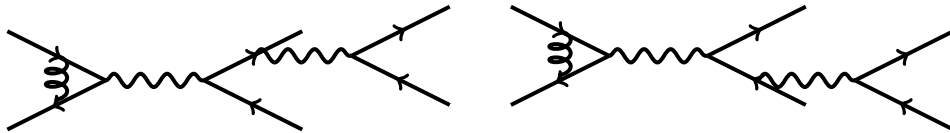


Figure 3.9: Virtual QCD corrections to single resonant Z pair production.

Each of the diagrams can separately diverge, and situations can arise where, after correct renormalisation, the finite term of the one-loop amplitude is negative. These amplitudes will then create negative differential cross sections, denoted as negative weights. If a large number of event weights become negative, one could imagine a situation where the next-to-leading order effects decreases the number of events compared to the number of events expected at leading order. This is exactly the case presented in [18]. Thus the naïve notion

of obtaining more events when turning on the next-to-leading order contributions might prove to be wrong.

3.5 Real emission corrections: $ZZ + j$ contributions

The real emission contributions to Z pair production all give rise to a five-particle final state, where the emitted particle is a coloured particle giving a jet in the detector.

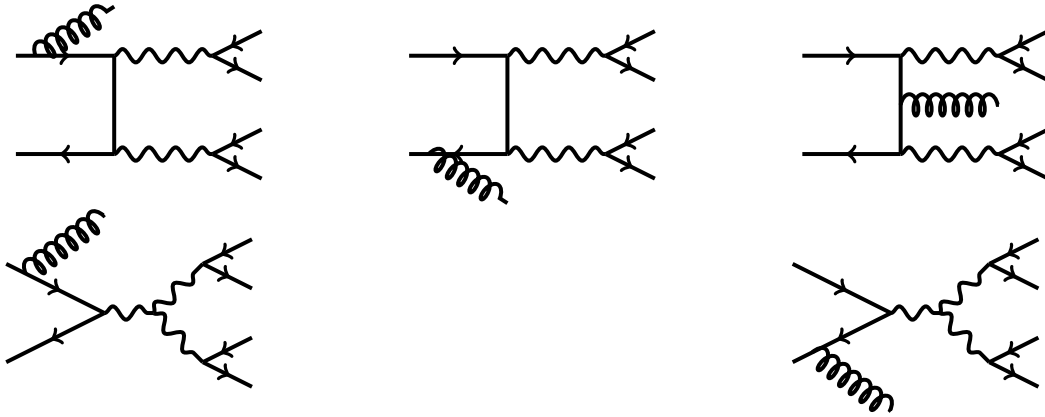


Figure 3.10: Real gluon emission contributions to $q\bar{q}$ diboson production. The u-channel diagrams can be found from the top three with an appropriate change of Z-boson momentum $q_1 \rightarrow q_2$.

Thus in the on-shell study one obtains 10 diagrams: Three t-channel, three u-channel and four s-channel diagrams. When studying the matrix element for such a process, one obtains two additional factors of i compared to the leading order diagrams: One factor of i coming from the $q\bar{q}g$ vertex and one coming from the additional internal quark propagator. This gives a sign difference compared to the leading order matrix element, and thus the real gluon emission is expected to contribute negatively to the leading order matrix element. These diagrams are also suppressed with a factor of g_S coming from the $[q\bar{q}g]$ vertex. One must also remember, that the real emission diagrams comes with an additional particle in the final state. Thus the phase-space is different, resulting in an integral over the three body phase space function when calculating the total cross section.

Including the off-shell contribution increases the number of subprocesses from one to four. Thus the end result is 38 ($10 \times 4 - 2(\gamma\gamma\gamma) = 38$) real emission diagrams. The single resonant process contributes with 32 diagrams (the four drawn in Fig. 3.11, multiplied with the four subprocesses and the two possibilities of lepton decays=32), thus resulting in a final set of 70 real gluon emission diagrams.

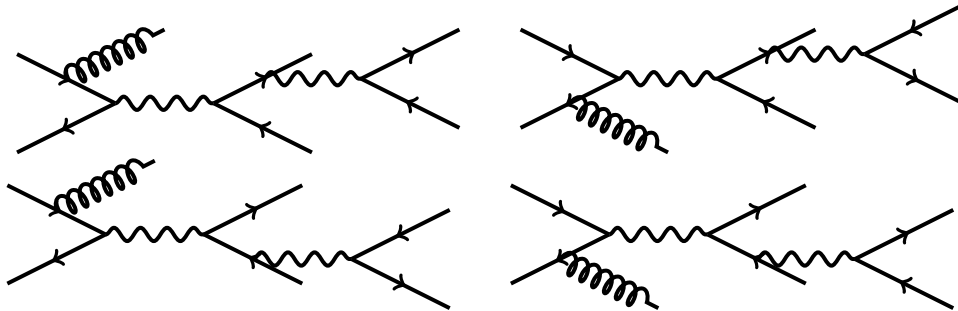


Figure 3.11: Real emission corrections to single resonant Z pair production.

Besides these diagrams, there are contributions from (anti)quark-gluon production. These

diagrams are different in initial state, and hence do not interfere with the leading order $q\bar{q}$ process. But they do contribute in the $ZZ + j$ processes because of the high gluon density at LHC, thus for a full simulation of the Z pair production process, these diagrams must be presented as well. They are included in the developed algorithm such that they will be weighted on equal grounds as the gluon emission diagrams.

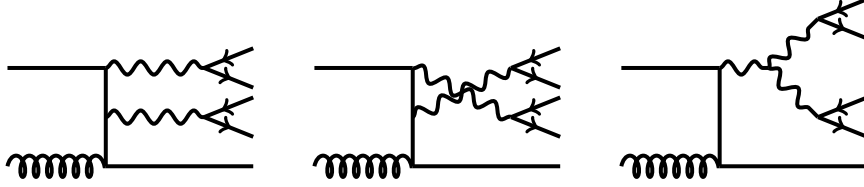


Figure 3.12: Real (anti)quark emission contributions to $q\bar{q}$ diboson production.

3.6 Gluon-gluon fusion

Whenever protons are collided at very high energies, eg. at the LHC, the most abundant parton is the gluon. Hence the most probable particle to enter in a hard scattering process is the gluon. But gluons do not couple to the other gauge bosons, since they do not carry colour. Thus one cannot create a pure gluon-induced diboson process at leading order. But at next-to leading order the process occurs: Two gluons can connect to either a quark box or a quark triangle. From these virtual quarks the bosons of interest can be produced.

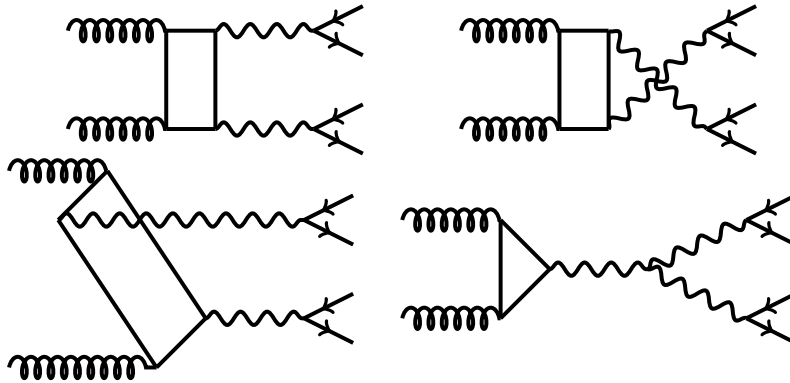


Figure 3.13: Gluon induced Z pair production. The upper two diagrams correspond to two gluons interfering through box quark exchange, whereas in the bottom left, the virtual quarks emits the Z -bosons before connecting with the gluon. The bottom right diagram is the triangle diagram and includes the TGC vertex.

The gluon-induced Z pair production does not interfere with the leading order $q\bar{q}$ matrix element, since this is a completely different process. The matrix element squared is then the one-loop matrix element squared, in practice an order higher in couplings, making it a next-to-next-to-leading order (NNLO) process. But because of the high probability of creating the gluons, the process will contribute to the total Z pair production amplitude significantly.

The most concerning issue with the gluon-induced process is that the loops now consist only of quarks. Each of the quarks are described by the Dirac propagator, carrying an instance of momentum in the numerator. Thus these diagrams will be harder to evaluate, which we shall see in the next section.

3.7 Ranking the loop diagrams

The method of calculating the virtual contributions in this thesis is based on a one-loop matrix element generator, GoSam [9]. As stated in Sec. 2.4.1 this program ranks the integrals based on the instances of momenta in the numerator of the integrals. The integral libraries used in the program are limited in the sense that they can only evaluate integrals, of which the rank of the integral does not exceed the rank of the loop [20]. Thus it is necessary to check if the integrals found in the above sections can be evaluated by the program.

In the virtual QCD case there are three types of integrals: Box, triangle and loop. Starting with the box diagrams, they are of integral rank three, because there are three virtual quarks in the loop and one gluon. The fermionic propagators with momentum p carry one instance of momentum in the numerator, ie. $D \sim \frac{\not{p}}{p^2 - m^2}$. Working in the Feynman gauge, the gluons do not carry any momentum in the numerator, making the propagator 'scalar'. This results in a total rank of three for the box diagrams. Since the diagram is a box, the loop size is four, and one can thus evaluate the box diagram in the Feynman gauge. The triangle diagram is of loop rank three and integral rank two in the Feynman gauge and can thus also be evaluated. The final diagrams present are the loop diagrams, which are of loop rank two, while the integral rank is one in the Feynman gauge. Hence all QCD corrections are possible to evaluate in the Feynman gauge.

The gluon induced process is only through quark box and triangle diagrams. This makes all diagrams have integral rank equal to their loop rank, ie. they have higher rank than the QCD correction integrals. The extra instances of momenta in the numerators creates more difficult integrals to evaluate, slowing the integral libraries significantly. The additional feature of allowing for all quark types in the loops creates six times as many diagrams, increasing the total number of diagrams to 60 all having the high integral ranking. This effectively slows the evaluation of the integrals down so much, that one helicity configuration takes more than a week to evaluate. Given the fact that the gluon induced process has 64 helicity configurations, the evaluation of the gluon induced process is beyond the timelimit of this thesis. This effectively means the gluon induced Z pair production has been discarded in the analysis.

Introducing the electroweak corrections should in principle be on equal footing as the gluon induced corrections, since they also will have integral rank equal to the loop rank. Assuming only fermionic loop corrections thus gives rise to ten fermion loop diagrams in the on-shell case. This is then multiplied with the six types of quarks and summed with the number of leptons available. This gives a factor of 10×6 diagrams if the boson creating the virtual pair is a Z, while it gives rise to a 10×3 diagrams if the photon creates the virtual pair, since photons do not couple to the neutrinos. Hence we end up with 150 diagrams. This is then multiplied with the factor of two coming from the direction of momentum in the loop, giving a total of 300 diagrams. And this is even without taking into consideration, that we could allow for four extra combinations, in the sense that the off-shell structure gives rise to four loop scenarios: a photon line splitting and combining with a photon line or a Z-line (2 cases) and a Z line splitting and combining with a photon or Z line (2 cases). This gives rise to ~ 1200 diagrams⁷ even without taking the single resonant diagrams into account.

This number unfortunately exceeds the limits of what GoSam is able to do. It is not a matter of the libraries not being able to calculate the integrals, it is just that the reduction of the integrals is highly time-consuming, and the higher the number of diagrams, the higher the number of integrals to reduce and evaluate. Being a general purpose one-loop matrix element generator means that GoSam package cannot include the neat tricks one can include when

⁷One must remember to subtract this number with the number of diagrams containing the forbidden $\gamma\gamma\gamma$ vertex.

hard-coding a processes by hand. The power of the general purpose generator diminishes greatly when higher dimensional integrals and large processes needs to be evaluated, hence results with high ranked integrals should preferably be done in the process specific generators. A functionality study of the program has been done, and a more detailed description on the timings is given in Sec. 5.6.

Monte Carlo event generators

Precision tests of the Standard Model as well as searches for new physics require a comparison of experimental findings and theoretical calculations. This is a highly non-trivial task because signals usually involve many-particle final states and these states are usually made from quarks and gluons, particles that only show up in bound states as hadrons. The transition from single particle to bound state is poorly understood in QCD, since this requires a transition from the perturbative to the non-perturbative regime. Thus our models of hadronization are usually not as well understood as the actual process producing these final state quarks and gluons. Also needed in the theoretical predictions is the specifications of the detector. These detector effects usually wash out signals and thus end up with smeared signals instead of sharp peaks, which would be the case if no detector effects and/or cuts were taken into account.

A way to overcome these theoretical difficulties is by using event generators. They are generally based on a divide-and-rule strategy, implying the events are divided into stages with respect to their energy scales [21]. This is done in the following way:

- Calculating the production amplitudes of heavy and/or highly energetic particles through the appropriate matrix elements. These are exact to some perturbative order and respect all quantum interferences etc.
- Radiating lighter particles which tend to be collinear with their emitters through the parton shower.
- Decaying the heavy unstable particles through appropriate matrix elements, and from these radiate additional lighter particles in the parton showers.
- Finally hadronizing the quarks and gluons into bound hadrons, decaying the bound hadrons that are not stable, thus identifying the bound states that eventually hit the detector.

Schematically this works well, but one should remember everything is handled numerically. This makes divergencies very difficult to handle. Multiple interactions of beam remnants and/or further beam particles, rescattering and pile-up effects contribute significantly to the final state, making these effects very important. But they are to some extent very limited in understanding. Thus the divide-and-rule idea is only an approximation to the real world, and must always be tweaked to data to make the predictions correct.

For this thesis most of the problems can be overcome, since it is concerned with the first step of the event division. The focus is to obtain the matrix elements of the Monte Carlo generator in question, thus for the most part the hadronization will not be taken into

account. Soft radiation will be taken into account only when generating events where real emission is included. Hence this presents a reliable method of calculating cross sections and final state distributions, since the first step is exact and respect all quantum symmetries etc.

4.1 Multichannel Monte Carlo generators

In the first step of the event generation the purpose of the Monte Carlo generator is simply to calculate the differential cross sections at a given phase space point. This relates to the issue of doing a numerical integration over a multi-dimensional function, $f(x)$, for which the analytical result is (usually) not known. The integral is, of course, supposed to be as close to the 'true' answer, in other words the Monte Carlo integration should provide a result with the smallest error possible.

A numerical approximation to an integral is in its most basic way found by finding the volume spanned by the function. If one splits the integration volume into smaller bins, and evaluate the integral in each bin, the result becomes closer to the analytical result. The method of Monte Carlo integration approximates the integral by choosing N integration points randomly from a uniform distribution and evaluates the function in these points. The integral is then approximated to the sum of the function values multiplied with the volume of the phase-space divided with the number of bins. The law of large numbers assures that this approximation will be equal to the integral in the limit of $N \rightarrow \infty$ [22].

The error on the integral gives an estimate of how well the integration was performed. It is thus of much importance to reduce this error, hence the multichannel Monte Carlo integration method was developed [23]. This method increases the number of distributions from which the N points are drawn. The integration points are drawn randomly from the sets of distributions with a given probability of drawing from each set. One then obtains a probability density for drawing the sample of integration points.

The integral in a bin is then merely the function value of the N integration points in the bin normalised to the probability of drawing said N integration points. This 'bin integral' is denoted the weight of the integration point, and summing over these weights, one obtains the total integral. A more formal introduction to the multichannel Monte Carlo integration method can be found in [23].

The integral is independent of the probabilities of drawing from each of the distributions. This means that during the integration the algorithm can change the probability of drawing from one of the distributions. This change will affect the error on the integral, since this depends on the probability, but not the integral itself. Hence if a distribution is seen to give large weights, the probability of drawing integral points from this distribution can be lowered. Likewise if a distribution contributes positively to the error, by giving small weights, the probability of drawing from this distribution can be increased. Hence the Monte Carlo integration optimises itself during the integration. This will in the end result in smaller integration errors [23].

This method of multichannel Monte Carlo integration is widely used in event generators. Both of the event generators used in this thesis are based on the multichannel method, but each has improved the method to their specific matrix element generators.

4.2 SHERPA

The SHERPA generator is a multi purpose event generator [21]. It contains two tree-level matrix element generators for SM and BSM reactions and can in itself handle all parts of the divide-and-rule strategy described in the above.

A process begins with SHERPA calculating the cross section of the process. After this has been evaluated at a given phase-space point the initial and final state radiation of the

partons in the process are simulated by $1 \rightarrow 2$ processes at different energy levels and with different probabilities [21]. The combination of the leading order matrix element and the parton shower is a tedious task. This is highly due to the additional emission of partons in a jet, restricted in a way such that the event does not change from an n -jet event to an $n+1$ -jet event. Several merging schemes exist, where SHERPA uses the Catani, Krauss, Kuhn, Webber (CKKW) merging scheme [24]. This scheme divides the jet-event into two regimes, one describing jet production using the matrix element generator, and one describing jet evolution, described by parton showering. In the jet production regime each new parton will be reweighted with respect to α_S suppressing the energy of further parton showering.

This merging scheme is important when real emission corrections are included to a process. A scale, defined by the user, steers the matrix element generator in SHERPA to chose if the process is a real emission process or not. This means that very collinear emitted particles cannot be distinguished from the outgoing particle, and the process will then be described as a pure $2 \rightarrow 4$ process, instead of evolving the emitted particle in a parton shower. Very soft outgoing particles are also described with the $2 \rightarrow 4$ matrix element, since they will not have enough momenta to be detected. Hence the user defined scale will in some sense dictate how large a fraction of real emission events are allowed in a process that includes the real emission corrections. The effects of the real emission will have impact on the analysis in this thesis, and will thus be described in more detail later.

4.2.1 The GoSam-SHERPA interface

In general SHERPA will handle all parts of the calculation except the next-to-leading order matrix elements. These matrix elements need to be generated with a next-to-leading order matrix element generator and interfaced to SHERPA using the Binoth Les Houches interface proposal [25]. This proposal dictates that the event generator initialises a process, by requesting the one-loop program to generate a set of processes specified by the event generator with the parameter setup used by the event generator. The one-loop programme then responds to this request by generating the needed processes with the proper parameter setup. When the one-loop matrix elements have been generated the event generator continues to the run-time phase. In this phase the one-loop matrix elements are called when needed. The one-loop program returns both the leading order and the next-to-leading order amplitudes, such that the ratio between the one-loop amplitude and the leading order amplitude can be extracted as a multiplication factor, from now on denoted the K-factor. This K factor is multiplied on the leading order matrix element generated internally in the event generator. The infrared divergencies returned by the one-loop program are checked against the divergencies obtained with in the event generator. A limit is usually set in the event generator, such that the infrared divergencies has to match within some precision. If the divergencies do not match, the event is discarded.

After SHERPA has put in a request for a set of processes, this must be passed to GoSam. GoSam then generates the next-to-leading order matrix elements and creates the confirmation file. If the generation of diagrams has succeeded. a message of OK is passed in the confirmation file. After a check of the contract file the matrix elements can thus be generated and the one-loop shared library can be passed to SHERPA, from where the one-loop amplitudes are called. Examples and further information on the Binoth Les Houches Accord (BLHA) interface can be found in [25, 26, 9].

A different interface between GoSam and SHERPA has also been created. This interface will generate and compile the GoSam code for the process specified in the SHERPA run card. But it only works with limitations, see [9], and only works within the Standard Model. This can be by-passed by cheating GoSam into thinking that the BSM model is in fact the Standard Model. This is done by renaming the BSM model files created by GoSam to names

recognised by the interface: `sm`, `sm.hh` and `sm.py`. The method should be valid, since a 'normal' run of GoSam can handle BSM physics. But of course the interface has only been validated for the Standard Model, and the method could in principle give wrong results. This cheating has been tried, but unfortunately the requirements for autotools and compilers did not allow compilation on available hardware.

As a final test of the interface between SHERPA and GoSam, a Standard Model sample for the process $pp \rightarrow e^+e^-\mu^+\mu^-$ was also tried. But this resulted infinite cross sections and thus SHERPA could not generate any events with virtual next-to-leading order corrections. Thus the method was not used in this thesis.

4.3 MADGRAPH

Along the same lines as SHERPA, MadGraph [27] is a tree-level matrix element generator. It has some advantages and some drawbacks compared to SHERPA, but is becoming more and more used, especially after the introduction of MadLoop [28], an algorithm designed for virtual corrections within the SM. BSM models can be implemented into MadGraph via the UFO format, an output of FeynRules [29] and LanHep [30]. This is the biggest advantage compared to SHERPA, since SHERPA does not allow for model import - it requires specific hardcoding in the various model. The MadLoop package is a good improvement, although many processes still need to be implemented. The drawback of MadGraph is that parton showering and hadronisation need to be passed to Pythia [31, 32], and although relatively simple to do, this makes the user effort bigger.

MadGraph can generate $2 \rightarrow n$ processes and decays, although the time requirement increases the higher number of external legs a process has. It creates helicity amplitudes using the generators HELAS [27] or ALOHA [33]. HELAS is a library containing helicity amplitudes for a number of different processes, ALOHA is called if the process is not found in HELAS. ALOHA automatically generates the helicity libraries, setting up routines for external and internal particles and amplitude calculations. It is done using the UFO output, wherein the vertex rules and particle definitions is set up. ALOHA then creates the analytical expression linked to the HELAS routine by contracting the vertex rule with a set of wavefunctions and expands this expression component by component. The result is an amplitude library, which can be called from eg. MadGraph.

4.3.1 The aMC@NLO interface

In order for MadGraph to use the MadLoop next-to-leading order generator the `aMC@NLO` interface has been developed [34]. This is fully implemented in MadGraph and will use MadLoop and the Standard Model as default. It can be called in MadGraph by generating a process with the command `[QCD]`, eg.

```
$generate p p > e+ e- mu+ mu- /h QED=6 [QCD]
```

This command will create the $pp \rightarrow e^+e^-\mu^+\mu^-$ at order e^6 and with QCD corrections and exclude all diagrams with Higgs bosons. MadLoop can in principle generate QCD corrections to BSM models, but relies on the UFO model imported in MadGraph being able to handle next-to-leading order processes. Hence the BSM model imported must be generated at next-to-leading order with FeynRules. But at the current time this version of FeynRules is still under development. It has only been validated for the Standard Model, and could in principle give wrong results with a BSM model. For this thesis a private beta version of FeynRules was obtained and used with the TGC model. But at the time of writing the next-to-leading order model has not been generated. It is not known whether it is the complexity of the TGC model or if it is a bug in the beta version of FeynRules that slows

down FeynRules, but the authors of FeynRules have been informed of this issue. Thus the MadLoop interface can only be used as a check of the Standard Model results.

The authors of MadGraph and aMC@NLO are currently implementing the GoSam generator as a one-loop matrix element generator in the aMC@NLO interface. The GoSam authors are currently validating the interface for the Standard Model before the interface becomes public. The author was asked to test the interface in collaboration with the developers and thus obtained the beta version of MadGraph. At this point of testing the Standard Model was the only model handled by the GoSam-MadGraph interface, but this could again be by-passed along the same lines as the GoSam-Sherpa interface. The interface is not ready for passing parameters between generators, hence a hard-coding in the GoSam model must be used when parameters should be changed. This is of course neither efficient nor completely safe, since the two generators could work with completely different parameter settings thus calculating the next-to-leading order contributions to the process at two very different energy scales etc. The testing of the interface is a work in progress and at the time of writing no results are ready.

4.4 MCFM

MCFM is a parton-level Monte Carlo program which gives next-to-leading order differential cross sections for a range of processes at hadron colliders. The program is developed by hard-coding the processes into MCFM, and is therefore not an automated ME generator. It includes all relevant diboson processes, but only includes a subset of the TGCs, where none of the ZZZ TGCs are present. The inclusion of the subset of TGCs (the five CP-conserving couplings for W -pair production, and the four for $Z\gamma$ production) requires the bosons to be produced on mass shell, and hence does not give a full result as done in the generic algorithm presented in this thesis. MCFM will be used as a test of the next-to-leading order results of GoSam, whereas a full description on the method of calculation in MCFM is not needed. In [35] the numerical results from MCFM are presented, but results on amplitude calculations are only presented for WW and WZ production.

The diagrams involved in the amplitude calculation in MCFM include both the gluon-gluon fusion diagrams as well as the double and single resonant diagrams. Gluon-fusion diagrams have been switched off, since these are not included in the thesis.

4.5 BHO and BR

For the specific purpose of generating matrix elements for diboson production, two fast and reliable generators exist, the Baur-Hahn-Ohnemus (BHO) [36] generator for all diboson processes and the Baur-Rainwater (BR) [37] for ZZ and $Z\gamma$ processes. They include a subset of the TGCs: All neutral and the CP conserving charged couplings. The outgoing gauge bosons are produced with their nominal mass values without width and can decay into both quarks and leptons. The BHO generator includes next-to-leading order corrections in the sense that it includes real emission diagrams but no virtual corrections. The BR generator does not include next-to-leading order corrections. Both generators are used as comparison to the GoSam generator at leading order and for the real emission.

4.6 GoSam

The most important generator in this thesis is strictly speaking not a Monte Carlo generator, but a one loop matrix element generator. GoSam [9] is a package for calculating amplitudes in a given phase space point, and thus cannot (automatically) do a full phase-space integration

as MCFM does. The matrix element from this generator is utilized in the reweighting algorithm developed in this thesis. The GoSam package contains two integral libraries, Golem95 [10] and Samurai [11], and is thus the wrapper program initialising the libraries and calling each when needed. GoSam is a generator capable of BSM model import from LanHep [30] and FeynRules [29], and provides a fast and reliable Standard Model library as well. The method of ranking integrals in GoSam has been described in Sec. 3.7 and a discussion of compiling issues is given in Sec. 5.4 before a benchmarking of the matrix element implemented in GoSam is performed in Sec. 6. Thus only a short introduction to the method used in GoSam is given here.

4.6.1 The GoSam conventions

GoSam uses a colour 'basis' when expressing the amplitudes. This is not a basis in the mathematical sense, since one can find linear relations between the 'eigenstates' $|c_i\rangle$. But it has advantages since in the colour basis the loop integrals reduce to a sum over a set of tensors (from where the tensor integrals get their name), making the matrix element easier to write down and evaluate numerically. A very short introduction to the terms and notations are given here, and unless otherwise stated, the findings of this section is based on [9].

Any one-loop diagram can be written in the following form

$$\mathcal{D} = \int \frac{d^n q}{i\pi^{n/2}} \frac{\mathcal{N}(q)}{\prod_{l=1}^N [(q+r_l)^2 - m_l^2 + i\varepsilon]}$$

where the numerator is a polynomial of consisting of powers of four momenta, $\mathcal{N}(q) = C_0 + C_1^{\mu_1} q_{\mu_1} + C_2^{\mu_1\mu_2} q_{\mu_1} q_{\mu_2} \dots$. The full one-loop amplitude is then a sum of the interference with the leading order terms

$$(\mathcal{M}^{(1)})^\dagger \mathcal{M}^{(0)} + h.c. = \sum_\alpha \int \frac{d^n q}{i\pi^{n/2}} \frac{N_\alpha(q)}{\prod_{i=1}^N [(q+r_i)^2 - m_i^2 + i\varepsilon]} + h.c.$$

with $N_\alpha = \sum_i N_i(q)^\dagger N_i(q)$. The fully renormalised matrix element at one-loop is

$$\begin{aligned} |M|_{one-loop}^2 &= \mathcal{A}_1^\dagger \mathcal{A}_0 + \mathcal{A}_0^\dagger \mathcal{A}_1 \\ &= |M|_{bare}^2 + |M|_{ct,\delta m_Q}^2 + |M|_{ct,\alpha_S}^2 + |M|_{wf,g}^2 + |M|_{wf,Q}^2 \\ &= \frac{\alpha_S(\mu)}{2\pi} \frac{(4\pi)^\varepsilon}{\Gamma(1-\varepsilon)} \cdot g_S^{2b} \left[c_0 + \frac{c_{-1}}{\varepsilon} + \frac{c_{-2}}{\varepsilon^2} + \mathcal{O}(\varepsilon) \right] \end{aligned}$$

with $|M|_{bare}^2$ being the unrenormalised matrix element, $|M|_{ct,\delta m_Q}^2$ being the mass counterterm, $|M|_{ct,\alpha_S}^2$ being the counterterm for α_S renormalisation, $|M|_{wf,g(q)}^2$ being the counterterm for gluon (quark) wavefunction renormalisation. The tree-level matrix element squared equal to

$$|M|_{tree}^2 = \mathcal{A}_0^\dagger \mathcal{A}_0 = g_S^{2b} \cdot a_0$$

where b is the power of the leading order coupling in the process.

The output amplitude from GoSam is an array $a[4] = a[0], a[1], a[2], a[3]$ translating to the amplitudes $(a_0, c_0, c_{-1}, c_{-2})$. The numbers correspond to the tree-level amplitude coefficient, a_0 , and the one-loop coefficients, c_0, c_{-1}, c_{-2} . If the process is loop induced GoSam returns $|M|_{one-loop}^2 = \mathcal{A}_1^\dagger \mathcal{A}_1$ where the factor of $\frac{\alpha_S(\mu)}{2\pi} \frac{(4\pi)^\varepsilon}{\Gamma(1-\varepsilon)}$ has been pulled out. These amplitudes are extracted from GoSam and used in the reweighting algorithm.

The generic reweighting algorithm

Event-by-event matrix element reweighting is a powerful experimental technique widely employed to maximize the amount of information that can be extracted from a collider data set. Given a set of theoretical hypotheses and a sample of events, the method assigns a weight to each hypothesis on an event-by-event basis. The computation of the weights is not trivial since it involves a difficult extraction of the theoretical information on the hard scattering amplitude based on the experimentally available information on the final state, such as momenta. In this chapter a generic algorithm is presented for evaluating the weights at next-to-leading order appearing in the matrix element method for any process of interest in the Standard Model and beyond. This is done using the next-to-leading order matrix element from GoSam [9], utilizing the leading order and next-to-leading order amplitudes and implementing these in the generic code developed. Given the initial and final state particles the algorithm assigns a weight to each event and can thus be used for both Monte Carlo reweighting and on experimental data, where the matrix element can be used to create a probability density function and thus create a discriminator among the different hypotheses.

5.1 The reweighting method

The reweighting method is a way to incorporate theoretical information in either a data sample or a Monte Carlo sample. In this thesis the TGC model has been implemented to the reweighting algorithm, and thus a short introduction will be given on how the TGC information is incorporated in a sample.

The method of reweighting includes the TGCs by rescaling the cross sections of the Standard Model to include the TGCs under consideration. Hence the t- and u-channel diagrams of the Standard Model will be scaled to include the s-channel contributions arising when including the TGCs. The developed algorithm is given the momenta from each event and will then calculate the differential cross section for the process including the s-channel diagrams. When including the s-channel diagrams in the process, the differential cross section will be affected through the matrix element. The TGCs enter linearly in the lagrangian, giving rise to a change in the differential cross section as follows:

$$d\sigma = d\sigma_{SM} + f_i^V \cdot F_1 + (f_i^V)^2 \cdot F_2$$

where $d\sigma_{SM}$ is the differential cross section of the Standard Model process, and f_i^V is the TGCs with $i = 4, 5$ and $V = Z, \gamma$. The F_i 's are the operators generating the couplings f_i^V and consist of both Standard Model and beyond operators. They are however completely determined by the kinematics of the event, hence being independent of the coupling value.

Considering more than one coupling at a time, the above expression becomes:

$$d\sigma = \sum_{i,j=0,4,5} f_i^V f_j^V \cdot F_{ij}$$

with the Standard Model contribution being given with $f_0^V = 1$ and $F_{00} = d\sigma_{SM}$. Normalising this differential cross section to the Standard Model result will result in the reproducing the effects of the TGCs through the weight:

$$\begin{aligned} w(TGC) &= \frac{\sum_{i,j=0,4,5} f_i^V f_j^V \cdot F_{ij}}{d\sigma_{SM}} \\ &= \frac{d\sigma(event)}{d\sigma_{SM}} \end{aligned}$$

The method can of course be 'reversed', ie. the Standard Model can be obtained from a sample generated with non-zero values of the TGCs. Here the inverse approach is used and one assigns a weight to each event, normalised to the differential cross section when the TGCs are included:

$$w(SM) = \frac{d\sigma(event)}{d\sigma_{TGC}}$$

With the reweighting method the next-to-leading order effects can be incorporated into a leading order sample, by calculating the weight of the event with the next-to-leading order matrix element and normalising to the leading order differential cross section:

$$w(NLO) = \frac{d\sigma(event)}{d\sigma_{LO}}$$

In this way one can mimic the effects of the full next-to-leading order calculation with all TGCs included.

5.2 Structure of the program

The algorithm is designed such that the user only needs to provide the tar balls with the appropriate source code for each process considered. Once a decision of the needed processes has been taken the user must create the tar balls in GoSam¹. The tar ball includes all information needed for compilation of source codes and calculation of the process amplitude. From here the automated setup takes over, where it generates all needed source code and creates shared object files. When the interface has been generated the user must take a decision on how to use the interface. Either the C++ binding in the program package can be compiled and used for further analysis, or the user can choose only to compile the Fortran90 interface and write his or her own code calling the subroutines available in the interface. A detailed description of the setup, compilation and usage of the provided C++ binding is given in Appendix D, while a detailed description of the interface is given in Appendix C.

The GoSam package can handle any $2 \rightarrow 6$ process in the Standard Model or beyond, provided the user implements the new physics model via LanHep or FeynRules. In the available test study program the TGC lagrangian for diboson production has been implemented in GoSam using LanHep, and a set of process tar balls has been created from this model. These process tar balls have been given to the interface and a specific diboson reweighting program has been developed. Leading order amplitude testing has been done versus the Standard Model implemented in GoSam and versus two other matrix element generators for diboson studies, the BHO and BR.

¹Please consult the GoSam Manual for further guidance [38]

5.3 Interface description and C++ binding description

The GoSam interface package comes with three shell scripts and one Makefile. The Makefile contains information on how and in what order the setup should be done. Two of the three shell scripts create Fortran90 files, one containing the process specific module creation and one containing the interface creation, from which the input is analysed. A decision is based on this analysis on which process to call to calculate the amplitude. The last shell script converts the process information from GoSam into a format readable by the interface script. Fig. 5.1 explains the structure of the interface.

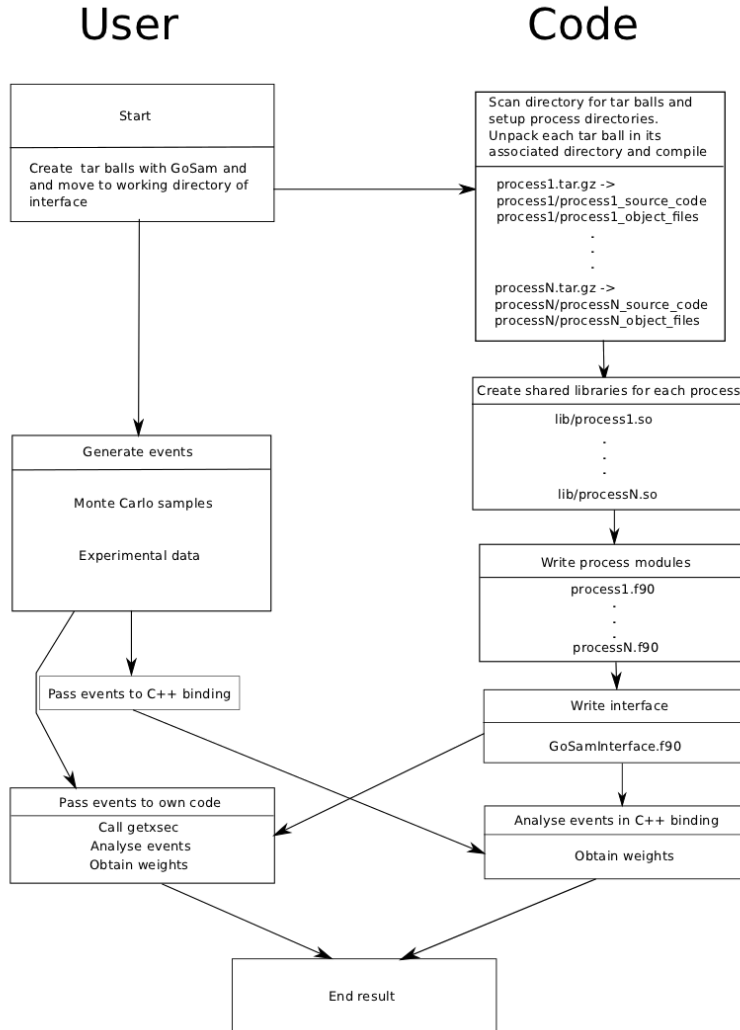


Figure 5.1: Flow chart of the generic algorithm.

The process modules contain a function to set the parameters needed by GoSam, `<name>_setParameter`, a function to call the squared amplitude from GoSam, `<name>_amplitude`, and a function to determine the process type, `<name>_processID`. The parameter function takes as input a character array passed by the interface. The amplitude function takes as input the momenta and PDG codes of the particles in the process as well as the renormalisation scale. The output of the amplitude function is two arrays, one containing the one-loop amplitude and the other the IR-divergencies. The final function takes as input the number of particles in the process and returns the particle code of the process.

The interface steering the module file contains two functions: `findparameter` and `getxsec`. The first translates a character string and a value into a character array readable by the process modules, and then calls each of the process modules to set the parameter to the given value. The last function is the main function of the interface. It takes as input the momenta and PDG codes of the particles and the renormalisation scale. Based on the PDG codes a decision is made on which of the process amplitudes to call. It then returns the one-loop amplitude and the IR-divergencies. If the PDG codes are not recognised by any of the process modules, the amplitude returned is zero. For more specific information see Appendix C.

A C++ binding has been developed such that the Fortran90 code can be called by including the binding in any C++ code. This class contains most of the relevant functions in which to collect the parts of the amplitude to a final result to be used in eg. a reweighting algorithm. Thus it contains an initialisation of the LHAPDF libraries [39], a calculation of the relevant couplings and form factors needed as well as a calculation of the phase-space function. A call to the main function, `GetXSec`, will return the differential cross section in the phase-space point passed to the function. This can then be used to obtain the full matrix element information for a given process in a given phase-space point. For further information of the C++ binding, see Appendix D.

5.4 Compiling issues

The GoSam package is very suited as a next-to-leading order matrix element generator in many ways. It has the advantage of being an automated generator and can include (almost) any beyond Standard Model process imaginable, being restricted only by the integral libraries, meaning that the rank of integrals must not exceed the rank of the diagrams under consideration. Effectively this means the libraries are ready for both virtual QCD and electroweak corrections. This is a major advantage compared to other loop generators that are hard-coded to specific processes, most of them hard-coded only to QCD corrections.

The drawback of GoSam is in fact the same thing. The automatically generated source code does not include the tricks of the trade in next-to-leading order amplitude calculations, meaning that it cannot exploit symmetries and other theoretical techniques that reduces the Feynman rules and integrals. Thus it is a very good generator for Standard Model processes, where the Feynman rules have been reduced by hard-coding them. When one wants to introduce a model beyond the Standard Model the Feynman rules become many lines long and hence the reduction by FORM [40] becomes slow. After FORM has done the required reduction the Java code Haggies [41] tries to translate the FORM result into an optimised Fortran90 code. Standard Model processes will be able to run on a machine with a usual amount of virtual memory (~ 16 Gb), but BSM models will not, since the FORM expressions are too large. This will cause Haggies to become very slow or even crash. Hence BSM physics can only be processed on machines with large amounts of virtual memory and only if Haggies does not try to group the expressions. Running the TGC model without grouping diagrams required up to 30 Gb of virtual memory. It is thus not able to run on a normal machine.

After a succesful source code generation the code needs to be compiled. A Standard Model process will be able to be compiled on a normal machine, since the source code is optimised and efficient. A BSM model will not. The fact that Haggies could not group the expressions means that the source code will have functions and expressions that are very big. These expressions will then be hard for the compiler to translate into machine language, and in some cases it will crash or use up all the virtual memory causing the machine to crash. None of these scenarios are desireable and the user of GoSam must take care in looking at ways to either reduce the Feynman rules or exploit symmetries etc. to reduce the number of

diagrams and/or helicities in the process. Before the TGC model was optimised the compiler used up to 120 Gb of virtual memory and actually at one point caused the machine to crash, ie. use all the 192 Gb of virtual memory accessible. After optimisation a limit was set on 75 Gb, and the compiler was able to compile the source code within this limit. But again, this is more virtual memory than accessible on a normal machine, hence the BSM physics can only be compiled on large machines.

When the compilation of the source code is done one has a set of libraries which can in principle be moved to any machine with the same compiler (or a newer version that is backwards compatible with the compiler that created the libraries) and thus does not need a large amount of memory to run. The speed of the calls to the amplitude calculation is slower than the hard-coded programs, but in principle only relies on the speed of the integral libraries called during the calculation. For further information, see 5.6.2 on page 57.

The GoSam collaboration is currently exploiting ways in which to handle big processes better. The author has been in contact with the collaboration during the writing of this thesis and they have proposed numerous things that helped in the optimisation of the code. They are currently testing the TGC model in the beta version of GoSam, and hopefully they will soon make the beta version public, such that new timing and compiling tests can be done. The GoSam package has as a complete set only been validated for the Standard Model, while the individual integral reduction libraries have been tested on some (hard-coded) BSM models. Thus the GoSam package is a very efficient tool for Standard Model processes, but requires some work before BSM physics processes can be recommended for 'normal' use.

5.5 The PDF weight

The PDF weight is a collective term for the factors lacking from the GoSam matrix element. If the matrix element has been calculated with all couplings set to one, these need to be restored for proper results. Implemented in the algorithm is an (optional) inclusions of the couplings by multiplying the returned amplitude from GoSam with the factors g^{2b} for the leading order amplitude and $\alpha_S(\mu_R)/(2\pi)g^{2b}$ for the next to leading order amplitude. The couplings g^{2b} vary depending on the process and the interface must take care of this fact. This is done by the user giving the name of the coupling, eg. weak, and the power b . As there is a possibility of doing both QCD and electroweak corrections, the algorithm needs to know the type of correction as well, such that the proper α can be added to the result.

After the coupling factors have been taken into account the calculation of the differential cross section follows as:

$$d\sigma = \sum_{a,b} dx_1 dx_2 f_a(x_a, \mu_F^2) f_b(x_b, \mu_F^2) \times d\sigma_{hard}$$

$$d\sigma_{hard} = \frac{1}{2s} \cdot |\mathcal{M}(hard)|^2 d\Phi$$

$$d\Phi = (2\pi)^4 \delta^4(k_1 + k_2 - \sum_{i=1}^N p_i) \prod_{i=1}^N \frac{d^3 p_i}{(2\pi)^3 2E_i}$$

On Monte Carlo level one knows which partons participated in the hard interaction. Hence the sum can be removed, and for each event one can calculate the density function for each participating parton, as well as the fraction of energy carried by this parton. The center of mass scattering energy is known from the incoming momenta, and we denote this the flux, F . Hence the missing term is the phase space factor, $d\Phi$ term. This can be evaluated by

decomposing the N -body phase space function into two- or three-body phase-space functions and the final result for the PDF weight in the given phase-space point is:

$$d\sigma = w(PDF) \times d\sigma_{hard}$$

$$w(PDF) = \frac{f_a(x_a, Q^2) f_b(x_b, Q^2) d\Phi K}{x_a x_b F}$$

where $F = 2s$, $x_i = p_{parton}/p_{proton}$ and $K = (\hbar c)^2$ for proper units.

Thus one can calculate the differential cross section, the absolute weight, for each event. The algorithm needs a minimal amount of information; Momenta of in- and outgoing particles, the renormalisation scale and specific constants of the theory, such as masses and couplings. Then the algorithm calculates the values of α_S, α , the next-to-leading order amplitude and the differential cross section at the given scale and uses this information to reweight the samples on an event-by-event basis.

5.6 Functionality study of the GoSam matrix elements

GoSam is for this performance study generated with the full TGC set, where the other generators BR and BHO lack both in number of diagrams and number of TGCs. BR is implemented only with the neutral couplings and is only leading order, but includes the off-shell γ^* diagrams. BHO is implemented with all neutral couplings but only the CP-conserving charged couplings. It is next-to-leading order, but only a subset of the real emission diagrams is included. Neither of the two generators include the single resonant diagrams. MCFM however, is next-to-leading order and includes both the gluon fusion diagrams and the single resonant diagrams. But MCFM does not include any of the neutral TGCs and only the CP-conserving charged TGCs. Hence the matrix elements generated with GoSam in this thesis are the first implemented with all TGCs at next-to-leading order.

A timing study is performed on GoSam in this section before the benchmarking of the matrix elements is performed in the next section. The algorithm relies on a set of tar-balls created by GoSam, hence the timing is noted for both generation of the tarballs, as well as unpacking and compilation of the process in the tarball. Finally the timing for the full generation of the reweighting algorithm is noted. The work has been done on a 48 core machine with 192 Gb of memory.

5.6.1 GoSam timing: Creation of the process tarballs

Each process is generated with its own input file in its own directory. From here the command `make dist` is executed, telling GoSam to create a tarball with the source code. The creation of the source code depends on the helicity configuration as well as the number of leading order diagrams and next-to-leading order diagrams in each helicity configuration. The compilation of the source code was done using `gfortran` version 4.1.2, with the optimisation option `-O2` and the options `-fPIC -g`.

A test was done on trying to improve the speed of generation and compilation, but not much succeeded. One successful optimisation of the diagram generation was to set the option `abbrev.level=diagram` (the setting used in the Table 5.3 on page 57). This is an option telling GoSam how to transform the diagrams into source code. The default is that it should do the calculation on helicity level, passing the sum of diagrams in a helicity configuration to Haggies and transform each helicity configuration into optimised Fortran90 code. This

Process QCD	No. of LO diagrams	No. of NLO diagrams	No. of helicity configurations	Creation time
$dd \rightarrow ZZ \rightarrow e^+e^-\mu^+\mu^-$	4	0	64	33m 58s
$uu \rightarrow ZZ \rightarrow e^+e^-\mu^+\mu^-$	4	0	64	34m 24s
$dd \rightarrow ZZ \rightarrow e^+e^-\mu^+\mu^-g$	10	0	128	546m 24s
$uu \rightarrow ZZ \rightarrow e^+e^-\mu^+\mu^-g$	10	0	128	545m 8s
$dg \rightarrow ZZ \rightarrow e^+e^-\mu^+\mu^-d$	18	0	128	554m 11s
$ud \rightarrow ZZ \rightarrow e^+e^-\mu^+\mu^-u$	18	0	128	555m 5s
$\bar{d}g \rightarrow ZZ \rightarrow e^+e^-\mu^+\mu^-\bar{d}$	18	0	128	488m 35s
$\bar{u}g \rightarrow ZZ \rightarrow e^+e^-\mu^+\mu^-\bar{u}$	18	0	128	490m 41s
$dd \rightarrow ZZ \rightarrow e^+e^-\mu^+\mu^-$	4	10	64	5670m 22s
$uu \rightarrow ZZ \rightarrow e^+e^-\mu^+\mu^-$	4	10	64	5674m 40s
$gg \rightarrow ZZ \rightarrow e^+e^-\mu^+\mu^-$	0	60	64	—
$dd \rightarrow Z^*/\gamma^*Z^*/\gamma^* \rightarrow e^+e^-\mu^+\mu^-$	31	0	64	100m 56s
$uu \rightarrow Z^*/\gamma^*Z^*/\gamma^* \rightarrow e^+e^-\mu^+\mu^-$	31	0	64	99m 38s
$dd \rightarrow Z^*/\gamma^*Z^*/\gamma^* \rightarrow e^+e^-\mu^+\mu^-g$	70	0	128	2250m 15s
$uu \rightarrow Z^*/\gamma^*Z^*/\gamma^* \rightarrow e^+e^-\mu^+\mu^-g$	70	0	128	2187m 43s
$dg \rightarrow Z^*/\gamma^*Z^*/\gamma^* \rightarrow e^+e^-\mu^+\mu^-d$	70	0	128	2235m 41s
$ug \rightarrow Z^*/\gamma^*Z^*/\gamma^* \rightarrow e^+e^-\mu^+\mu^-u$	70	0	128	2227m 11s
$\bar{d}g \rightarrow Z^*/\gamma^*Z^*/\gamma^* \rightarrow e^+e^-\mu^+\mu^-\bar{d}$	70	0	128	1806m 50s
$\bar{u}g \rightarrow Z^*/\gamma^*Z^*/\gamma^* \rightarrow e^+e^-\mu^+\mu^-\bar{u}$	70	0	128	1785m 29s
$dd \rightarrow Z^*/\gamma^*Z^*/\gamma^* \rightarrow e^+e^-\mu^+\mu^-$	31	55	64	13650m 45s
$uu \rightarrow Z^*/\gamma^*Z^*/\gamma^* \rightarrow e^+e^-\mu^+\mu^-$	31	55	64	13641m 40s
$gg \rightarrow Z^*/\gamma^*Z^*/\gamma^* \rightarrow e^+e^-\mu^+\mu^-$	0	114	64	—
Process EW	No. of LO diagrams	No. of NLO diagrams	No. of helicity configurations	Creation time
$uu \rightarrow Z^*/\gamma^*Z^*/\gamma^* \rightarrow e^+e^-\mu^+\mu^-$	31	1212	64	—
$dd \rightarrow Z^*/\gamma^*Z^*/\gamma^* \rightarrow e^+e^-\mu^+\mu^-$	31	1212	64	—

Table 5.1: The time it takes GoSam to create and compile the process tar balls. - indicates that at the writing of the thesis, the process was not done yet.

default setting caused Haggies to slow down or even crash when large amount of diagrams was created. But by passing one diagram at the time, the creation of the source code was successful for the runs that crashed with the default setting, and improved in speed in the runs that was slow with the default setting.

The improvement in compilation was not very successful. The optimisation option `-O0` was tried instead of the default `-O2`, but did not affect the speed. A test on lessening the number of helicities was also done, ie. creating a tarball for each helicity in each process, but neither the speed of the compilation nor the memory consumption was affected by this.

It should be noted that the hard-coded Standard Model provided in the GoSam package is both faster and less memory consuming for the compiler. The differences between the model files provided and the ones obtained when importing a model via FeynRules or LanHep primarily lies in the FORM model file. Here the Standard Model makes use of the hard-coded vertex rules obtained in the `vertices.hh` file provided by GoSam. The FORM model file `model.hh` hence only need to define the couplings missing in the `vertices.hh` file by defining a `VertexConstants` procedure. Any model import will not make use of the hard-coded vertex file. In stead it produces the vertex rules in the `model.hh` file. These are not optimised and thus will slow down Form and thus the entire evaluation of the diagrams in the process. Whenever possible it is **highly recommended** to use the hard-coded vertex rules and, if needed, hard-code the additional vertex rules needed in the `vertices.hh` file. It is not known to the author if a mixture between methods is possible and the author have thus settled on using the slow, but working, generated FORM model file.

5.6.2 Creation of the test program DiBosonStudy

The test program has been made in two versions, one for the on-shell case and one for the off-shell case. The compilation times for the two are:

Case	Compiling time
On-shell	2209m 9s
Off-shell	11975m8s

Table 5.2: Compiling time for the test programs used in the thesis.

The timing for reweighting a sample with 1000 events with the three generators are:

Generator	Processing time
On-shell BHO	0m 4s
On-shell BR	0m 4s
On-shell GoSam	14m 9s (13m 33s)
Off-shell GoSam	25m 53s (32m 30s)

Table 5.3: Compiling time for the test programs used in the thesis. A subset of 1000 events was reweighted from $f_4^\gamma = 0.25$ to $f_4^\gamma = 0$ (from LO to NLO) for each matrix element generator.

It is evident that in a run the automated generator is much slower than the hard-coded generators. But on the plus side, it does not take longer to include the next-to-leading order contributions, than it does without. It seems to be the integral libraries, Samurai and Golem95, that slows the algorithm down compared to the hard-coded (no virtual corrections) matrix element generators.

Benchmarking the GoSam matrix element

The algorithm presented is developed to reweight events on an event-by-event basis. This means that each event is passed to the algorithm with information on PDG codes and momenta for each particle involved in the process. Further information, such as couplings and renormalisation scale is also passed, either by specifying them directly or by letting the algorithm calculate the needed information. To test the algorithm it is crucial that the different variables have the exact same value, hence a C++ test program was developed for the specific purpose of reweighting diboson events. This program also includes two other matrix element generators, BHO and BR. If the variables needed in the matrix element calculation are set up properly, the squared matrix element for the three available generators in the test program should be equal.

Presented here is first a test on W-pair production at leading order, then a test on Z-pair production at leading order and finally a test on the ability to reweight events with the full PDF information included.

6.1 WW leading order comparisons

The process under consideration, $d\bar{d} \rightarrow W^+W^- \rightarrow e^+\nu_e e^-\bar{\nu}_e$, was used as a test of the TGC model implemented in GoSam. It was tested against the GoSam Standard Model, MadLoop and MCFM at leading order, where results from MCFM and MadLoop was taken from [28]. The input parameters are:

Parameter	Value	Parameter	Value
α_S	0.118	N_f	5
M_Z	91.1867	μ	M_Z
M_W	80.44	α^{-1}	132.6844139
$\sin\theta_W$	$1 - \frac{M_W^2}{M_Z^2}$	Γ_W	2.1054

with the following kinematical configuration:

$$\begin{aligned}
p_d &= (39.534683750772302, 0, 0, 39.534683750772302) \\
p_{\bar{d}} &= (546.24075297747743, 0, 0, -546.24075297747743) \\
p_{\nu_e} &= (188.27600670927578, 3.8276243346653374, -38.361733789650529, -184.28668257634874) \\
p_{e^+} &= (295.10612392593191, 49.617890129404948, 30.642119343108476, -289.28662236587513) \\
p_{e^-} &= (41.828055877825669, -7.1022701637404531, -30.841911801229820, -27.348135100677510) \\
p_{\bar{\nu}_e} &= (60.565250215216373, -46.343244300329829, 38.561526247771873, -5.7846291838037445)
\end{aligned}$$

The test results in the following¹:

$dd \rightarrow W^+W^- \rightarrow e^+\nu_e e^-\bar{\nu}_e$	GoSam w/ TGC	GoSam Standard Model
a_0	$1.108063317575431 \cdot 10^{-4}$	$1.109591571689323 \cdot 10^{-4}$
$dd \rightarrow W^+W^- \rightarrow e^+\nu_e e^-\bar{\nu}_e$	MadLoop	MCFM
a_0	$1.11000204402873114 \cdot 10^{-4}$	$1.11000204410578607 \cdot 10^{-4}$

Slight discrepancies between the two GoSam models and MCFM and MadLoop are seen. The results obtained with GoSam are a bit smaller, but this is very likely due to the difference in the mixing matrix. The GoSam Standard Model uses the full Cabibbo–Kobayashi–Maskawa mixing matrix in Wolfenstein parameters expanded to $\mathcal{O}(\lambda^6)$ [9]

$$V_{ij} = \begin{pmatrix} 1 - \lambda^2/2.0 \cdot (1 + \lambda^2/4.0) & \lambda & A \cdot \lambda^3 \cdot (\rho - i\eta) \\ -\lambda \cdot (1 + A^2 \cdot \lambda^4 \cdot (\rho + i\eta - 0.5)) & 1 - \lambda^2/2.0 - (4.0 \cdot A^2 + 1) \cdot \lambda^4/8.0 & A \cdot \lambda^2 \\ A \cdot \lambda^3 \cdot (1 - \rho - i\eta) & -A \cdot \lambda^2 \cdot (1 + \lambda^2 \cdot (\rho + i\eta - 0.5)) & 1.0 - A^2 \cdot \lambda^4/2.0 \end{pmatrix}$$

with

$$\begin{aligned}
\lambda &= \sin\theta_{12} \\
A\lambda^2 &= \sin\theta_{23} \\
A\lambda^3(\rho - i\eta) &= \sin\theta_{13}e^{-i\delta}
\end{aligned}$$

while the TGC model implemented in GoSam uses the standard parametrization:

$$V_{ij} = \begin{pmatrix} c\theta_{12}c\theta_{13} & s\theta_{12}c\theta_{13} & s\theta_{13}e^{-i\delta_{13}} \\ -s\theta_{12}c\theta_{23} - c\theta_{12}s\theta_{23}s\theta_{13}e^{i\delta_{13}} & c\theta_{12}c\theta_{23} - s\theta_{12}s\theta_{23}s\theta_{13}e^{i\delta_{13}} & s\theta_{23}c\theta_{13} \\ s\theta_{12}s\theta_{23} - c\theta_{12}c\theta_{23}s\theta_{13}e^{i\delta_{13}} & -c\theta_{12}s\theta_{23} - s\theta_{12}c\theta_{23}s\theta_{13}e^{i\delta_{13}} & c\theta_{23}c\theta_{13} \end{pmatrix}$$

with $c = \cos$ and $s = \sin$. The results from [28] use $CKM_j^i = \delta_j^i$, hence removing the extra diagrams from the two GoSam models, would improve the comparison results. Changing the CKM matrix in the GoSam models one obtains:

$dd \rightarrow W^+W^- \rightarrow e^+\nu_e e^-\bar{\nu}_e$	GoSam Standard Model	GoSam TGC
a_0	$1.110005747993170 \cdot 10^{-4}$	$1.110261540264524 \cdot 10^{-4}$

Now the discrepancy between the implemented Standard Model and MCFM, MadLoop arise at the sixth decimal, giving a difference between generators of $\sim 10^{-4}\%$. The TGC model gives a result around $\sim 0.02\%$ too high. This is more than reasonable, and thus the initial difference was due to the diagonal CKM-matrix.

¹The author is aware of the high amount of significant decimals in the result. But when comparing to papers from theoreticians, the number of significant digits seem to be a competition. The higher number and precision, the better. But of course this result will never be measured. First of all there are all the effects from the PDFs and the lack of that precision in many of the 'fundamental' constants. And secondly any non-theoretician will always round up and only use two, maybe three significant digits.

6.2 ZZ leading order comparisons

The Z-pair production matrix element has been checked against the two generators BHO and BR. For direct comparisons between the three generators, the off-shell photon diagrams in BR has been switched off. Neither BHO nor BR include the single resonant diagrams, hence these have been switched off in GoSam and SHERPA.

A set of SHERPA samples has been generated for the benchmarking. The switch `Decay0S` (decay on-shell) has been used for the Z decays into leptons, since BHO does not include the off-shell diagrams. In all samples the Higgs production diagrams have been switched off, since neither of the generators include these diagram. Showering effects have been switched on in the generation of the jet samples. For all samples the PDF set CTEQ6.6 has been used.

SHERPA uses the matrix element from [13], hence only the TGC samples with the f_4^V couplings should in principle be used in the reweighting tests, since this vertex is not changed in the version from [14] used in this thesis. The f_5^V couplings from [14] has a sign difference compared to the version used in [13], thus it could be possible that these samples would show discrepancies when reweighting a coupling down to the Standard Model value. Instead the samples have been used as a comparison to a Standard Model sample reweighted to a coupling value with the vertex rule used in this thesis. This test will also tell if the change in sign actually does matter.

Process	Events	Generator	Beam energy	Model	σ (pb)
1 $pp \rightarrow ZZ \rightarrow e^+e^-\mu^+\mu^-$	10^6	Amegic++	7 TeV	SM	0.0095
2 $pp \rightarrow ZZ \rightarrow e^+e^-\mu^+\mu^-$	10^6	Amegic++	7 TeV	SM+AGC $f_4^\gamma = 0.25$	0.222
3 $pp \rightarrow ZZ \rightarrow e^+e^-\mu^+\mu^-$	10^6	Amegic++	7 TeV	SM+AGC $f_4^Z = 0.25$	0.288
4 $pp \rightarrow ZZ \rightarrow e^+e^-\mu^+\mu^-$	10^6	Amegic++	7 TeV	SM+AGC $f_5^\gamma = 0.25$	0.215
5 $pp \rightarrow ZZ \rightarrow e^+e^-\mu^+\mu^-$	10^6	Amegic++	7 TeV	SM+AGC $f_5^Z = 0.25$	0.279

Table 6.1: The SHERPA input

Particle	p_T (GeV)
e^+	$10 - E_{cm}$
e^-	$10 - E_{cm}$
μ^+	$10 - E_{cm}$
μ^-	$10 - E_{cm}$
Particles m_{ab} (GeV)	
e^+e^-	$12 - E_{cm}$
$\mu^+\mu^-$	$12 - E_{cm}$
$\tau^+\tau^-$	$12 - E_{cm}$

Table 6.2: The SHERPA cuts

6.2.1 Validation of the TGC model implemented in GoSam

The following shows the raw matrix element squared. The PDF weight (for proper cross sections) has been switched off in order to directly compare the matrix elements, and the strong and weak couplings have been set equal to one, since these couplings are pulled out of the results from the GoSam generator. A subset of 1000 events from the SHERPA samples

(1) and (2) have been processed for these tests. Figs. 6.1 to 6.3 on the following page show the ratio between the weights obtained with the two generators under consideration.

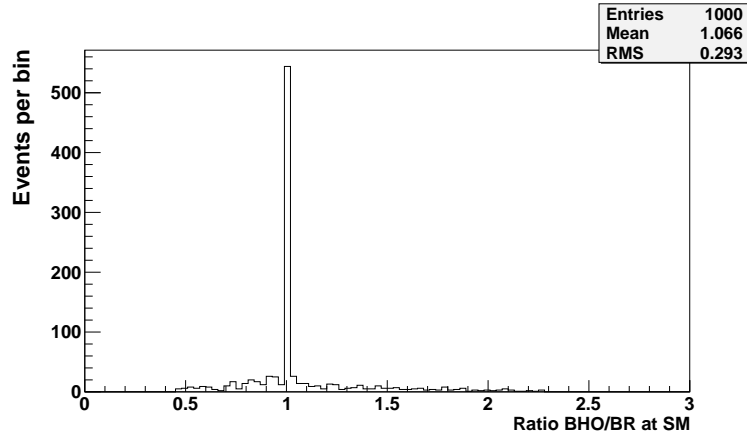


Figure 6.1: Matrix element comparison between BR and BHO generators in a $pp \rightarrow ZZ \rightarrow e^+e^-\mu^+\mu^-$ sample.

The first comparison is between the two generators BR and BHO at Standard Model values. Originally the two generators used different propagators, BHO using a fixed-width and BR using a finite-width propagator. The propagator in the BR code was corrected to the fixed-width propagator in order to be consistent with BHO. The results of the matrix element ratios is shown in Fig. 6.1. The two generators agree very well, showing a sharp peak at one, with some fluctuations probably due to numerical instabilities. Testing against the GoSam generator there is a clear correspondance between the GoSam and BHO, while the same fluctuations are seen between GoSam and BR.

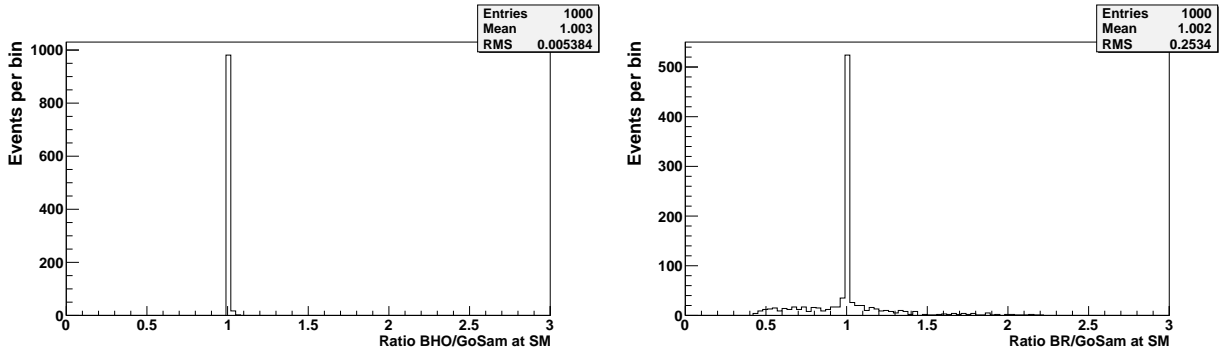


Figure 6.2: Matrix element comparison between GoSam and BHO generators (left) and GoSam and BR generators (right) in a $pp \rightarrow ZZ \rightarrow e^+e^-\mu^+\mu^-$ sample.

Hence the matrix element obtained with the new TGC model implemented in GoSam is valid with Standard Model coupling values. Testing for the beyond Standard Model matrix elements is performed by switching on the coupling values of $f_i^V = \pm 0.25, i = 4, 5$ in turn. The sample from which the weights are obtained is a Standard Model sample, hence no issues concerning sign factors are present in this test. Here the test of $f_4^\gamma = 0.25$ is shown, the remaining figures can be found in Appendix A.

With couplings turned on, the TGC matrix element from GoSam is again comparable to the generators BHO and BR. Thus the matrix element implemented in GoSam is valid at both Standard model and beyond coupling values. The remaining task to be performed is

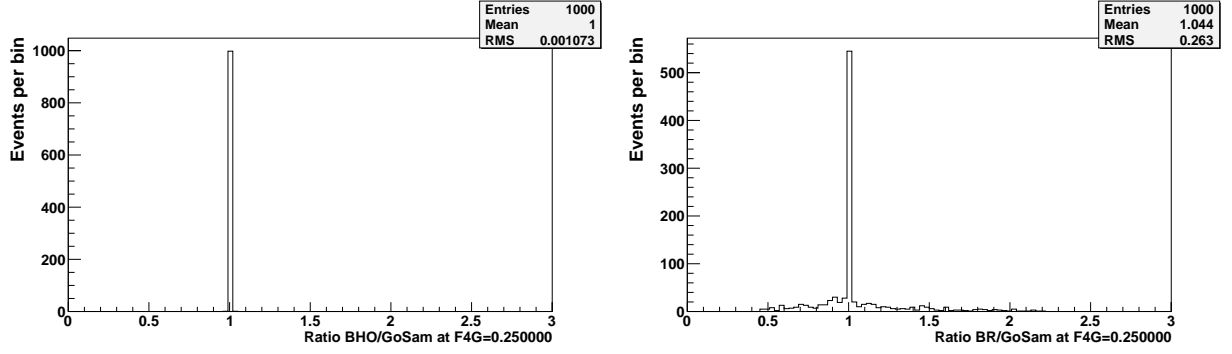


Figure 6.3: Matrix element comparison between GoSam and BR generators in a $pp \rightarrow ZZ \rightarrow e^+e^-\mu^+\mu^-$ sample including the coupling $f_4^\gamma = 0.25$ diagram in the matrix element.

to benchmark the reweighting algorithm developed. This is done in the next section, where a BSM sample is reweighted to the Standard Model values for the couplings f_4^V , while the reverse is performed on the couplings f_5^V , in case the sign difference in the matrix element matters.

6.2.2 Reweighting tests

The plots show the p_T distribution of the bosons on the x-axis and the number of events on the y-axis. Below is given the ratio between the Standard Model and the reweighted sample, ie. $ratio = \frac{SM}{reweighted}$. This makes sure that we do not obtain any zero-bin problems, ie. if no Standard Model events are present, the ratio is zero. The errors on the ratio are propagated in each bin as²

$$f = \frac{x}{y}$$

$$\sigma_f = f \sqrt{\left(\frac{\sigma_x}{x}\right)^2 + \left(\frac{\sigma_y}{y}\right)^2}$$

with x denoting the value in the bin of the Standard Model sample and y denoting the value in the bin of the TGC sample. Shown in the lower plots are the χ^2 of a fit to a straight line. The χ^2 is a measure of the goodness of the fit in the sense that it extracts the difference between observed and fitted values in a given bin taking the error in the bin into account. More formally it can be written [22],

$$\chi^2 = \sum_i^n \frac{(O - E)^2}{E}$$

with n being the number of bins, O being the observed value E the expected, or the value obtained when evaluating the fit function in the point. The reduced χ^2 , ie. the χ^2 divided by the number of degrees of freedom, gives a more straightforward goodness of fit measure. If the fit is good, the reduced χ^2 should be of the order of 1.

From Fig. 6.4 on the facing page it is clear that the reweighting method works very well. The TGC sample has been reweighted down to the Standard Model distribution and the ratio is located around one, with expected fluctuations in the bins with low statistics.

²This method has been used for error propagation in all plots shown from this point forward.

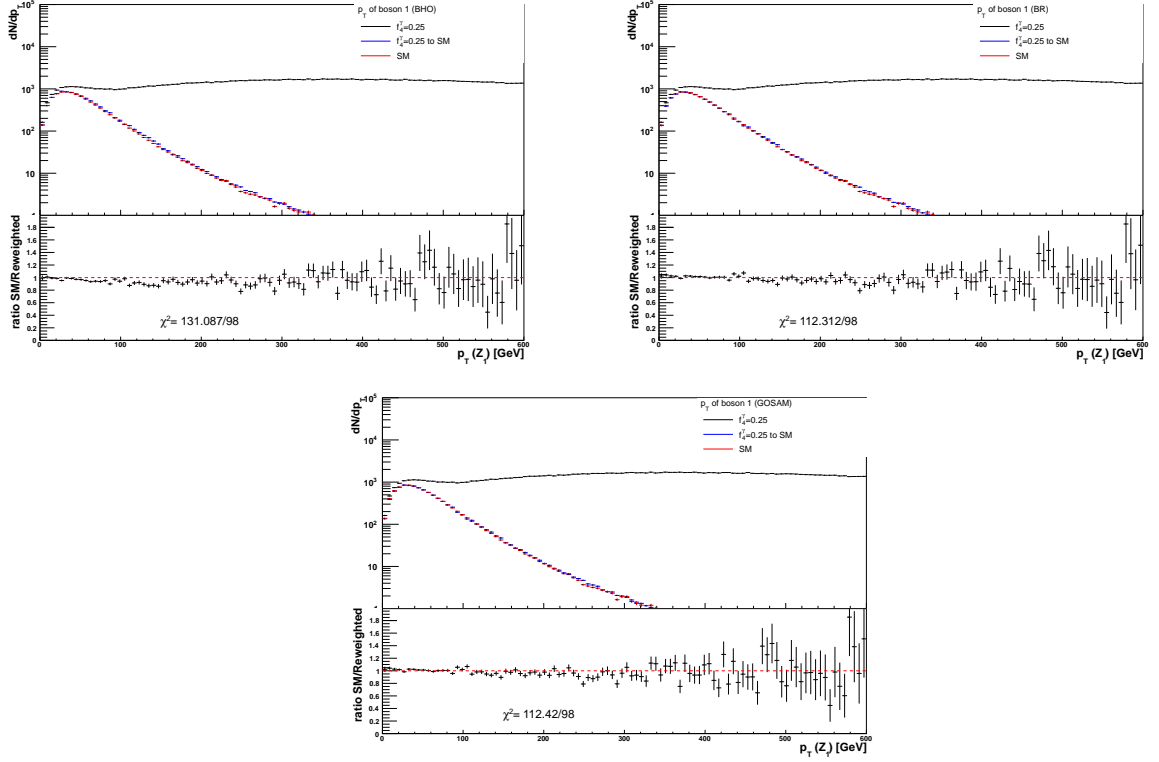


Figure 6.4: A BSM sample generated with SHERPA with the anomalous coupling $f_4^\gamma = 0.25$ is reweighted down to the Standard Model value of $f_4^\gamma = 0$ with the three generators BHO (upper left), BR (upper right) and GoSam (bottom) and compared to the Standard Model sample. The dashed red line indicates a ratio of one.

As seen in Fig. 6.4 the generators BR and GoSam give rise to a reduced $\chi^2 \sim 1$ whereas BHO has a slightly higher reduced χ^2 . But the difference is so small, that one cannot distinguish between generators based on this. Shown in Fig. 6.5 on the following page is the distributions of the discussed scattering angle. It was shown in Sec. 3 that the $\cos\theta$ dependence in the couplings should give rise to an increased number of events. In Fig. 6.5 on the next page the number of events per scattering angle is shown. It is thus evident that a sample generated with an anomalous coupling shows an increased number of events with respect to the Standard Model sample, thus behaving as seen Fig. ?? on page ?. The reweighting technique is able to reweight the TGC distribution down to the Standard Model, giving reduced χ^2 of the order of one for all generators.

Testing the matrix element of the f_5^Z couplings is performed by reweighting the Standard Model sample up to a value of $f_5^Z = -0.25$ and comparing this to the sample generated by SHERPA. It is possible that the sign factor in the matrix element could affect the reweighting method, hence this reversed method is used. The problem with the reverse method is that the Standard Model sample will have a small number of events in the high p_T tail where the effects of the TGCs are best seen. This will affect the errors on the reweighted sample, hence the fit of the ratio to one will in turn become higher. Thus the reversed method is not preferred and is only used, since there could be disambiguities because of the sign difference in the matrix elements.

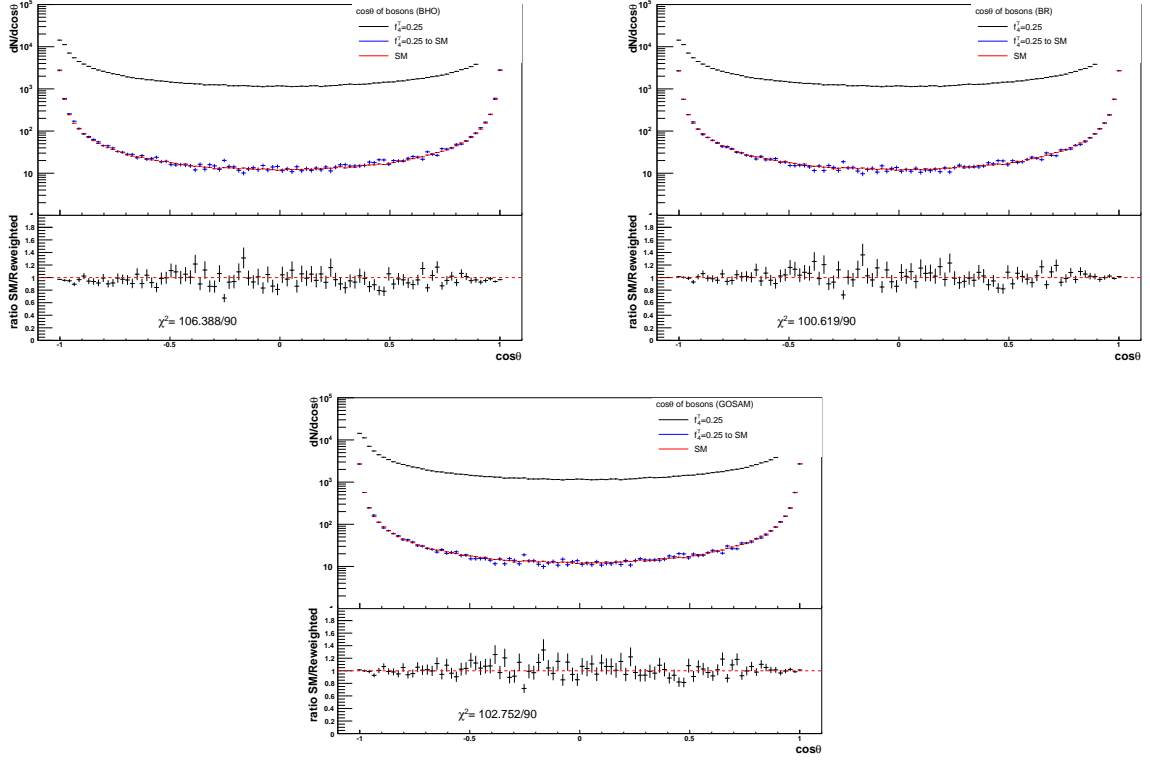


Figure 6.5: The scattering angle, $\cos\theta$ of the bosons in the center-of-mass frame of the bosons. A BSM sample with f_4^γ have been reweighted down to the Standard Model value of $f_4^\gamma = 0$ and compared to a Standard Model sample. The dashed red line indicates a ratio of one.

Fig. 6.6 on the next page shows the p_T distribution of one of the bosons reweighted with the three different generators. As expected there is a large fluctuation in the high p_T tail of the distribution. The reduced χ^2 is on the order of 1 for all generators, making the fit to the line at one valid. From these results it seems evident that the sign factor in the matrix element does not matter. The reweighted sample is similar to the sample generated with SHERPA, the slightly higher χ^2 originates from the lack of statistics in the generated sample. Or in other words, if the sign difference matters, the effects of this are so small, that they cannot be seen. The high similarity of the SHERPA sample and the reweighted sample as well as the reduced χ^2 indicates that the samples are alike even though they have been produced with two 'different' matrix elements.

This concludes the benchmarking of the model implemented in the matrix element generator GoSam. The model has proved to give differences in the amplitude of $\sim 0.02\%$ compared to MCFM, MadLoop and the Standard Model implemented in GoSam. Where the three Standard Model generators agree within $\sim 10^{-4}\%$, the additional diagrams in the TGC model seem to give rise to some small numerical effects, when calculating the amplitude with all TGC's set to the Standard Model values. It is expected that explicit hard-coding of the TGC Feynman rules in the FORM language would decrease these slight effects (and improve the timing studies) and thus would be an excellent beginning for further studies.

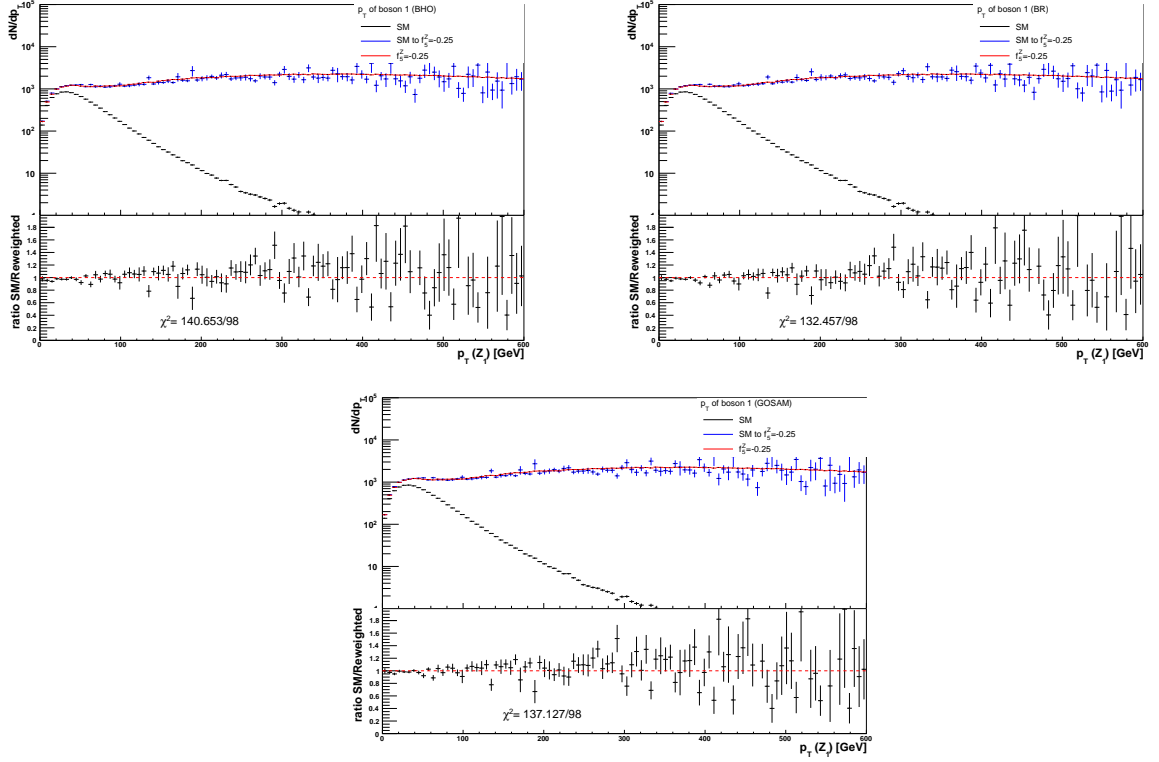


Figure 6.6: A Standard Model sample generated with SHERPA is reweighted up to the value of $f_5^Z = -0.25$ with the three generators BHO (upper left), BR (upper right) and GoSam (bottom) and compared to the BSM sample generated with SHERPA at the same coupling value. The dashed red line indicates a ratio of one.

The matrix element is in perfect agreement with the generators BHO and BR, both when examining Standard Model samples and TGC samples. The reweighting method using the GoSam generator has been validated by reweighting a TGC sample down to the Standard Model values and the reverse. All three generators perform well overall, giving rise to reduced χ^2 around one. The sign difference between the vertex rules from [13] and [14] does not affect the reweighted sample, hence the matrix element implemented in GoSam should be completely valid.

Thus left is to study the effects of the next-to-leading order corrections and benchmark the amplitudes obtained with GoSam, before the full next-to-leading order effects of the anomalous couplings can be evaluated.

Reweighting Standard Model samples to next-to-leading order

Before reweighting the leading order samples, one should get a hint of how the off-shell structure and the virtual corrections affect the particle distributions. First the effects of the single resonant diagrams in the $pp \rightarrow e^+e^-\mu^+\mu^-$ process is analysed, by a comparison to the process, where singly resonant diagrams are not allowed. Next the effects of real emission corrections are analysed in SHERPA. Finally the effects of the virtual corrections are analysed in MCFM and MadLoop.

In this section a set of leading order SHERPA samples was generated with the setup described in Sec. 6.2.

7.1 Including the next-to-leading order contributions

The unclusion of next-to-leading order effects involves many subtleties which needs to be handled correctly. The main concern is that one has to make sure that the IR divergencies are properly cancelled as described in Sec. 2.4.2, such that no divergencies remain. In the reweighting algorithm this is done in a similar way as the method used in SHERPA, when an external one-loop generator is implemented¹ if the process is a proper $2 \rightarrow 4$ event. Once the decision of the event type has been made, SHERPA calls the one-loop generator and extracts a K -factor from the generator:

$$K_{finite} = \frac{c_0}{a_0}$$

as well as the remaining IR singularities:

$$K_1 = \frac{c_{-1}}{a_0}$$

$$K_2 = \frac{c_{-2}}{a_0}$$

with a_0 being the Born amplitude squared, c_0 the finite term and finally c_1, c_2 the remaining IR singularities. The IR singularities are only used as a check that the IR poles from the virtual corrections cancel against the IR poles from the real emission.

SHERPA normalises the finite and IR-divergencies to the Born amplitude given by the one-loop generator, since it provides the leading order matrix element itself. From here the matrix element generator in SHERPA uses the one-loop information as follows:

$$|M_{one-loop}|^2 = K_{finite}|M_{Born}|^2$$

¹Information obtained by reading the SHERPA code.

SHERPA then provides the full event weight:

$$d\sigma = w(PDF) \left[|M_{Born}|^2 + |M_{one-loop}|^2 + |M_{real}|^2 \right]$$

The returned amplitude from GoSam contains both the finite term of the loop corrections, as well as the remaining IR singularities. It also returns the IR singularities from the real emission corrections to the tree level diagrams, such that the same consistency check can be performed. But it does not include the finite term from the real emission diagrams. This must be estimated from another source, or a decision must be made not to include it.

Fortunately most generators includes the real emission corrections themselves. This means the sample generated with the real emission corrections already have taken the finite term from the real emission into account and it is thus not necessary to take these into account in the reweighting.

As a consistency check of the one-loop amplitude the algorithm checks that the single and double pole from the virtual corrections, c_{-1}, c_{-2} , match against the single and double pole from the real emission, $IR(1), IR(2)$. If the singularities do not cancel, the event is discarded by returning a zero amplitude. Implemented in the algorithm is then the inclusion of the finite term in the next-to-leading event weight:

$$\begin{aligned} |M_{one-loop}|^2 &= \frac{\alpha_S(\mu)}{2\pi} \frac{(4\pi)^\varepsilon}{\Gamma(1-\varepsilon)} \cdot g^{2b} \cdot c_0 \\ &= \frac{\alpha_S(\mu)}{2\pi} \cdot g^{2b} \cdot c_0 \text{ for } \varepsilon = 0 \end{aligned}$$

with g being the Born coupling and b being the power of this coupling. Hence the full event weight will be:

$$\begin{aligned} d\sigma &= w(PDF) g^{2b} \left[a_0 + \frac{\alpha_S(\mu)}{2\pi} \frac{(4\pi)^\varepsilon}{\Gamma(1-\varepsilon)} \cdot c_0 \right] \\ &= w(PDF) g^{2b} \left[a_0 + \frac{\alpha_S(\mu)}{2\pi} \cdot c_0 \right] \text{ for } \varepsilon = 0 \end{aligned}$$

7.2 Effects of the single resonant diagram

In the full off-shell analysis in this thesis the single resonant diagrams are allowed to contribute and it is necessary to study the effects these diagrams have on the $pp \rightarrow e^+e^-\mu^+\mu^-$ sample. For this test four samples were generated: A $pp \rightarrow e^+e^-\mu^+\mu^-$ sample, a $pp \rightarrow Z^*Z^* \rightarrow e^+e^-\mu^+\mu^-$ sample where the Z-bosons are allowed to be off-shell, a sample with $pp \rightarrow Z^*\gamma^* \rightarrow e^+e^-\mu^+\mu^-$, and finally a sample with $pp \rightarrow \gamma^*\gamma^* \rightarrow e^+e^-\mu^+\mu^-$ (scaled with a factor of 100). The last three samples will thus not include the single resonant diagram, but are instead included to show the effects of the different contributions to the off-shell double resonant diagrams.

The effects of the Z^*Z^* diagrams are expected to be similar to the on-shell production samples. The M_{ZZ} distribution is expected to be smeared, since the Z boson no longer have to be produced on mass shell. Because of the phase-space cuts in the sample, the peak in the invariant mass distribution is not located at 182 GeV, but instead at 200 GeV. The $Z^*\gamma^*$ sample is expected to be smeared slightly above the Z mass, while no significant peak is expected in the $\gamma^*\gamma^*$ sample, since the only requirement is that the photons produced are energetic enough to create an electron or muon pair.

If one includes both the single and double resonant diagrams in a sample one should then expect two peaks in the M_{VV} distribution: One slightly above the Z mass and one slightly above twice the Z mass, corresponding to either one or two Z bosons being created. The single resonant diagrams are expected to contribute to the low M_{VV} end, since the probability of

creating a single boson at low energies are higher than the probability of creating a pair of bosons. The additional emission of a $Z^*\gamma^*$ with enough energy to produce a second lepton pair can happen down to relatively low energies, since the production threshold of the muons is a few hundred MeV and less for electrons.

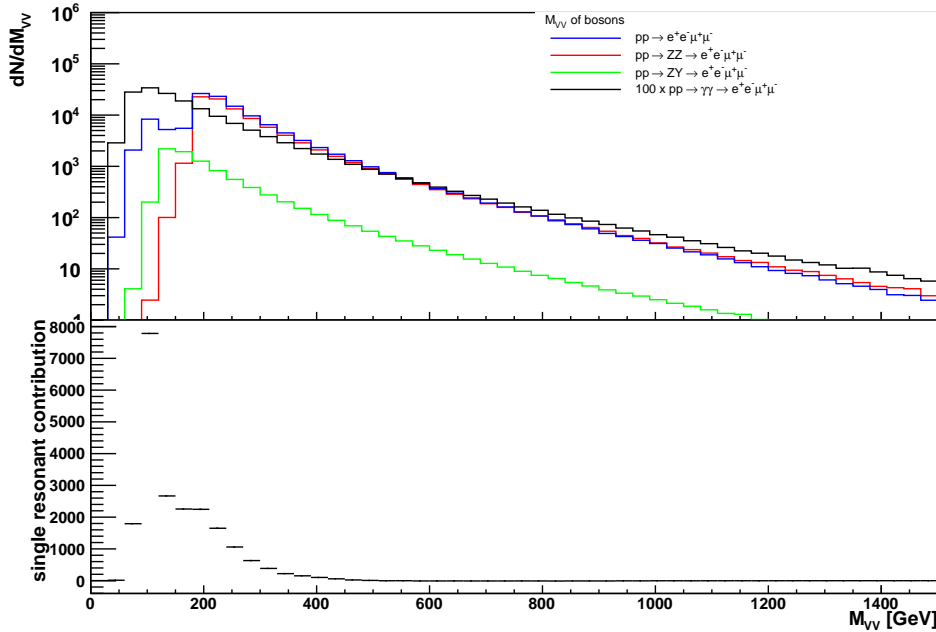


Figure 7.1: Four samples showing the off-shell structure of the Z^*/γ^* pair-production in the distribution of the invariant mass of both Z 's.

In Fig. 7.1 it is evident that an inclusion of off-shell photons gives an additional contribution to the invariant mass distributions down towards lower invariant mass as expected. The massive Z -boson requires more energy to be produced, hence the events from the $pp \rightarrow Z^*Z^* \rightarrow e^+e^-\mu^+\mu^-$ sample only has a slight tail below the shifted production threshold at 200 GeV. The full off-shell sample $pp \rightarrow e^+e^-\mu^+\mu^-$ includes the single resonant diagrams. The estimated contribution from these diagrams and the cross terms between the single and double resonant diagrams are shown in the lower plot, where the three double resonant samples have been subtracted from the full off-shell sample. This is of course only for shown for pedagogical reasons; In a full data sample this cannot be done, but instead cuts on physical distributions must be performed in order to distinguish the two production methods from each other.

The single resonant contribution shows up at low M_{VV} as expected and seems to be the dominant production method at the Z mass peak in the invariant mass distribution. This is explained through the Breit-Wigner propagator factor in the double resonant diagrams. The probability of creating two Z bosons decrease with decreasing energy, since it would require to 'pick up' two bosons from the Breit-Wigner tail, which has a very small probability. Thus the dominant production method is the single resonant diagram at low M_{VV} . But of course the subtraction method does not account for the cross terms between the single and double resonant diagrams, hence these are also a part of the lower plot in Fig. 7.1. Hence it is not explicitly known which fraction of the distribution the single resonant diagram accounts for.

Shown in Fig. 7.2 on the facing page is the invariant mass of the boson reconstructed from an electron pair. This clearly shows the wide spectrum of the off-shell photons, compared to the rather narrow spectrum of the Z^* bosons. Hence if one wishes to remove the single-resonant diagrams, requiring a boson mass in the range of 80 to 100 GeV would greatly reduce the process. This is especially important if one wishes to study the TGC vertex. This

is not present in the single resonant diagrams and thus most of the contributions from these processes needs to be removed before one can make precision measurements of the vertex in order to set limits on the couplings. The cut on the boson mass distribution removes a lot of the single resonant diagrams, and for further precision, one could require the invariant mass of the Z bosons to be above ~ 150 GeV, where the single resonant distribution begins to fall off.

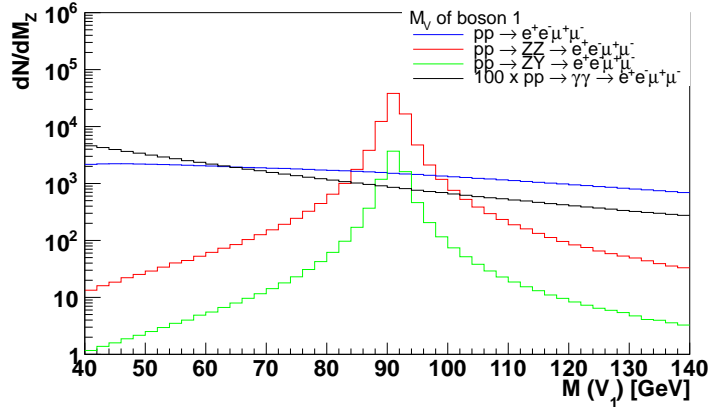


Figure 7.2: Four samples showing the off-shell structure of the Z^*/γ^* pair-production in the mass distribution of one Z.

In summary the effects of the single resonant diagram are greatest at low center-of-mass energy. This is in direct contrast to the effects of the TGCs, which show up in the high energy tails of the various distributions. Hence including the single resonant diagrams should not give effects similar to the effects of the couplings, and show up as signs of new physics. Including these diagrams to the reweighting code will also give better results when reweighting a full off-shell sample, since the double resonant matrix element is not able to describe these low-energy distributions.

7.3 Real emission effects

The effects of the real emission corrections are again studied with SHERPA. Two sets of SHERPA samples have been generated; One including the real emission corrections (denoted the real emission sample) and one without (denoted the leading order sample). The real emission sample has further been categorised into two: The no-jet sample (denoted the $2 \rightarrow 4$ sample) and the jet-sample (denoted the $2 \rightarrow 5$ sample). The division of the real emission sample is included to visualise how the events in the real emission sample is distributed.

The real emission sample is expected to lower the cross section of the process, because of the sign difference in the real emission diagrams. This is also observed in the samples, where the leading order sample has a cross section of (0.0092 ± 0.003) pb and the real emission sample has a cross section of (0.0089 ± 0.002) pb. The real emission sample has been generated with a CKKW-cut² of $(20\text{GeV}/E_{CM})^2$. The effects of this cut will be described later.

Normalising to the same integrated luminosity shows the effects of the real emission. Shown in Figs. 7.3 on the next page and 7.4 on page 71 are the real emission sample (black),

²The merging of parton showers and matrix elements is highly non-trivial. It requires an introduction of a cut, steering the generator to use either the parton shower approach or the matrix element approach to describe the generation and evolution of jets appearing when real emission effects are taken into account. See eg. [24] for further information of the merging method.

the leading order sample (green), the $2 \rightarrow 4$ sample (red) and last the $2 \rightarrow 5$ sample (blue).

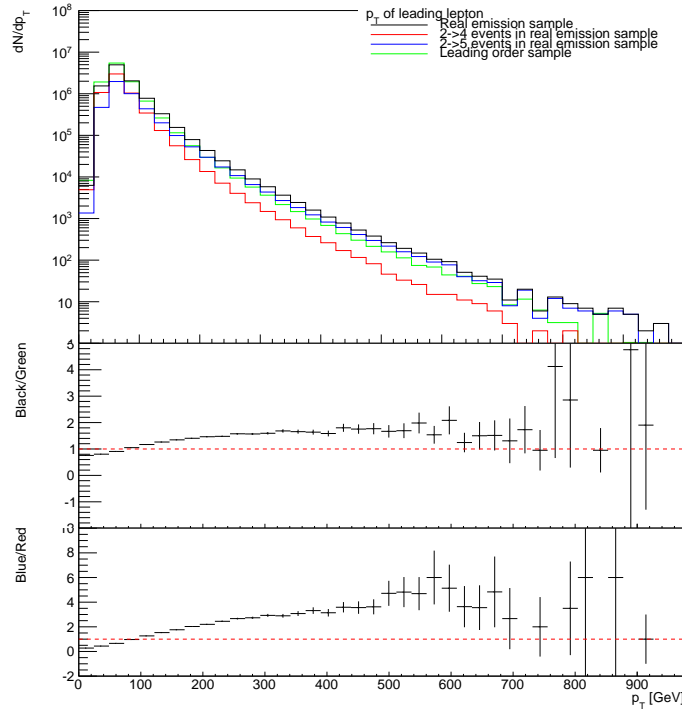


Figure 7.3: p_T of the leading lepton in a SHERPA $pp \rightarrow e^+e^-\mu^+\mu^-(j)$ sample. The dashed red line indicates a ratio of one.

In Fig. 7.3 the p_T distribution of the leading lepton is shown. The ratio (Black/Green) shows that the inclusion of real emission in the process increases the number of events in the high p_T tail while slightly decreasing the number of events in the peak at low p_T . This is explained by the boost received by the ZZ system when an incoming quark radiates a gluon. This boost will increase the number of high p_T leptons, thus resulting in the high p_T tail.

The ratio (Blue/Red) in Fig. 7.3 is dominated by the $2 \rightarrow 4$ events at low p_T , whereas the high p_T tail is dominated by the $2 \rightarrow 5$ events. The low p_T events have received a smaller boost, by emitting soft, collinear or no particles at all. The high p_T events have, on the other hand, received a large boost from an emitted particle. If the parton is energetic enough to boost the ZZ system significantly, it will be energetic enough to be distinguished from the outgoing leptons, resulting in a $2 \rightarrow 5$ event. Hence the tail is dominated by the $2 \rightarrow 5$ sample. Assuming that the virtual corrections are not p_T dependent, one would expect the virtual contributions to be dominating in the low p_T end, where the $2 \rightarrow 4$ events dominate. But this assumption will be shown not to be valid.

The boost obtained by the system is again evident when looking at the difference in η of the bosons. The $\delta\eta$ variable hints whether the bosons are collinear (giving small $\delta\eta$) or have a wider angle between them. It is evident from Fig. 7.4 on the next page that the bosons with accompanying jets (blue) have a narrower spectrum than the events without (red). This is again related to the boost gained by the system, when jets are emitted. The boost results in more collinear bosons, hence giving rise to a smaller $\delta\eta$.

Testing the dependency on the cut applied to SHERPA when generating the real emission events, two additional smaller samples were generated; One with an increased cut of $(100\text{GeV}/E_{CM})^2$ and one with a decreased cut of $(10\text{GeV}/E_{CM})^2$. The effects of the change in cuts are seen in the p_T distributions in Fig. 7.5 on page 72.

There is still a slightly higher p_T tail in the real emission samples. There is a steep rise in the ratio (Blue/Red) in the low-cut sample at p_T greater than ~ 20 GeV, meaning that

the $2 \rightarrow 5$ events dominate at lower p_T in the low cut sample compared to the initial cut and the high cut samples. The cut is thus a measure of how low p_T the outgoing partons are allowed.

The cross sections are also affected by the variation in cuts. The low cut sample obtains a cross section of $8.16 \cdot 10^{-3}$ pb, while the high cut sample obtains a cross section of $11.06 \cdot 10^3$ pb. The additional real emission is thus seen to decrease the cross section in the low cut scale, while the hard cut increases the cross section, since the finite term from the real emission has a smaller effect.

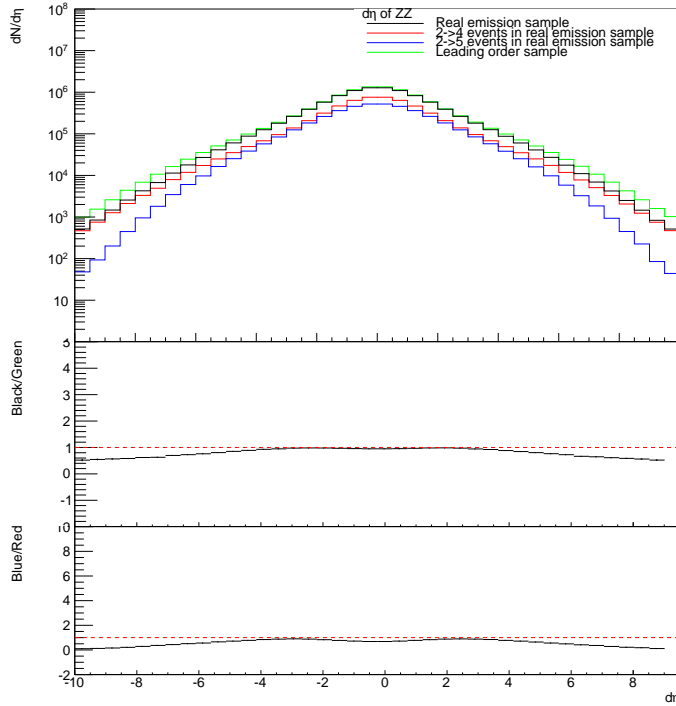


Figure 7.4: $\delta\eta$ in a SHERPA $pp \rightarrow e^+e^-\mu^+\mu^-(j)$ sample. The dashed red line indicates a ratio of one.

This then gives rise to the question of which cut to use in the simulation of these effects. Clearly one would strive for obtaining a simulation closest to the actual distributions obtained in data. Thus a reasonable cut would be at the level of acceptance of the detector, one provides simulations for. Ie. if the detector can detect jets down to eg. 20 GeV, the CKKW-cut should be set to this value. But the distributions and cross sections at this level, could prove not to be similar to those seen in data, and then the simulations again do not describe the physical world.

The issue with this cut is completely determined by the physicists ability to describe the world. If one was able to calculate to all orders of perturbation theory and did not have the need for scale dependent cuts and structure functions, these issues would (probably) not arise. Then all real emission effects would be finite, and the simulations and predictions would tend to go to the 'true' value observed.

Generally one distinguishes between three scenarios: Initial state radiation, final state radiation and 'real' radiation. Real emission events arising from the initial state partons carry IR divergencies, that will be absorbed into the parton density functions [24]. Likewise the IR divergencies obtained in the final state radiation are absorbed into the *fragmentation functions*, appearing when a parton is showered and collected into the hadrons detected in the detector [24]. The final divergent term are the terms, to which the subtraction discussed in Sec. 2.4.1 method apply.

The study concludes with the statements, that the inclusion of real emission to a process is not trivially done and relies on theoretical assumptions one needs to estimate the error on. But it is noticed that the inclusion of these effects tend to give higher p_T in the outgoing particles and slightly lower cross sections. Including the virtual corrections is expected to give effects in the lower p_T spectrum, since the proper $2 \rightarrow 4$ events are primarily distributed here. It is thus expected to give an increase in low p_T events giving an overall rise to the production cross section.

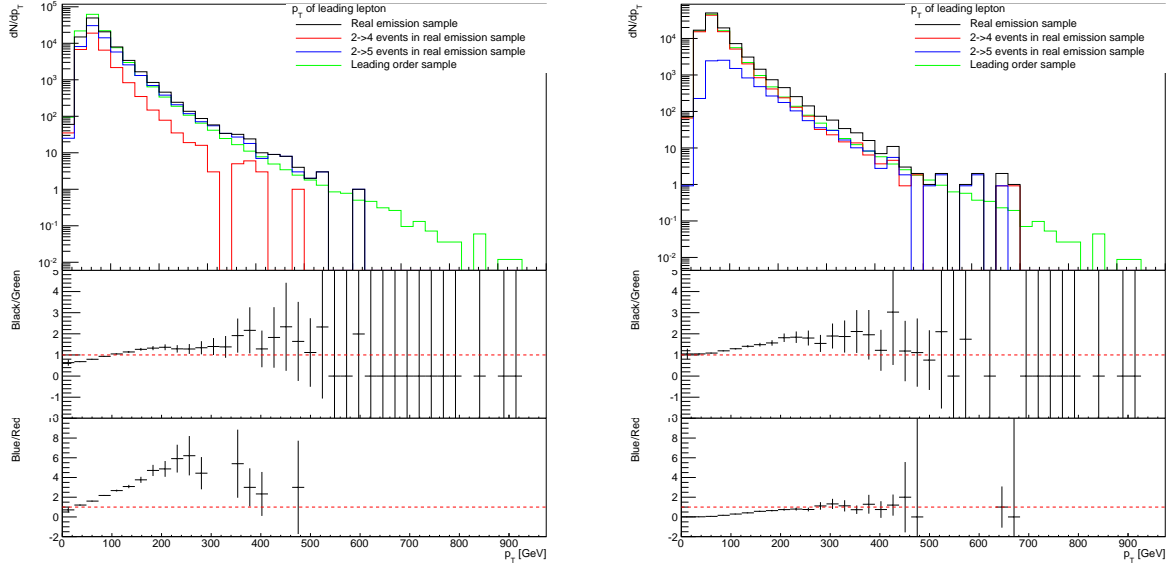


Figure 7.5: p_T of the leading lepton obtained by varying the CKKW-scale in SHERPA. Left is shown the distributions obtained with the cut at 10 GeV, right the distributions obtained with a cut of 100GeV. The dashed red line indicates a ratio of one.

7.4 Effects of the virtual corrections

In this test the cross sections for the Standard Model process $pp \rightarrow ZZ \rightarrow e^+e^-\mu^+\mu^-$ have been generated with MCFM at $\sqrt{s} = 7$ TeV and a full sample has been generated with MadGraph+MadLoop at next-to-leading order. The figures obtained with MCFM have the following samples: Leading order (green), leading order plus virtual corrections (blue), real corrections (red) and total next-to-leading order (black). The distributions are the differential cross sections per bin but they are comparable to the number of events per bin through $dN = \mathcal{L}d\sigma$. The MadGraph+MadLoop samples has two distributions, the leading order sample (blue) and the next-to-leading order sample (red).

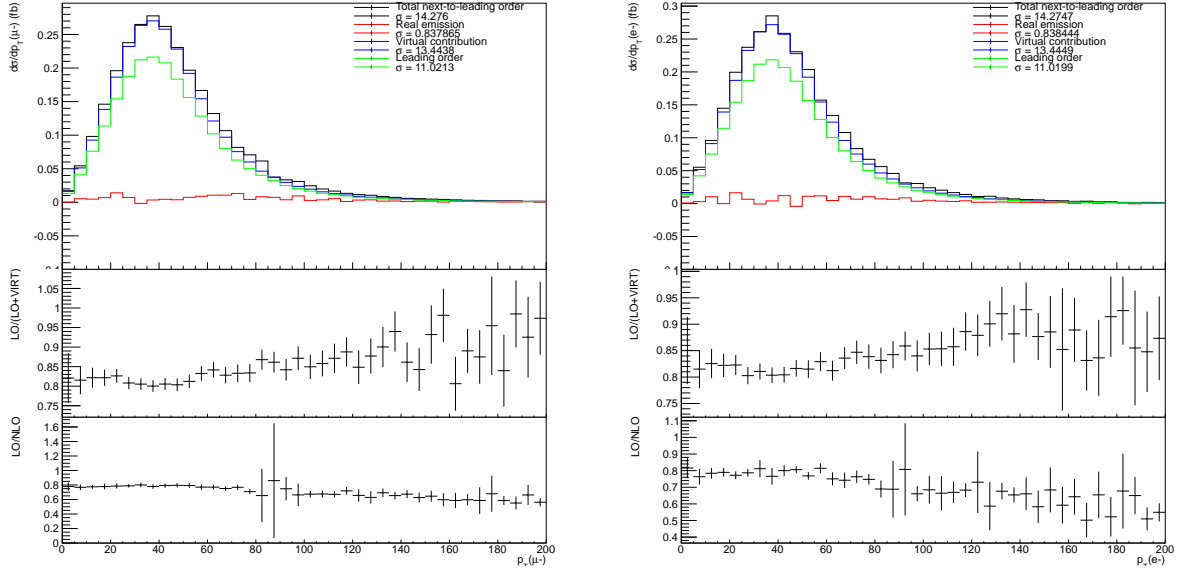


Figure 7.6: p_T distributions of the electron and the muon generated by MCFM without the single resonant diagrams included. The dashed red line indicates a ratio of one.

Fig. 7.6 shows the differential cross section per p_T bin of the electron and the muon obtained with MCFM. The plots given below the distributions show the ratio of the leading order corrections to the leading order plus virtual corrections as well as the leading order to the total next-to-leading order corrections. The renormalisation and factorisation scales have been set to the Z-mass when generating the samples.

Most noticeable is the increased differential cross section at low p_T when including the virtual corrections. This is as expected, since the dominant process at low p_T was shown to be the 'true' $2 \rightarrow 4$ processes. At p_T around 100 GeV the real emission effects contribute significantly, giving a slight decrease in the (LO/NLO) ratio.

MCFM gives the results of the finite term of the real emission with the correct sign, ie. the differential cross section for the real emission can be negative. This is explicitly seen in Fig. 7.7 on the following page, where the real emission goes below zero such that the total next-to-leading order distribution is less than the virtual corrections. This is also the reason why the K-factor obtained from the LO/NLO ratio increases, because at high p_T the real emission contributes with a positive differential cross section just as the virtual contribution does.

An approximate K-factor can be extracted from the lower ratio. The ratio LO/NLO is ~ 0.8 at low p_T , thus the K-factor is ~ 1.2 here. At high p_T the increased effects of the real emission diagrams contribute significantly, giving rise to a high p_T K-factor of ~ 1.4 . It is more difficult to extract an approximate K-factor from the LO/(LO+VIRT) ratio, as the errors are larger. But a reasonable estimate would be that the low p_T K-factor is 1.2, since the virtual corrections dominate here. At high p_T the K-factor is estimated to be ~ 1.1 .

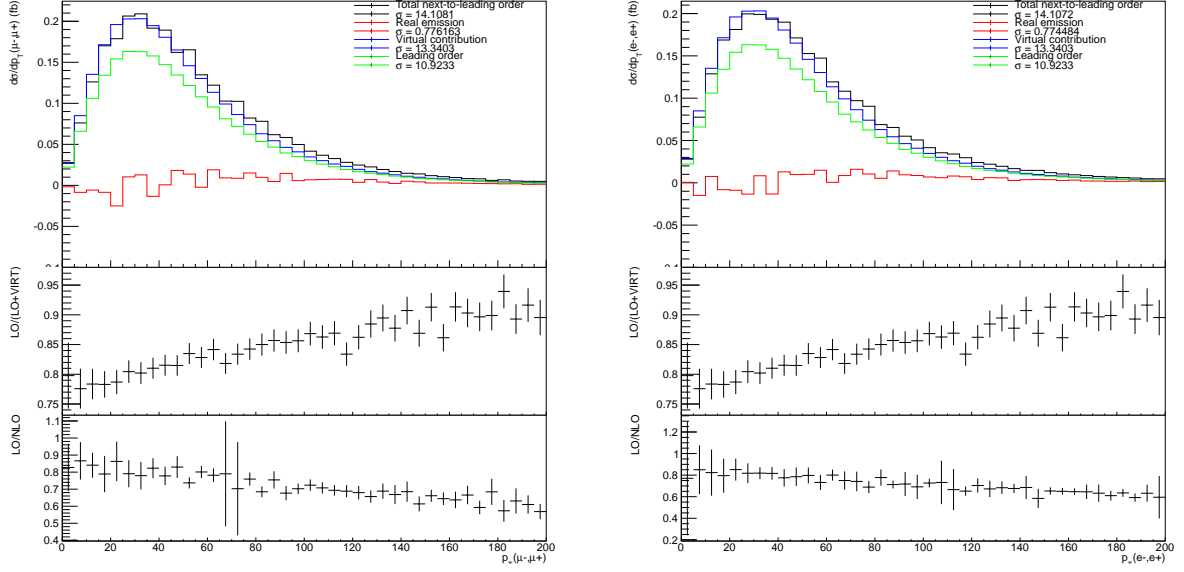


Figure 7.7: p_T distributions of the two Z bosons generated by MCFM without the single resonant diagrams included. The dashed red line indicates a ratio of one.

To check the distributions obtained with MCFM the process $pp \rightarrow e^+e^-\mu^+\mu^-$ was generated with MadGraph implemented with MadLoop at both leading and next-to-leading order. The real emission events was showered with Pythia [31, 32]. The lack of statistics in the sample results in increased errorbars in the high p_T tail, such that the K-factor is difficult to extract. But it is noticed that the ratio (LO/NLO) is comparable to the obtained (LO/NLO) from MCFM.

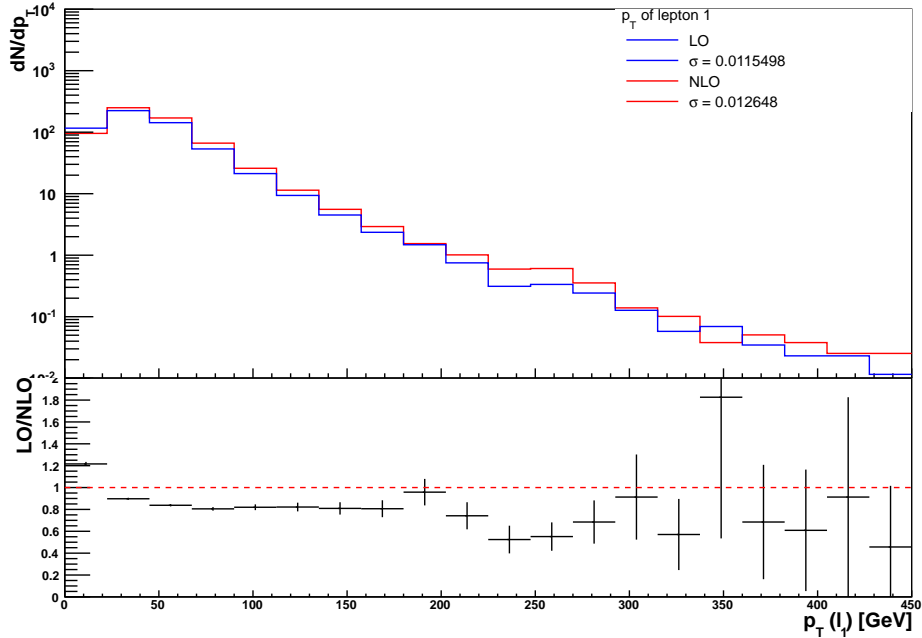


Figure 7.8: p_T of the electron generated with MadGraph+MadLoop at leading and next-to-leading order.

The p_T spectrum of the electron obtained with MadGraph+MadLoop show an overall increase of events in the next-to-leading order sample. The high p_T tail is again due to the real emission boosting the system. The next-to-leading order corrections seem to decrease

slightly, when all the single resonant contribution is taken into account. In MCFM the next-to-leading order K-factor is ~ 1.2 at low p_T while being ~ 1.4 at $p_T \sim 200$ GeV. In the MadGraph+MadLoop sample the K-factor is slightly less, being ~ 1.1 at low p_T while being ~ 1.3 at $p_T \sim 200$ GeV and at higher p_T it is estimated to be ~ 1.3 .

The renormalisation and factorisation scale dependence is tested in MCFM as described in Sec. 2.3. The scales were set to M_Z when generating the above distributions, so two other runs are created, this time only calculating the total cross section. The additional samples are denoted (A) and (B) and have been generated with the following scales:

$$\begin{aligned} \text{A: } \mu_R &= 0.5 \cdot M_Z = 45.594, \mu_F = 2 \cdot M_Z = 182.376 \\ \text{B: } \mu_R &= 2 \cdot M_Z = 182.376, \mu_F = 0.5 \cdot M_Z = 45.594 \\ &\text{with the initial scales being} \\ \text{0: } \mu_R &= \mu_F = M_Z = 91.188 \end{aligned}$$

The cross sections obtained with MCFM are given in Table. 7.1.

Case	σ (fb)	Error (fb)
0	14.44	0.013
A	14.78	0.056
B	14.02	0.050

Table 7.1: The cross sections obtained with MCFM when varying the factorisation and renormalisation scales.

This interval gives rise to a scale uncertainty of 2.62%. It is estimated that the uncertainty on the next-to-leading order corrections obtained by the reweighting algorithm is slightly higher than the uncertainty obtained with MCFM. The reweighting algorithm already shows signs of a slight disagreement with MCFM, giving rise to differences at around 0.02%. The possibility of numerical instabilities in the large reweighting sample, also would increase the uncertainty due to the scale choice.

The uncertainty obtained by MadGraph when generating the sample was ${}_{-2.1}^{+2.6}\%$ and thus in good agreement with the MCFM uncertainty.

7.5 Testing the reduction libraries in GoSam

Before producing a full next-to-leading order sample, it is necessary to check if both libraries implemented in GoSam are consistent with each other. A small set of 5000 events were recorded for a $pp \rightarrow ZZ \rightarrow e^+e^-\mu^+\mu^-$ sample, to check if the weights obtained with each of libraries agreed. The renormalisation scale has been set to the Z mass.

As seen in Fig. 7.9 on the following page the two integral libraries agree. The extracted K-factor from both generators in this subset of events seem to agree with MCFM as well, having a mean K-factor of ~ 1.25 . The agreement between the two integral libraries are perfect at leading order, as well as at next-to-leading order. Hence the choice of integral library should not affect the next-to-leading order samples.

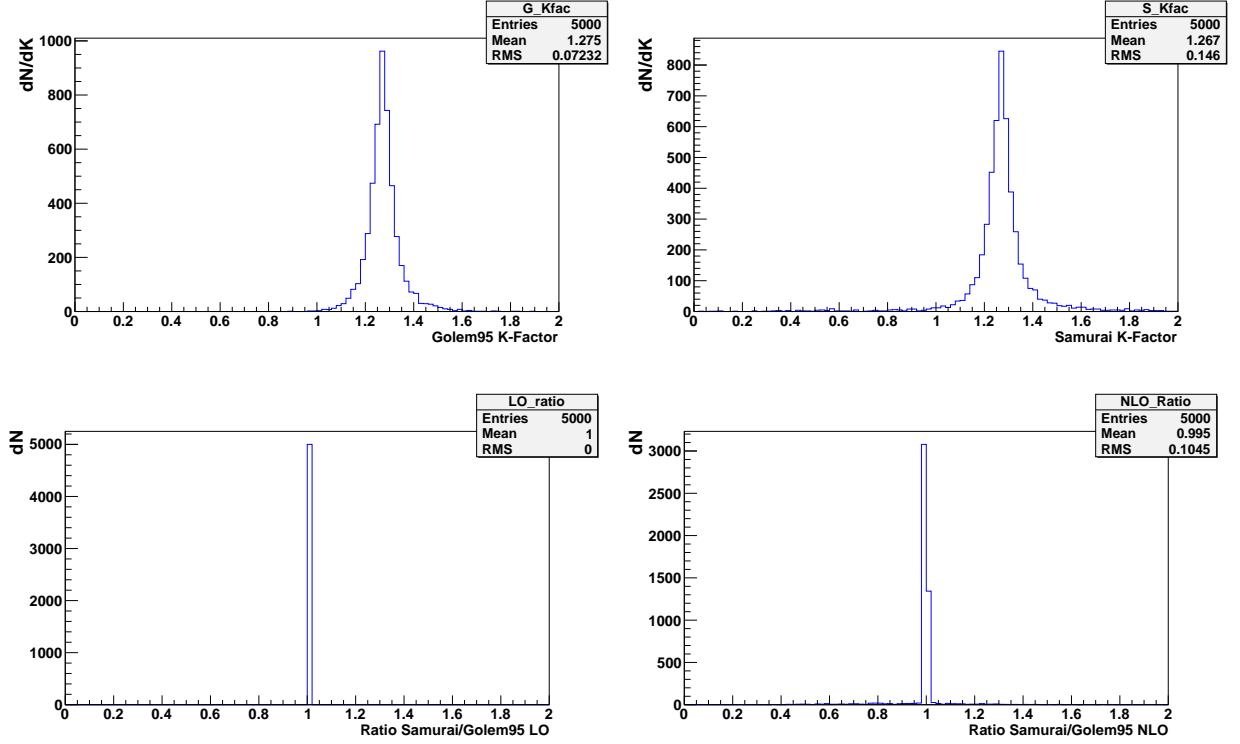


Figure 7.9: The initial test of the two integral libraries implemented in GoSam. The upper two figures show the K-factor extracted from the integral libraries Golem95 (left) and Samurai (right). The bottom two show the ratio between the weights obtained with each of the generators for LO (left) and NLO (right).

7.6 On-shell ZZ samples

The benchmarking of the virtual corrections obtained in the reweighting method is performed against MCFM. The onshell SHERPA sample (1) is reweighted using Golem95 and Samurai separately and the shape of the (LO/NLO) ratio is compared to the ratio (LO/(LO+VIRT)) obtained with MCFM. The samples have been reweighted with a fixed factorisation and renormalisation scale $\mu_F = \mu_R = M_Z$ to be directly comparable to MCFM. After the initial results, the uncertainty due to the scale choice is estimated in the reweighting method, and a third scale choice is also tested to see the effects of a dynamic renormalisation scale.

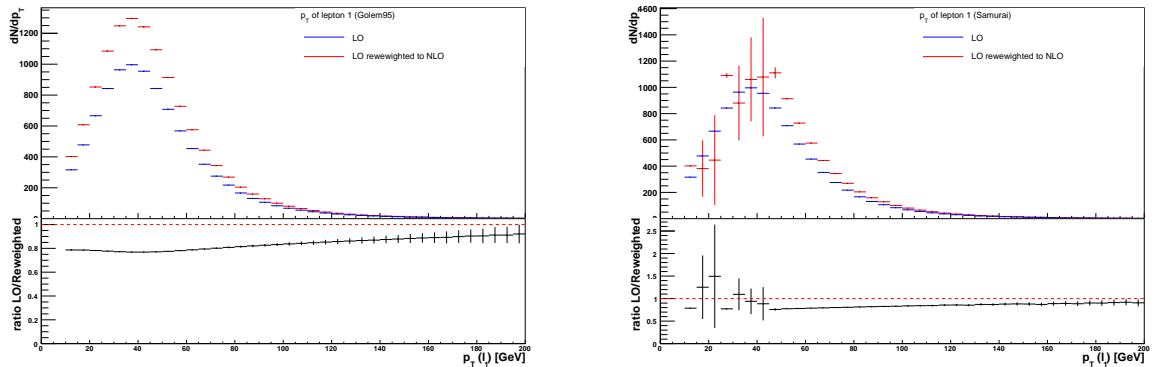


Figure 7.10: The initial test of the two integral libraries implemented in GoSam. Shown is the p_T distribution of the electron at leading order (blue) and next-to-leading order (red). The dashed red line indicates a ratio of one.

From 7.10 on the preceding page it is evident that Samurai has a few events in which the errorbars are significantly high. These effects are most likely caused by a set of events having high weights, and it is thus necessary to investigate what causes these high weights.

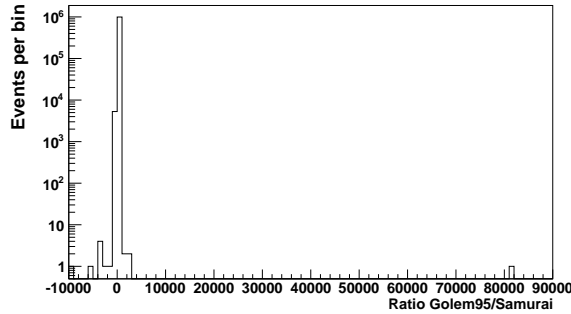


Figure 7.11: The ratio of the NLO weights obtained with Golem95 and Samurai.

It is evident that the unusually high event weights obtained with Samurai are only a small subset of the weights. But the weights are so large, that the errors in the bins where the events are located, increase sufficiently. It is noticeable that all the events are located in the low p_T bins, and after careful investigation of the distributions, no other trend was found, neither in angles or mass spectra and no convincing arguments have been obtained of what causes these high weights. It was first assumed to be numerical instabilities, but this would cause much higher (lower) ratios, since numerical instabilities usually return eg. 10^{-32} or similar. The authors of GoSam was contacted with regards to the cause of these weights but they have not responded to the inquiries. Because of these instabilities in Samurai it was decided to continue using only Golem95.

The p_T spectrum of the electron is compared to the spectrum obtained with MCFM.

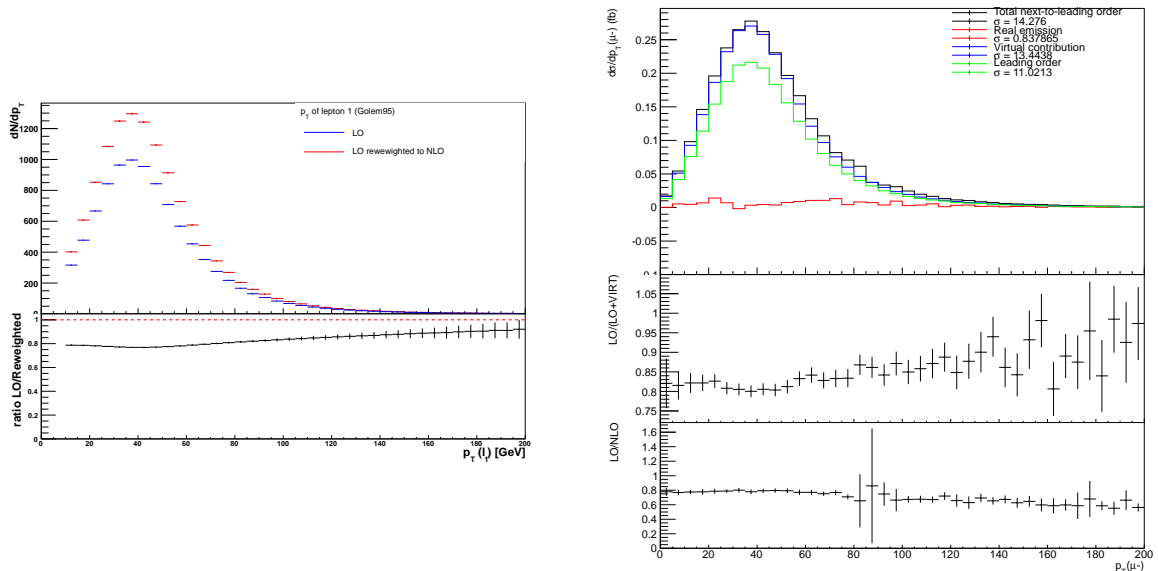


Figure 7.12: The p_T spectrum of the electron obtained with the reweighting method (left) and MCFM (right).

By eye the two ratios ($LO/(LO+VIRT)$) and ($LO/Reweight$) have similarities. Both have ratios at around 0.8 at low p_T and show an increase at around 50 GeV. Both ratios end up at approximately 0.95 at 200 GeV. So visually they are comparable. A χ^2 test and

a Kolmogorov-Smirnov [22] test was performed on the two ratios to check if they really are comparable. The Kolmogorov-Smirnov test was included, since this is sensitive to shape and normalisation comparisons, such as needed here. The initial test results in Fig. 7.13.

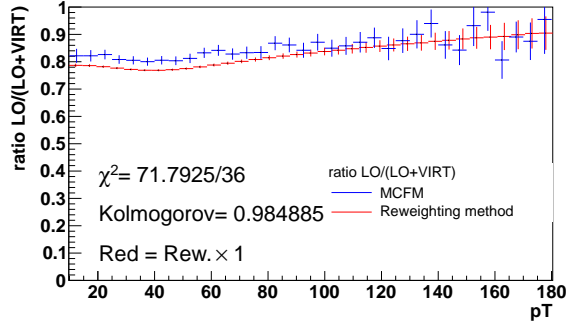


Figure 7.13: The comparison of the two ratios (LO/(LO+VIRT)) and (LO/Reweighted) obtained from MCFM and the reweighting method.

By eye it is evident that the reweighting method is similar in shape as the ratio obtained from MCFM. But the reweighting method seem to overestimate the next-to-leading order contribution at low p_T up to ~ 60 GeV. Hence a scaling test was performed to see if one could obtain better χ^2 and Kolmogorov-Smirnov probability if an overall scaling of the reweighting method was performed. This results in a χ^2 distribution, shown in Fig. 7.14.

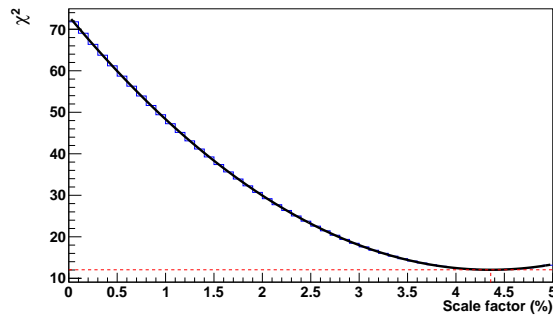


Figure 7.14: The χ^2 obtained when scaling the reweighted distribution in steps of 0.1%.

The χ^2 test show a minima at 4.4% scaling factor. Hence there is a difference of 4.4% between the two generators. This scaling can be used as a correction factor on the reweighting method, if the sample obtained with MCFM is assumed to be the true distribution. It is evident from both the Kolmogorov-Smirnov probability and by eye, that the two methods are in perfect agreement, when the correction factor is applied. The author has chosen not to use the correction factor, since there is further need for comparison against MadGraph+MadLoop.

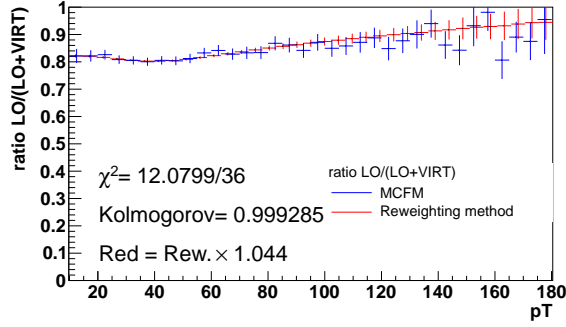


Figure 7.15: The comparison of the two ratios (LO/(LO+VIRT)) and (LO/Reweighted) obtained from MCFM and the reweighting method where the reweighting method has been scaled with 4.4%.

The uncertainty due to scale choice is estimated by varying the factorisation and renormalisation scale.

$\mu_F = \mu_R =$	σ (fb)	Error (fb)
M_Z	11.6161	0.012
$0.5 \cdot M_Z$	11.4379	0.011
$2 \cdot M_Z$	12.1663	0.012

Table 7.2: The cross sections obtained with the reweighting method when varying the factorisation and renormalisation scales.

The uncertainty due to scaling is 3.3% in the reweighting sample. This is comparable to the uncertainty obtained with MCFM at 2.62%.

The results obtained in the above assume a fixed factorisation- and renormalisation scale. There is no convincing arguments that this should be the case. In a physical process, at least the factorisation scale varies with energy, hence a dynamic scale is preferable. Thus a sample has been reweighted with a dynamic scale of $\mu_F = \mu_R = M_{VV}$. The results are shown in Fig. 7.16.

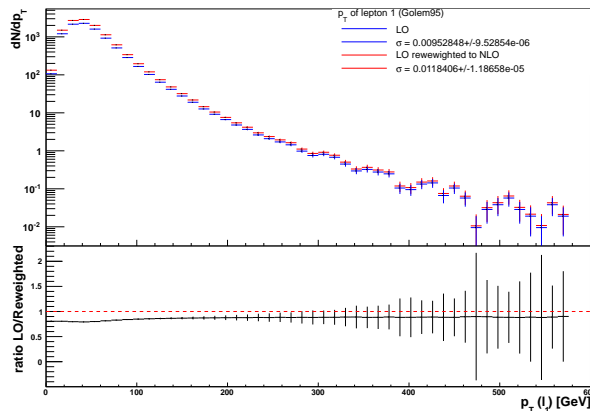


Figure 7.16: The p_T spectrum of the electron obtained with the reweighting method with a dynamic factorisation and renormalisation scale of $\mu_F = \mu_R = M_{VV}$. The dashed red line indicates a ratio of one.

It is thus evident that the inclusion of virtual corrections apply to all parts of the spectrum. It is also evident, that the virtual corrections are p_T dependent. This can be explained through the strength of α_S , since this decreases with increasing energy. But other effects must be present as well, since the same shape was seen in the samples generated with fixed factorisation and renormalisation scales. Hence the virtual corrections must be dependent on the incoming momenta in a non-trivial way. Had the virtual effects only been p_T dependent through α_S one would expect a constant decrease in the virtual corrections with increased p_T , thus not having the shape observed. The exact explanation for the increase at $p_T \sim 50$ GeV is not known to the author.

Adding the real emission to the sample would cause an increase in events in the high p_T spectrum and a slight decrease in the low p_T spectrum, thus possibly obtaining a spectrum similar to the spectrum obtained with MadGraph+MadLoop.

The scale uncertainty is obtained by varying the factorisation and renormalisation scales and results in the cross sections given in Table 7.3.

$\mu_F = \mu_R =$	σ (fb)	Error (fb)
M_{VV}	11.8407	0.012
$0.5 \cdot M_{VV}$	12.2994	0.012
$2 \cdot M_{VV}$	10.5939	0.011

Table 7.3: The cross sections obtained with the reweighting method when varying the factorisation and renormalisation scales.

The scale uncertainty obtained with the reweighting method results in 7.2%, and is thus bigger than the uncertainties obtained with MCFM and MadGraph+MadLoop and the reweighting method with fixed scales. This was more or less expected, since the method used to obtain the cross section is not a direct calculation. The cross section is estimated by integrating a distribution. The integral is affected by the axis of the histogram, hence if the distribution exceeds the range of the axis, the cross section will be underestimated. The integrated distribution is $\cos \theta$ of the bosons, which cannot exceed the axis range of $(-1,1)$, hence all events are taken into account in the integral. But the distributions are highly affected by numerical precision in both the leading order sample and the parameters used in the reweighting, hence the measure will not be as precise as the directly calculated cross sections from MCFM.

One might have noticed that the cross section obtained with SHERPA is lower than obtained with MCFM. The reason for this lower cross section is that the SHERPA sample is generated with cuts, hence the cross section will automatically become lower than MCFM. The overall K-factor obtained with MCFM is 1.22, while the K-factor obtained with the reweighting method is 1.24 giving an overall factor of 1.64% difference between generators.

Uncertainties from the chosen PDF can be measured within the set itself, ie. it is not necessary to generate and reweight samples with a different choice of PDFs. The uncertainty is estimated from the best fit value of the PDF set by varying the PDF set number up and down, just as done when estimating the uncertainty on the scale choice. The method is as follows [42]:

$$\Delta\sigma = \frac{1}{2} \left(\sum_{i=1}^{N_p} [\sigma(S_i^+) - \sigma(S_i^-)]^2 \right)^{1/2}$$

with $\Delta\sigma$ being the uncertainty on the cross section, N_p the number of eigenvectors in the set (the number of degrees of freedom or fit parameters), S_i^\pm the up(+) and down (-) values

of the PDF set. Because of the large number of degrees of freedom in the PDF set, only a small sample of 10000 events is used in the uncertainty estimate.

N_p	$(\sigma(S^+) - \sigma(S^-))^2$
1	0.048
2	0.002
3	0.002
4	0.129
5	0.005
6	0.009
7	0.011
8	0.014
9	0.066
10	0.134
11	0.119
12	0.006
13	0.064
14	0.092
15	0.046
16	0.013
17	0.016
18	0.005
19	0.004
20	0.014
21	0.006
22	0.001
σ	$\Delta\sigma$
11.8407	0.49

Table 7.4: The squared difference in cross sections obtained with the reweighting method when varying the PDF eigenvectors and the total uncertainty due to PDF choice.

Adding the virtual corrections to the leading order sample increases the cross section, hence in the $pp \rightarrow ZZ \rightarrow e^+e^-\mu^+\mu^-$ process with a dynamic factorisation and renormalisation scale at $\mu_F = \mu_R = M_{VV}$ one obtains:

$$\begin{aligned}\sigma_{LO+VIRT}^{rew.} &= 11.841 \pm 0.012(\text{stat}) \pm 0.85(\text{scale}) \pm 0.49(\text{PDF}) \text{ fb} \\ &= 11.841 \pm 0.98 \text{ fb}\end{aligned}$$

giving an increase compared to the leading order cross section of 24.26%.

7.7 Observables affected by the next-to-leading order corrections

In this section a short summary of the observables affected by the next-to-leading order corrections is provided. A distinction is made between the real emission effects and the virtual effects, but they may show similarities in the observables. The cause of these effects have been mentioned in the above sections.

The observables sensitive to real emission

- The p_T distributions of bosons and leptons. Effects are visible at p_T above 100 GeV.
- Difference in η between bosons. Effects are visible in the interval $[-4, 4]$.
- Invariant mass distribution of the bosons. Effects are visible below 200 GeV and above 400 GeV.

The observables sensitive to virtual corrections

- The p_T distributions of bosons and leptons. Effects are visible in the entire spectrum, but show a large effect at low p_T .
- Difference in η between bosons. Effects are visible above ± 4 .
- Distance between leptons. Effects are visible below 0.5 if the leptons are traced back to the same mother and above 6 if the leptons are from different mothers.

In other observables investigated the effects only showed up as an increase or decrease in cross sections, hence the ratios were flat. It is evident that the most sensitive variables to these corrections are similar, but the effects of each correction shows up in different parts of the distributions. Based on these observations and the observations made in Sec. 3, the effects of the next-to-leading order corrections in the TGC samples are studied in the p_T and M_{VV} distributions.

Next-to-leading order corrections in TGC samples

The final study will try to estimate the effects of adding next-to-leading order corrections to a TGC sample. It begins by evaluating the next-to-leading order corrections in the full off-shell sample at Standard Model couplings, then a sample generated with the TGC coupling of $f_5^Z = -0.25$ is reweighted to the Standard Model values, and finally the TGC samples with the full off-shell structure of the couplings is evaluated at next-to-leading order.

Another set of samples was generated in SHERPA with the same cuts as the on-shell samples, but with the following setup:

Process	No. of events	Generator	Beam energy (\sqrt{s})	Model	σ (pb)
1 $pp \rightarrow e^+e^-\mu^+\mu^-$	10^7	Amegic++	7000 GeV	SM	0.0113
2 $pp \rightarrow e^+e^-\mu^+\mu^-j$	$5 \cdot 10^5$	Amegic++	7000 GeV	SM	0.0120
3 $pp \rightarrow e^+e^-\mu^+\mu^-$	$5 \cdot 10^5$	Amegic++	7000 GeV	SM+AGC $f_5^Z = -0.25$	0.153
4 $pp \rightarrow e^+e^-\mu^+\mu^-j$	$5 \cdot 10^5$	Amegic++	7000 GeV	SM+AGC $f_4^\gamma = 0.25, f_4^Z = -0.47$ $h_1^\gamma = 0.13, h_1^Z = -0.25$	0.452

Table 8.1: The SHERPA input

For all samples the PDF set CTEQ6.6 has been used and showering has been performed in samples with real emission. This setup allows for the singly resonant diagrams as well. There is a small issue though, since the couplings $f_i^V, h_j^V, i = 4, 5, j = 1 \dots 4$ are only defined in the case where two bosons are on-shell. Hence when all three bosons are off-shell SHERPA generalises the one off-shell boson vertex by symmetrising the vertex [43]:

$$Z^*Z^*V^* = Z_1Z_2V_3^* + Z_1Z_3V_2^* + Z_2Z_3V_1^*$$

Strictly speaking this assumption is not true, since the operators generating the off-shell couplings are different from the operators generating the on-shell couplings. As stated in Sec. 3.3 this relates the on-shell couplings to each other in the limit one requires $SU(2)$ gauge invariance and two of three off-shell bosons are put on-shell. Hence when 'turning on' one on-shell coupling others will be 'turned on' as well, explicitly through Eqn. 3.3 on page 36. This feature is not implemented in SHERPA, ie. what SHERPA does is not completely valid. There is a workaround, where the author explicitly calculates the couplings, and then generates a new SHERPA sample with the 'correct' off-shell structure. This is sample 4 in Table 8.1.

8.1 $pp \rightarrow e^+e^-\mu^+\mu^-$ at next-to-leading order

For this test two samples were generated: A $pp \rightarrow e^+e^-\mu^+\mu^-$ sample and a $pp \rightarrow e^+e^-\mu^+\mu^-(j)$ sample, the latter allowing for real emission. It is this sample that should be reweighted such that the full next-to-leading order corrections are present. The sample should then in principle be similar to the sample generated with MadGraph+MadLoop, thus this sample will be used for comparisons.

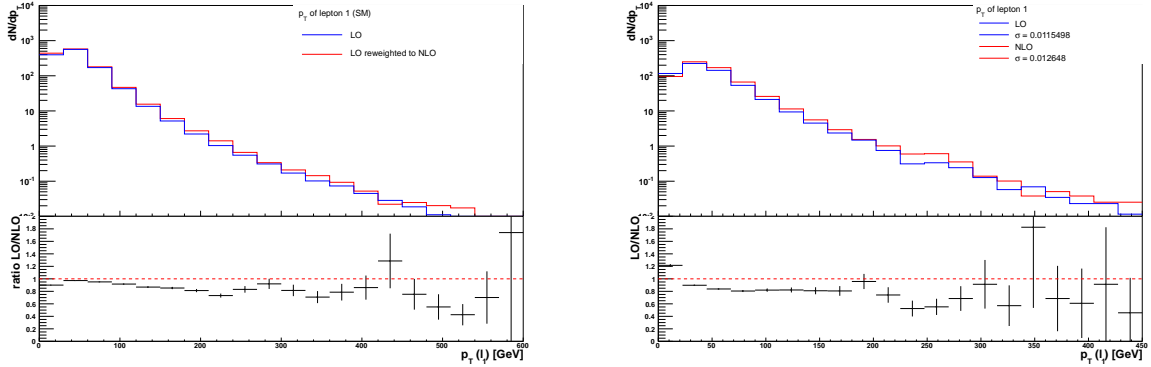


Figure 8.1: The left figure shows a comparison of the leading order $pp \rightarrow e^+e^-\mu^+\mu^-$ sample to the sample $pp \rightarrow e^+e^-\mu^+\mu^-j$ reweighted to include next-to-leading order corrections. The right figure shows the same comparison performed in MadGraph+MadLoop. The dashed red line indicates a ratio of one and the distribution show the p_T of the electron.

Shown in Fig. 8.1 are the p_T distributions of the electron at next-to-leading order obtained with the reweighting method and MadGraph+MadLoop. Both contain the real and virtual corrections and should thus be directly comparable. A χ^2 and Kolmogorov-Smirnov test was performed on the ratio, resulting in Fig. 8.2.

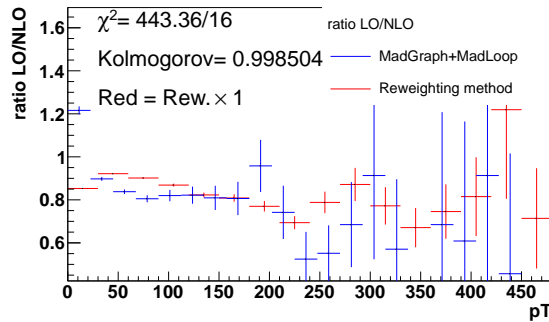


Figure 8.2: The comparison of the two ratios (LO/NLO) and (SM/Reweighted) obtained from MadGraph+MadLoop and the reweighting method.

Shape-wise they are compatible with a Kolmogorov-Smirnov probability of 99%. The χ^2 fit gives high values because of discrepancy between generators in the first bin. Here it seems that MadGraph+MadLoop estimates the leading order contribution to be bigger than the next-to-leading order, while SHERPA does not have the same effect. The decrease in events at low p_T is primarily due to real emission, and the method used in MadGraph+MadLoop seem to disagree with the method used in SHERPA.

A χ^2 test was performed, showing minimal χ^2 without scaling. If one excludes the first bin, there is a minima at a scaling factor of 0.956. This is similar to the correction

factor when comparing to MCFM, but only this is a downwards scaling. Thus it seems that the reweighting method overestimates the virtual corrections compared to MCFM, while underestimates the corrections compared to MadGraph+MadLoop.

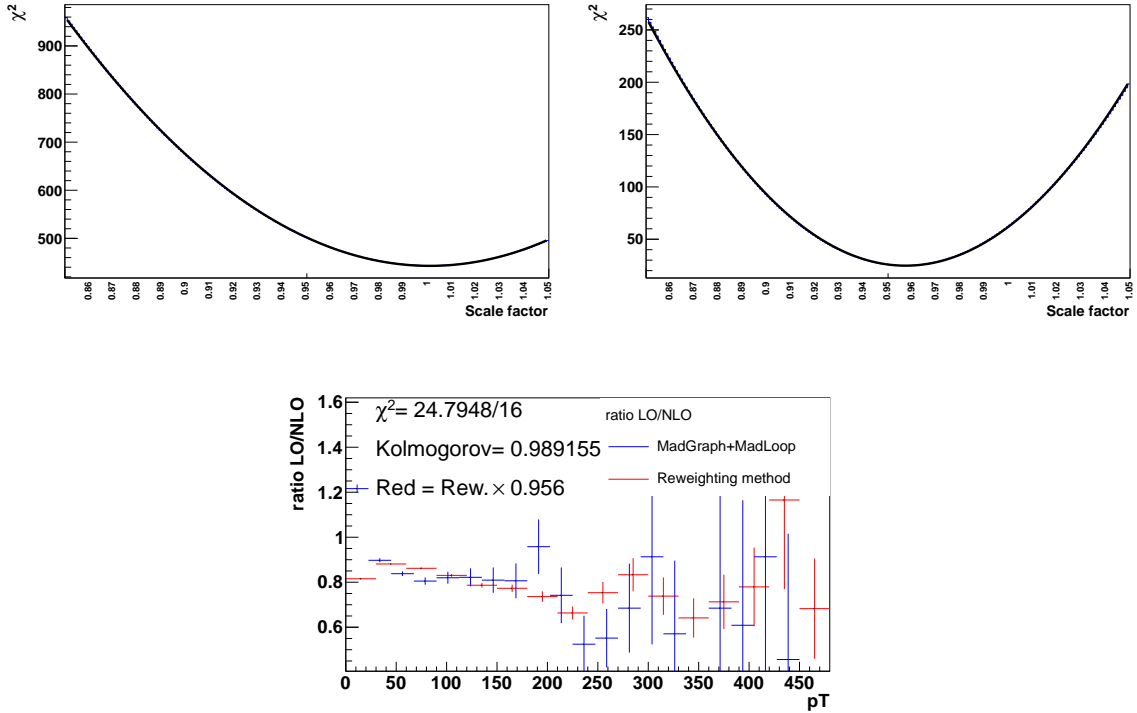


Figure 8.3: The χ^2 obtained when scaling the reweighted sample in steps of 0.001. The upper left figure includes the first bin in the fit, the upper right does not. The bottom figure shows the distribution when applying the scaling factor of 4.4%.

The uncertainty due to scale choice is estimated by varying the factorisation and renormalisation scale. The cross sections obtained by integration are given in Table 8.2 and results in an uncertainty of 5.1%. The uncertainty due to PDF choice is estimated not to change, since the choice of PDF has not changed.

$\mu_F = \mu_R =$	σ (fb)	Error (fb)
M_{VV}	12.73	0.019
$0.5 \cdot M_{VV}$	13.87	0.16
$2 \cdot M_{VV}$	12.58	0.18

Table 8.2: The cross sections obtained with the reweighting method when varying the factorisation and renormalisation scales.

This results in a cross section of:

$$\begin{aligned} \sigma_{NLO}^{rew.} &= 12.73 \pm 0.019(\text{stat}) \pm 0.65(\text{scale}) \pm 0.49(\text{PDF}) \text{ fb} \\ &= 12.73 \pm 0.81 \text{ fb} \end{aligned}$$

giving an increase of 12.4% compared to the leading order sample.

8.2 Reweighting the $f_5^Z = -0.25$ sample to the Standard Model

The sample (3) from Table 8.1 on page 83 is reweighted to the Standard Model with the three generators BHO, BR and GoSam. It is expected that the BR and BHO will perform worse than the GoSam generator, since these do not include all possible diagrams present in the sample. Hence a reduced χ^2 worse than obtained in the on-shell case is expected. The GoSam generator includes all possible diagrams present in the sample. This should provide a more precise reweighting, and it is thus expected that the generator will obtain a reduced χ^2 comparable to the one obtained in the on-shell sample.

It is evident that the two on-shell generators suffers, especially in the high p_T tail. The reduced χ^2 is now of the order of 2, giving a much worse compatibility compared to the on-shell sample. If one reduces the single resonant contribution by introducing cuts to the sample, the generators BR and BHO are expected to obtain improved reweighting samples. The cuts are loosened compared to what suggested in Sec. 7.2, since these were found to be too tight. The cuts applied to the sample are given in Table 8.3 on the facing page.

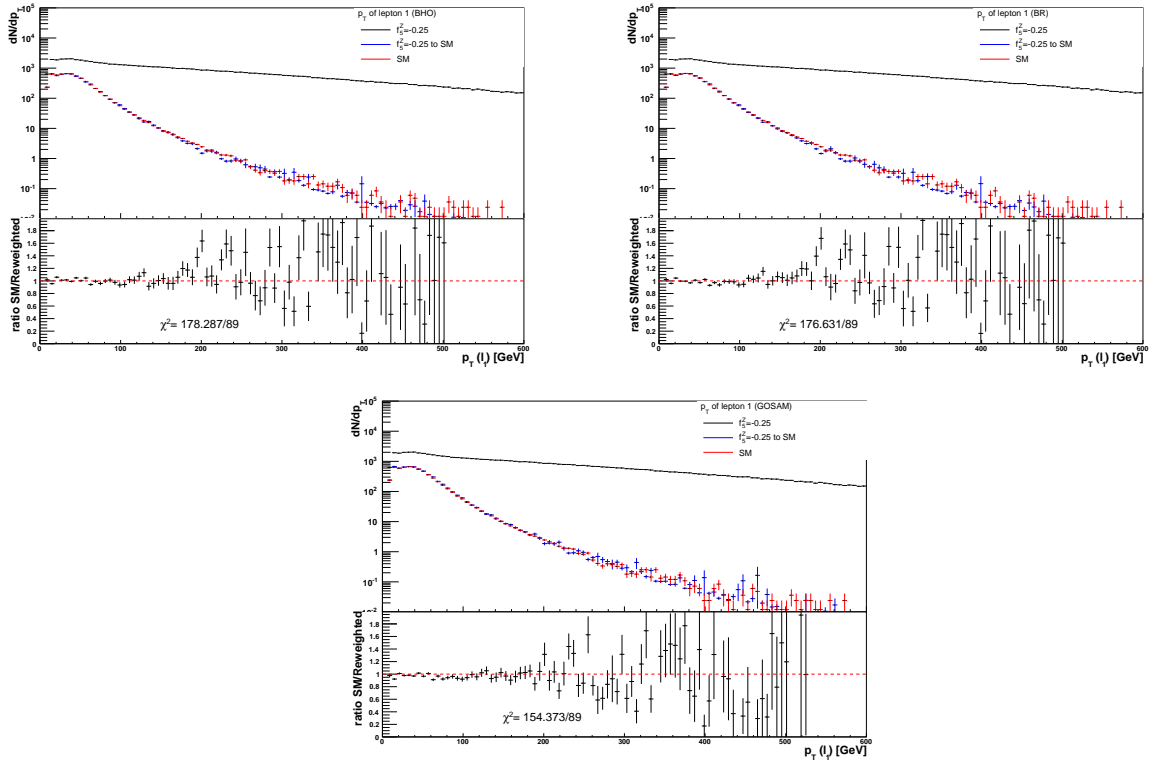


Figure 8.4: A BSM sample generated with SHERPA with the anomalous coupling $f_5^Z = -0.25$ is reweighted down to the Standard Model value of $f_5^Z = 0$ with the two generators BHO (left), BR (right) and GoSam (bottom) compared to the Standard Model sample. The dashed red line indicates a ratio of one and the distribution show the p_T of the electron.

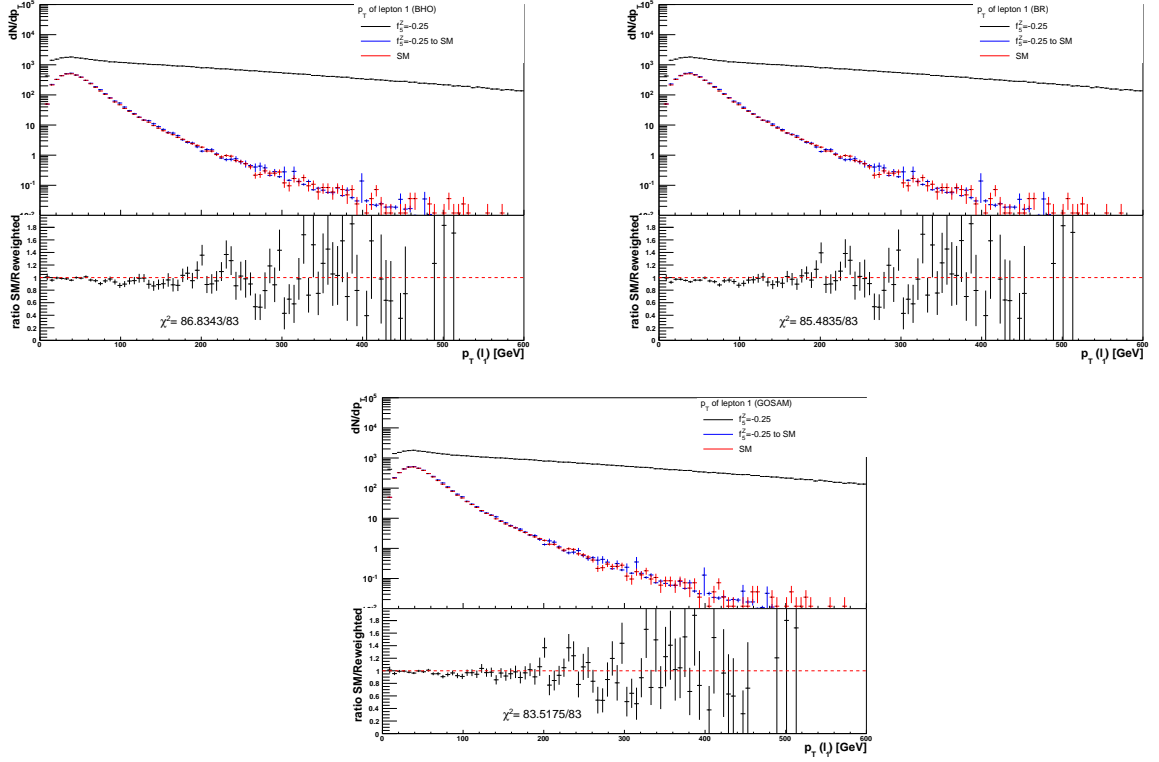


Figure 8.5: A BSM sample generated with SHERPA with the anomalous coupling $f_5^Z = -0.25$ is reweighted down to the Standard Model value of $f_5^Z = 0$ with the three generators BHO (upper left), BR (upper right) and GoSam (bottom) and compared to the Standard Model sample after the selection cuts given in Table 8.3. The dashed red line indicates a ratio of one. The distribution show the p_T of the electron.

Observable	Cut
M_{ZZ}	150 GeV
M_Z	[66, 116] GeV
$p_T(l)$	> 10 GeV
$ \Delta R(l, l) $	> 0.2

Table 8.3: The reweighting cuts

Applying the cuts seem to benefit all three generators, now all being comparable with a reduced χ^2 equal to one. It seems that it is actually the Standard Model sample having the highest fluctuations in the high p_T tail because of the low statistics.

All three generators also give comparable results in the $\cos\theta$ distribution, with GoSam performing slightly better. The additional diagrams implemented in the GoSam matrix element gives slightly better results without cuts, approximately 15% improvement in the reduced χ^2 . After the selection cuts the three generators are comparable and perform equally well.

8.3 The TGC samples at next-to-leading order

In this section the next-to-leading order effects in the $pp \rightarrow e^+e^-\mu^+\mu^-$ channel is analysed with BSM effects taken into account via the coupling f_5^Z . This coupling interferes with the

Standard and effects are expected to be seen in the high p_T tail. The section begins by analysing the real emission effects and ends with the inclusion of the virtual corrections.

The study of the virtual corrections in the neutral TGC sector is the first of its kind. This effectively means there are no ways of comparing the results of the virtual corrections, thus no statistical tests can be performed against other generators. Since the matrix element has been validated both at Standard Model values (Sec. 8.1) and beyond (Sec. 8.2) the assumption is, that the next-to-leading order corrections to the TGC samples are correct within the 4.4% uncertainty found when comparing against MadGraph+MadLoop. A smaller study is dedicated to the effects in the TGC sample (4) with the couplings being connected by requiring the $SU(2)$ invariance.

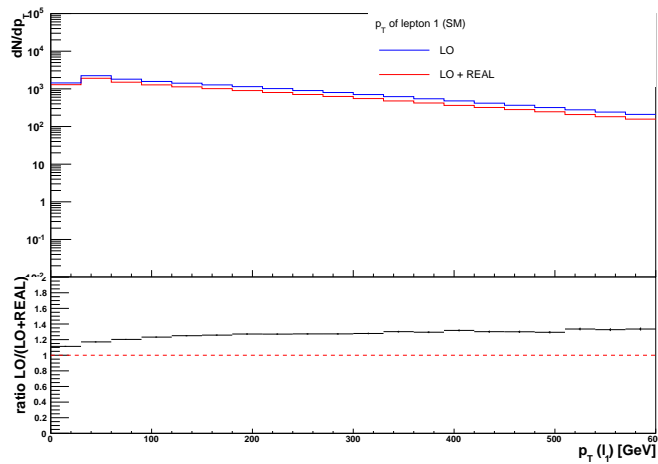


Figure 8.6: The distribution show the p_T of the electron in the leading order sample (blue) and in the real emission sample (red) both with TGC coupling $f_5^Z = -0.25$. The dashed red line indicates a ratio of one.

The inclusion of the real emission gives rise to an overall reduction in events compared to the leading order sample. The same effects were seen in Sec. 7.3, but are greater in this sample, because of the increased number of allowed real emission diagrams. The decrease in cross section is found to be $\sim 25\%$, and the ratio $(LO/(LO+REAL))$ is greater than one in the entire spectrum. In Sec. 8.1 the increase in the cross section was found to be 12.4% when including all next-to-leading order corrections. The same will not be the case in this study, since the real emission effects decrease the cross section significantly. A total increase in the cross section compared to the leading order sample will require the virtual corrections to be larger than 25% and this is highly unlikely.

Because of this general decrease in cross section, the virtual corrections will be compared to the sample with real emission, and not the leading order sample. This will also directly allow for seeing the effects of the full next-to-leading order corrections compared to only including the real emission effects in the TGC samples.

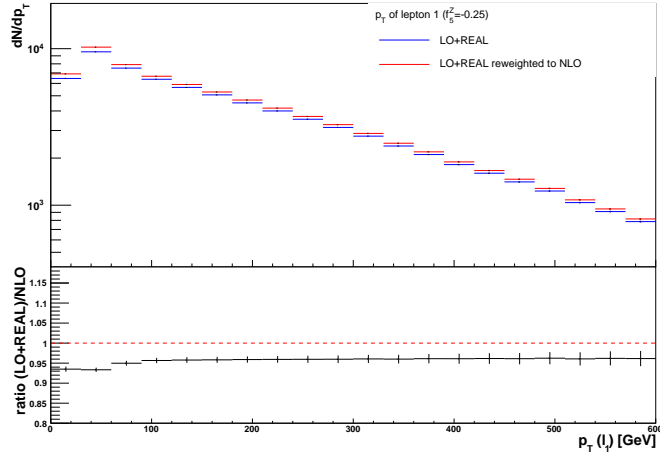


Figure 8.7: The distribution show the p_T of the electron in the real emission sample (blue) and in the reweighted sample (red) with a nonzero value of f_5^Z coupling and the dashed red line indicates a ratio of one.

The sample has been generated with a dynamic factorisation and renormalisation scale, and the effects of the virtual contributions are seen to become constant with increasing p_T . This is similar to what found in Sec. 7.6, when the dynamic scale was introduced. The low p_T effects of the virtual corrections are still seen, the ratio $((\text{LO}+\text{REAL})/\text{NLO})$ is slightly higher at $p_T \sim 50$ GeV. Thus an overall increase in events is obtained when including full next-to-leading order effects in the TGC sample. But the K-factor from the virtual corrections only amounts to 1.05. Hence the K-factor when comparing the leading order sample to the full next-to-leading order sample will be ~ 0.8 , which is still a decrease but slightly less than when only including the real emission effects.

The significant decrease in the next-to-leading order corrections can be explained through diagram combinatorics. The on-shell study only included four diagrams in the leading order matrix element, while including ten diagrams in the virtual matrix element. The leading order matrix element in the off-shell study includes 31 leading order diagrams and 55 virtual diagrams. The ratio between the number of diagrams is thus reduced, and could explain the decrease in the effects of the virtual corrections. The same logic applies to the increase in the real emission effects, where the on-shell matrix element had 18 real emission diagrams giving a ratio of ~ 0.2 to the leading order diagrams. The off-shell matrix elements have an increased set of real emission diagrams, 70, resulting in a ratio of ~ 0.44 . Hence the real emission effects should be significantly larger in the off-shell sample, which is also seen in Fig. 8.6 on the preceding page¹.

The uncertainty due to scale choice gives 3.5%, resulting in a cross section of:

$$\begin{aligned}\sigma_{NLO}^{rew.} &= 16.05 \pm 0.02(\text{stat}) \pm 0.57(\text{scale}) \pm 0.49(\text{PDF}) \text{ fb} \\ &= 16.05 \pm 0.75 \text{ fb}\end{aligned}$$

giving a decrease with respect to the leading order sample of 18.7%.

¹This is of course only an estimate. One must remember to subtract the TGC diagrams, which do not contribute if the couplings are zero.

$\mu_F = \mu_R =$	σ (fb)	Error (fb)
M_{VV}	16.05	0.02
$0.5 \cdot M_{VV}$	16.36	0.02
$2 \cdot M_{VV}$	15.22	0.02

Table 8.4: The cross sections obtained with the reweighting method when varying the factorisation and renormalisation scales.

In Fig. 8.8 the gauge invariant connections between the couplings f_4, h_1^V have been used. The explicit structure of the connections were given in Sec. 3.2 as [16]:

$$h_1^Z = -\frac{\sin \theta_W}{\cos \theta_W} h_1^\gamma = -f_4^\gamma = \frac{\cos \theta_W}{\sin \theta_W} f_4^Z = M_Z^2 \frac{v^2}{4} f$$

with θ_W being the weak mixing angle and v the vacuum expectation value of the Higgs field. This allows for setting the gauge invariant structure in a SHERPA sample:

$$\begin{aligned} h_1^Z &= -0.25 \\ h_1^\gamma &= 0.13 \\ f_4^\gamma &= 0.25 \\ f_4^Z &= -0.47 \end{aligned}$$

where the relation $\cos \theta_W = \frac{M_W}{M_Z} = 0.88$ have been used. Due to time limitations only the real emission sample has been generated, and it is thus not possible to extract a K-factor with respect to the leading order sample.

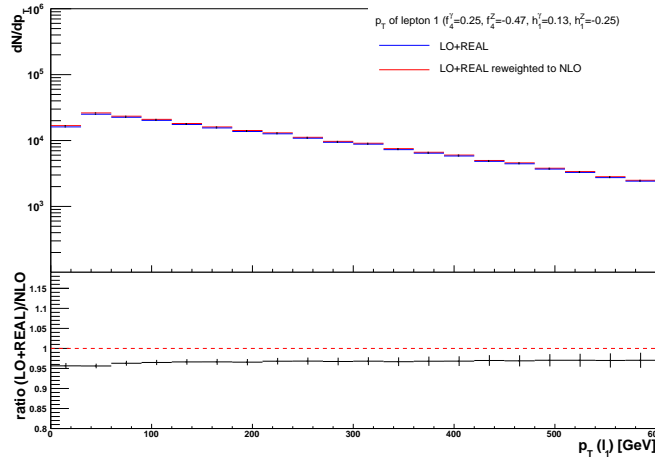


Figure 8.8: The distribution show the p_T of the electron in the real emission sample (blue) and in the reweighted sample (red). The reweighted sample now includes the full next-to-leading order contributions to the TGC sample (3) from Table 8.1. The dashed red line indicates a ratio of one.

Fig. 8.9 on the next page shows the same overall decrease in the virtual effects as found in the sample with one non-zero coupling. The additional decrease in the corrections supports the idea that the ratio between the number of diagrams in the leading order and the next-to-leading order matrix elements plays a role in how big a contribution the next-to-leading

order corrections will give. The K-factor obtained in this sample is so small, that the effects of the virtual corrections in principle are negligible.

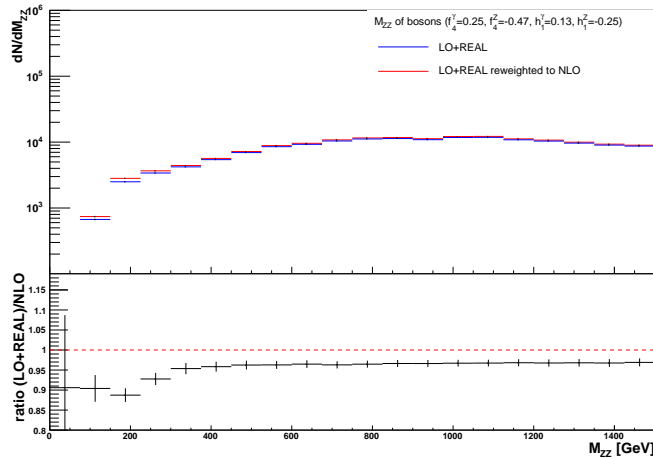


Figure 8.9: The distribution show the M_{VV} spectrum of the two bosons in the real emission sample (blue) and in the reweighted sample (red). The reweighted sample now includes the full next-to-leading order contributions to the TGC sample (3) from Table 8.1. The dashed red line indicates a ratio of one.

The effects are slightly better seen in the invariant mass distribution. Here the increase of events in the next-to-leading order sample is still visible at low M_{VV} . The effects in the other observables are negligible, being an overall scaling factor of ~ 1.05 . The scale uncertainty is again of 3.5%.

$\mu_F = \mu_R =$	σ (fb)	Error (fb)
M_{VV}	47.26	0.07
$0.5 \cdot M_{VV}$	48.12	0.007
$2 \cdot M_{VV}$	44.79	0.006

Table 8.5: The cross sections obtained with the reweighting method when varying the factorisation and renormalisation scales.

By introducing the cuts in Table 8.2 on page 85 the effects of the virtual corrections become more visible. The reduction of the single resonant background and the cross terms between the single and double resonant diagrams slightly increases the low M_{VV} effects. But the K-factor here is still only ~ 1.1 and thus not comparable to the real emission effects.

The study concludes with the observation that the virtual corrections to the TGC samples are negligible compared to the large real emission corrections. But the inclusion of the virtual corrections to the TGCs are primarily seen in the low p_T or low M_{VV} end, where one would not expect the effects of the TGCs to be present. The virtual effects in this part of the spectrum is likely to arise from the large Standard Model contribution, but a fraction of the events could be contributions from the TGCs and the virtual corrections to these diagrams.

Choosing to work with a matrix element that includes these effects is crucial, if one strives for precision measurements. The matrix element used in this thesis is $\sim 15\%$ better in reweighting samples without cuts. If the selection cuts are used, the generators are comparable, having reduced most of the single resonant and cross term contribution. In this case, the choice of generator can be based primarily on whether or not one would like to

include the virtual corrections to a sample. Since these effects amount to $\sim 10\%$ increase in cross section at low p_T and M_{VV} it could be necessary to use the full next-to-leading order matrix element for precision measurements.

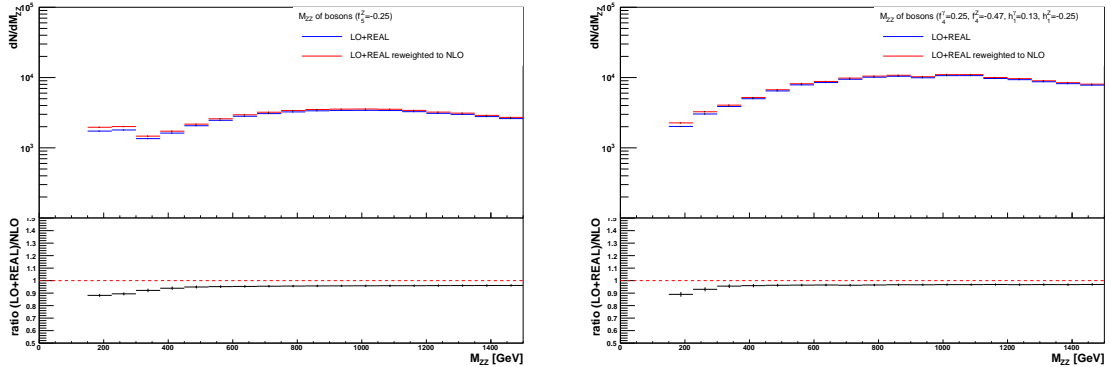


Figure 8.10: The distribution show the M_{VV} spectrum of the two bosons in the real emission sample (blue) and in the reweighted sample (red). The left figure shows the sample with only f_5^Z being non-zero, the right the TGC sample (3) from Table 8.1. The dashed red line indicates a ratio of one.

8.4 Discussion of the off-shell matrix element

The initial runs in all three above tests showed large numerical instabilities. The weights obtained with the off-shell matrix element contained instances of both infinities and nans. Examination of the events with these weights showed that all were events with one gluon in the initial state. Processing an entire sample at the same time gave rise to these instabilities, but if the author processed one event at the time these weights did not occur. It was then concluded that the matrix element worked, but that it was not properly initialised. Due to time limitations a temporary fix was introduced such that the code will initialise the amplitude calculation (up to ten times) until neither nan or inf are returned.

This is of course very unfortunate, since the generator was supposed to be a good alternative to the BR and BHO generators. But the real emission processes seem to be too big (70 diagrams with 128 helicity configurations) for GoSam to always handle properly. One can then either chose to use the on-shell matrix element for the real emission processes, or simply to use only the 'good' event weights.

The initial test showed that 2% of the real emission events failed. After the fix, this was reduced to 0.05%.

Conclusion and outlook

The results obtained in this thesis are the first full next-to-leading order corrections to the process $pp \rightarrow ZZ \rightarrow e^+e^-\mu^+\mu^-$ with anomalous couplings f_4^V, f_5^V . The results show an overall decrease in cross section when the next-to-leading order corrections are taken into account. Most of this absorption is due to the real emission in the process, and thus by introducing the additional virtual corrections, the decrease is reduced. The virtual corrections in the neutral TGC sector gives rise to a p_T dependent K-factor varying from ~ 1.1 at low p_T or M_{VV} to ~ 1.05 at high p_T or M_{VV} . Compared to the real emission corrections these virtual effects are thus negligible.

The method used to include these next-to-leading order corrections is based on the reweighting method, a method highly efficient for both Monte Carlo studies and data samples. The method has been used in ATLAS when limits are set on the anomalous couplings, see eg. [15], and the full next-to-leading order matrix element would be an improvement in this sector. Other collaborations are also pursuing the reweighting method, an example is the inclusion of MadWeight into the MadGraph generator [44].

The use of the GoSam generator in the developed generic algorithm for matrix element reweighting provides an efficient and reliable way of including the next-to-leading order corrections to the reweighting method. The GoSam generator has been thoroughly validated for the Standard Model, hence results obtained with the generic reweighting algorithm in Standard Model processes are to be trusted completely. The inclusion of BSM models to GoSam relies on the user validating the model, before final results should be discussed. The model used in this thesis has been validated at both Standard Model and beyond. The validation has been done against the generators BR and BHO for the BSM part of the model, while the loop corrections have been validated at Standard Model against MCFM and MadLoop. No method of validating the BSM loop corrections exists, as no other generator includes the neutral TGC couplings at next-to-leading order (as far as the author knows). It would of course have been preferable if a method existed, but unfortunately the pursuits of implementing the model to MadGraph+MadLoop via FeynRules could not be done at present time. The interfaces of GoSam to SHERPA and MadGraph are still largely under development, and the efforts to include the model and obtain results using these, are still a work in progress.

A full simulation of the TGC process at next-to-leading order would thus be an excellent starting point for further studies. The GoSam collaboration is developing the interfaces fast, and a beta version of the interface to MadGraph should soon become public. The interface to SHERPA is, more or less, working at present time, but it has not been possible for the author to obtain results in the process under consideration. It should be noted that the effort to obtain these results were undertaken the last month of writing, hence a full understanding of what the errors arose from has not been obtained. Thus the interface might prove to be

perfectly working and thus it can only be the author who is to blame for the lack of results. Further studies would of course include the full understanding of the errors obtained in the SHERPA-GoSam interface, such that the Standard Model loop corrections obtained with the reweighting method can be compared against SHERPA as well. Bypassing the fact that the interfaces only allow for Standard Model processes has been fairly easy, hence if further knowledge of the SHERPA-GoSam interface was obtained, the corrections to the BSM model should be easy to get.

Other small issues with the use of GoSam occurred during the writing of this thesis. One noticeable issue was the creation and compiling times for the processes. This is due to the complicated expressions in the model, and the lack of hard coding the model in the language of FORM. Had the author known at the beginning of the studies, that the expressions obtained with the BSM model would slow the creation and compiling as much as it did, she would have made an effort to write the additional vertices in FORM. It is expected that the hard-coding of the vertices greatly decreases the creation time as well as it is assumed to make the compiler work both faster and without consuming as much memory. If this notion proves to be wrong, one can only hope that the efforts in handling bigger processes performed by the GoSam Collaboration will soon become public.

In conclusion the thesis has developed a method for reweighting any process of interest at next-to-leading order. It has been thoroughly validated at next-to-leading order in the neutral diboson sector of the Standard Model, and are comparable to both MCFM and MadGraph+MadLoop, showing a correction factor of 4.4% to each of the generators. This is an acceptable correction factor, as the uncertainty due to scale choice amounts to 3–7% depending on the process and chosen parameters. The generators MCFM and MadGraph+MadLoop gives scale uncertainties of $\sim 3\%$ hence the reweighting method is comparable.

At leading order the matrix element and the reweighting method has been validated by comparing to the generators BR and BHO. The TGC matrix element implemented in this thesis proved to be equal to the two generators, and the reweighted samples showed a good reduced χ^2 when compared to the Standard Model. In the inclusive $2e2\mu$ samples the implemented matrix element performed $\sim 15\%$ better than the BR and BHO generators, but after placing selection cuts on the sample to reduce the single resonant background, the three generators performed equally well.

The algorithm developed in this thesis provides a fast method of including virtual corrections to a Monte Carlo sample. The virtual corrections correspond to those obtained with MCFM and MadGraph+MadLoop. It is thus a reliable way of including next-to-leading order corrections to a leading order Monte Carlo simulation and could be, with a small development, used as a discriminator in data samples.

Acknowledgment

I would like to thank all the people who have aided me during this last year and made this work possible. Special thanks to

The Discovery center and especially the HEP group at the Niels Bohr Institute

For education, facilities and an excellent work environment. A special thanks goes to my office mates, who were always ready to listen when I had compiler issues, and never complained when I crashed the computers.

Gavin Cullen

For numerous answers to GoSam questions and BSM models, for great patience and for testing the TGC model in the GoSam beta version.

Kristian Gregersen

For physics discussions, debugging models, providing scripts and inspiration.

The GoSam, SHERPA, MadGraph and FeynRules Collaborations

For aid and support when testing the beta versions of the programs.

Sofie Birch Jensen, Morten Medici, Jeppe Trøst Nielsen and Kamilla Nørregaard

For spell checks, physics discussions and endless coffeebreaks during long code-compilations.

Jørgen Beck Hansen

Last, but not least, for excellent guidance and endless inspiration. For letting me do a phenomenological thesis in an experimental group, and giving me freedom to explore the aspects of particle physics and physics simulation I always wanted. For being at work, when I arrive at seven in the morning and always having time for a discussion. It has been a great pleasure and privilege.

Appendices

Validation of the GoSam matrix element

The remaining figures showing the validity of the weights obtained with the GoSam matrix element.

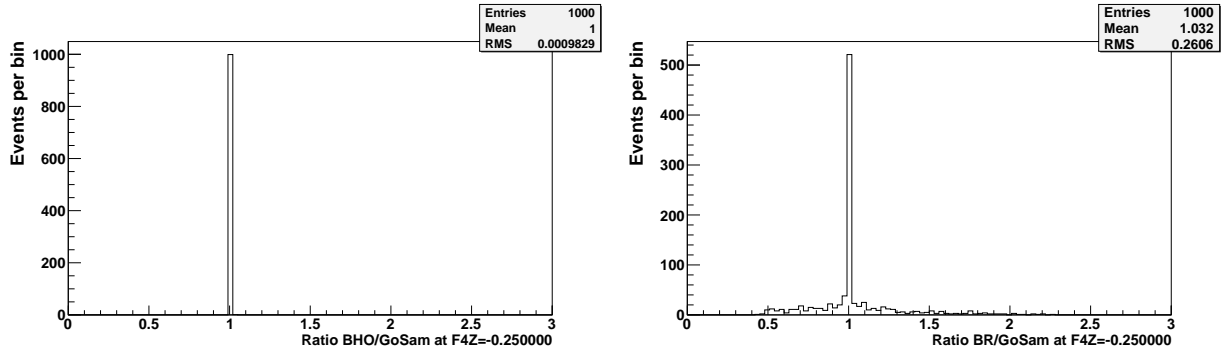


Figure A.1: Matrix element comparison between GoSam and BR generators in a $pp \rightarrow ZZ \rightarrow e^+e^-\mu^+\mu^-$ sample including the coupling $f_4^Z = 0.25$ diagram in the matrix element.

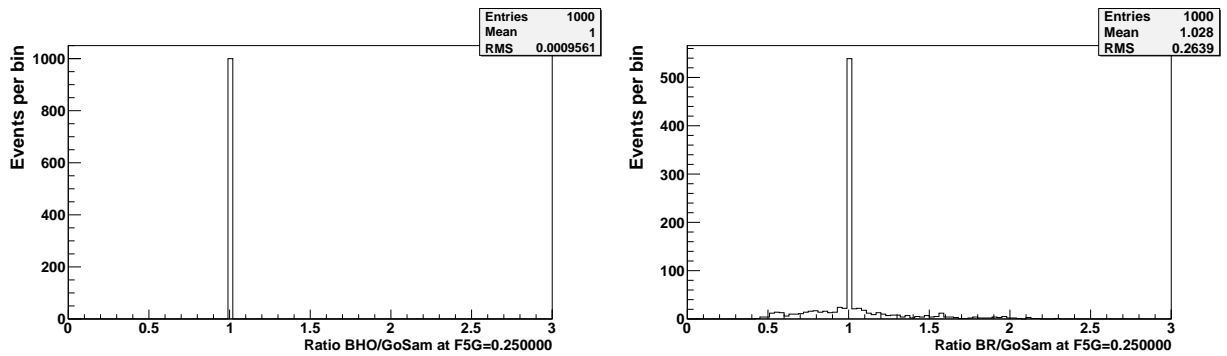


Figure A.2: Matrix element comparison between GoSam and BR generators in a $pp \rightarrow ZZ \rightarrow e^+e^-\mu^+\mu^-$ sample including the coupling $f_5^\gamma = 0.25$ diagram in the matrix element.

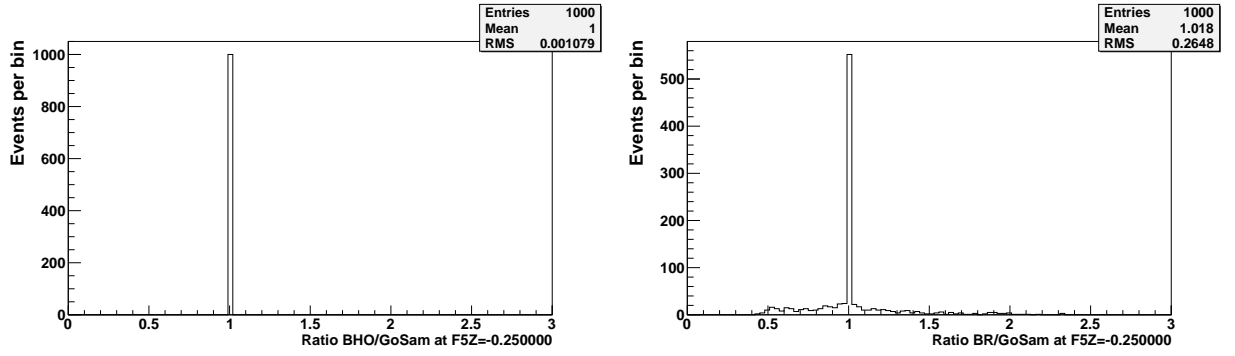


Figure A.3: Matrix element comparison between GoSam and BR generators in a $pp \rightarrow ZZ \rightarrow e^+e^-\mu^+\mu^-$ sample including the coupling $f_5^Z = 0.25$ diagram in the matrix element.

Technical information of the reweighting algorithm

B.1 Prerequisites

- Python v. 2.6 or higher
- Java v. 1.5 or higher
- QGraf: <http://cif.ist.utl.pt/~paulo/qgraf.html>
- FORM v. 3.3 or higher: <http://www.nikhef.nl/~form/>
- The Gosam Contrib Suite v. 1.0 or higher: <http://www.hepforge.org/archive/GoSam/GoSam-contrib-1.0.tar.gz>
- The GoSam Package v. 1.0-175 or higher: <http://www.hepforge.org/archive/GoSam/GoSam-1.0.tar.gz>
- The LHAPDF package: <http://projects.hepforge.org/lhapdf/>
- The compilers *gfortran* and *gcc*

B.2 Source codes

Interface:

- `Weight.cxx` - C++ binding
- `Weight.h` - C++ binding header files
- `lhpdf/lhapdf-5.8.9.tar.gz` - Library for PDF's
- `GoSam/Makefile`, `GoSam/module.sh`, `GoSam/interface.sh`, `GoSam/convertchar.sh`
The generic matrix element generator interface

Test program:

- `DiBosonStudy.cxx` - Main test program using the C++ binding
- `DiBosonClass.cxx` - Class for diboson study
- `DiBosonClass.h` - Header files for diboson study

- SherpaEvent.cxx - Class for events generated by Sherpa MC
- SherpaEvent.h - Header for Sherpa class
- MadGraphEvent.cxx - Class for events generated by MadGraph
- MadGraphEvent.h - Header for MadGraph class
- dble/bhowei.f, dble/brwei.f, dble/dibwei.f, dble/weiholib.f
Two other matrix element generators for example diboson studies
- Makefile

Interface description of the reweighting algorithm

The interface code can be used as a stand-alone Fortran90 subroutine, where the calling sequence is

```
call getxsec(nparticles, pdg, vecs, scale2, amp, irp)
```

where

nparticles (input, integer) is the number of particles in the process (maximum 8),

pdg (input, integer, dimension(nparticles)) is the PDG MC code for each particle in the event,

vecs (input, real, dimension(nparticles, 0:3)) is a two dimensional array of the momenta of each particle in the event¹,

scale2 (input, real) is the renormalisation scale squared, μ^2 , to which the next-to-leading order corrections are evaluated,

amp (output, real, dimension(0:3)) is an array of four containing the Born amplitude squared (**amp**[0]), the interference terms with the Born amplitude containing the finite (**amp**[1]), ε^{-1} (**amp**[2]) and ε^{-2} (**amp**[3]) parts of the one loop amplitude,

irp (output, real, dimension(2:3)) containing the single (**irp**[2]) and double (**irp**[3]) pole remaining after correct UV renormalisation. These singularities should be equal to the ε^{-1} (**amp**[2]) and ε^{-2} (**amp**[3]) parts of the one loop amplitude, and can thus be used as a check of the amplitude result.

The setup starts with scanning the working directory for files with a `.tar.gz` suffix. A directory is created with names corresponding to the process name, ie. from `process1.tar.gz` a directory with the name `process1` will be created. Each tar ball is then unpacked into its corresponding directory and the Makefile provided in the tarball will be used for compilation of the source codes in each directory. After succesful compilation² a shared library is created

¹The Fortran90 interface requires the momentum array to be of the following form: $\text{vecs}(i, 0) = E_i$, $\text{vecs}(i, 1) = p_i^x$, $\text{vecs}(i, 2) = p_i^y$, $\text{vecs}(i, 3) = p_i^z$

²The compilation of the GoSam source code can be quite memory consuming. For a detailed description with solutions to possible compiling issues, see Sec. 5.4

containing all information available in the source codes. This library is then moved to a newly created directory `lib` and the shell script `module.sh` is invoked.

This script creates a Fortran90 module for each process available in the working directory. It creates the following subroutines: `processname_setparameters`, `processname_amplitude` and `processname_processID`. The first subroutine makes the user able to change the default values of all variables in the process and takes as input a character array. The second calls the calculation of the amplitude with proper initialisation of all schemes needed for the next-to-leading order amplitude calculation. It also contains a call to the infrared subtraction calculation. The subroutine takes as input the number of particles in the process (integer), an array of momenta of each particle in the process (real) and a scale to which the next-to-leading order calculation is carried out (real). The output is an array of four amplitudes (real) and an array of two infrared singularities (real). The last subroutine takes as input the number of particles in the input file and gives back an array (integer) of the particle codes in a format readable by the interface.

After the creation of the process modules the setup continues to writing the interface. It uses the newly created modules and contains two subroutines: `findparameter` and `getxsec`. The `findparameter` subroutine takes three inputs, an array (character) containing the variable name one wishes to set, a size of the character array (integer), and the value one wishes to set the variable to (real). It then automatically edits the incoming information into a format readable by the `processname_setparameter` subroutine which it afterwards calls to set the variable properly. The `getxsec` subroutine in- and output are described above. The subroutine starts out by calling the `processID` subroutine from each process available and storing the output array into a two dimensional array containing the assigned process number and the particle codes in the given process number. It then takes the input particle codes and converts it into the same format as used by the `processID` subroutine and does a scan of the particle codes from the input and compares them to the particle codes coming from the `processID` subroutine. If the codes match the interface knows which process module to call for amplitude calculation. If the particle codes does not match, the subroutine tries to swap the particle codes from the input such that it matches the particle codes from the `processID` subroutines. If a match is not found a warning message is printed to screen, and the amplitude returned is zero.

This completes the description of the Fortran90 source codes. The Makefile does not include a recipe on how to compile each of the created Fortran90 source codes, since this is done by the C++ binding. If one does not wish to use this binding a recipe is given below:

```
F90OBS=process1.o process2.o ... processN.o

BUILDDIR=build

FC=gfortran

GoSamInterface.o: GoSamInterface.f90
    echo "Compiling $< "
    $(FC) -I${PWD}/${BUILDDIR} -c GoSam/$< -o $(BUILDDIR)/$@

GoSamInterface.f90: $(F90OBS)
    cd GoSam ; make $@;

$(F90OBS): %.o: %.f90
    echo "Compiling $<"
```

```
$(FC) -I${PWD}/GoSam/$(basename $@)/common  
-I${PWD}/GoSam/$(basename $@)/matrix -c GoSam/$<  
-o $(BUILDDIR)/$@
```

```
%.f90: GoSam/Makefile #: $(error Error! Need to rebuild $@ by doing:  
'( cd GoSam; make $@ )')  
cd GoSam; make $@;
```

Here the interface working directory is called GoSam, and all object files are moved to a build directory. Remember also to link the shared libraries in the directory lib in the working directory to your own executable when creating this.

C++ binding description

The C++ binding contains all relevant functions and routines for using the GoSam package for reweighting events. It consists of two files, `Weight.cxx` and `Weight.h`, where the latter is a header file with declarations of all routines in the `.cxx` file as well as the C++ call to the GoSam Fortran90 routines and the LHAPDF Fortran77 routines. The `.cxx` files contains the following routines:

`PrintParameters()`: Prints the parameters needed by the program.

`SetParameter(const char* parameter, double* value)`: Allows the user to set a value to the parameters needed by the program.

`SetCharParameter(const char* parameter, const char* name)`: Allows the user to set a character name to the parameters needed by the program.

`InitPDF()`: Initialises the LHAPDF set chosen.

`GetNumberOfParticles(const vector<int> pdg)`: Returns the number of particles in the process (max. 8) by returning the array number of the first empty PDG code.

`AlphaS_loop(const double* Q2, const double* Lambda4, const double* mtop, const double* order)`: Returns the 1-, 2- or 3-loop value of α_S . Input values are the energy scale, Q2, the QCD λ_4 for the initialised PDF set, the top mass and the order (1,2,3).

`gS(const double* alphas)`: Returns the value of the strong coupling. Input value is α_S calculated from the above `AlphaS_loop`.

`gE(const double* alpha)`: Returns the value of the electromagnetic coupling. Input value is the fine-structure constant.

`OneLoop(const double* alphasloop, const double* varepsilon)`: Returns the 1-loop factor of $\frac{\alpha_S(\mu)}{2\pi} \frac{(4\pi)^\epsilon}{\Gamma(1-\epsilon)}$ excluded from the GoSam amplitude. Input is α_S and ϵ .

`Q2(const int* iscale)`: Returns the scale to which the PDFs and the virtual corrections are evaluated. Input is the wanted scale, `iscale`=1-6, where 1 will return s , 2 will return $Q = M_{VV}^2$, 3 will return the p_T scale of the incoming quarks, 4 will return $Q = M_W^2$, 5 will return $Q = M^2$ where M can be whatever mass scale needed, and finally 6 will return

$$Q = M_Z^2.$$

`Formfactors(const bool qcd, const int* ndecay, const double* borncoupling, const double* couplingpower)`: Returns the multiplication factors missing from the GoSam amplitude. Input are the boolean (process specific): `qcd/!qcd(=ew)`, the number of particles in the events, the Born coupling of the process (`gE`, `gS`) and the power of the Born coupling (eg. 2 if the Born coupling is e^2).

`Lambda(const double a, const double b, const double c)`: Returns the two body phase-space lambda factor.

`TwoBodyPS(const double* mVV2, const double* mV12, const double* mV22, const double* s)`: Returns the two body phase-space function. Input are the squared invariant masses of the two bosons, `mVV2`, of the first boson, `mV12`, and the second boson, `mV22`, and finally the s of the system.

`ThreeBodyPS(const double* mVV2, const double* mV12, const double* mV22, const double* s)`: Returns the three body phase-space function. Input the same as the above.

`BornCoupling(const string coupling)`: Returns the correct value of the Born coupling from the string name. Eg. `weak` will return `gE`, `strong` will return `gS`.

`GetXsec(const vector<int> pdg, const vector<double> momenta, const double* scale, const bool nlo)`: Returns the differential cross section for the event. Input values are the PDG codes and momenta of the particles, the renormalisation scale, μ_R , and the boolean makes `GetXsec` return either the Born amplitude (`!nlo`) or the next-to-leading order amplitude (`nlo`).

Aside from these functions the `.cxx` file contains structured type (`struct`) containing the parameters needed by the program. The C++ binding can be used to interface the GoSam Fortran90 interface to the users own code. It can be included to any C++ program with

```
#include "Weight.h";
```

and a successive setup

```
Weight somename;
```

in the main program. From here on the class members can be called by eg.

```
somename.InitPDF();.
```

The parameters needed by the program are:

- `pi` (`double`) - the mathematical constant.
- `epsilon` (`double`) - the regulator in the dimensional regularisation scheme.
- `alpha` (`double`) - the fine-structure constant.
- `qcd` (`bool`) - true if QCD corrections, false if EW corrections.
- `borncoupling` (`string`) - type of born coupling: weak or strong.

- `powerborn` (`double`) - power of born coupling in \mathcal{M} .
- `pdfsubset` (`int`) - number of LHAPDF subset: Default 0.
- `pdfname` (`string`) - name of LHAPDF set.
- `iscale` (`int`) - integer to specify scale to evaluate α_S and the PDFs.
- `looporder` (`int`) - order of the α_S calculation (1,2,3).
- `cq` (`double`) - multiplication factor for the scale calculation: Default 1.
- `mscale` (`double`) - if `iscale=5` this scale must be set to evaluate Q . Can be whatever mass scale (in GeV).
- `ecm` (`double`) - center of mass energy of the beams.
- `mw` (`double`) - mass of the W-boson.
- `mz` (`double`) - mass of the Z-boson.
- `mt` (`double`) - mass of the top quark.
- `mb` (`double`) - mass of the b-quark.
- `pT` (`double`) - if `iscale=3` this scale must be set to evaluate Q .
- `mM1` (`double`) - mass of the first (mother) particle.
- `mM2` (`double`) - mass of the second (mother) particle.
- `mM3` (`double`) - mass of the third (mother) particle.
- `mM1M2` (`double`) - invariant mass of the first and second (mother) particles.
- `mM1M3` (`double`) - invariant mass of the first and the third (mother) particles.
- `mM2M3` (`double`) - invariant mass of the second and third (mother) particles.
- `sqrts` (`double`) - \hat{s} of the incoming partons.
- `reduction_interoperation` (`int`) - choice of integral library used for integral reduction. Choices are 0 (Samurai), 1 (Golem95), 2 (Samurai, Golem95 if Samurai fails), 4 (tensor reconstruction with Golem95, integral reduction with Samurai), 5 (tensor reconstruction with Golem95, integral reduction with Samurai, Golem95 if Samurai fails)

D.1 Creating the GoSam tarballs

Assuming a successful installation of the GoSam package, the user must now generate the source codes in Gosam for the process he or she wishes to analyse. A short how-to is available here, complete information can be found in [38].

The user edits the template process card generated by typing

```
$gosam.py -template
```

Besides specifying the incoming and outgoing particles, the order of the process, eg. $g_\alpha = 4$, excluding unwanted diagrams etc., **it is important** that the user sets the masses of all light quarks to zero and that the strong coupling and the electromagnetic coupling is set to one. This is because the interface itself sets the scale at which these couplings are evaluated, eg. $\alpha_S(M_Z)$. Once the process card is edited the user types

```
$gosam.py -v nameofprocesscard.in
```

GoSam will generate then the source codes. After generation of the source codes it is important to type

```
$make doc
```

to generate a .ps file with the helicity configurations and selected diagrams. This is only used for double checking that the diagrams are actually the ones the user wants. If the diagrams are correct the user types

```
$make dist
```

GoSam then creates a tar ball with all source codes needed for generating the matrix element. Once created the user must move the tar ball to the location of the interface subdirectory GoSam

```
$cp processname.tar.gz /location/of/interface/GoSam/.
```

Here the user can decide to implement the interface to his or her own code, or follow the directions below, if the test-program is used.

D.1.1 GoSam installation issues

In the package provided by the GoSam collaboration, the filter module does not work. In the newest version they have added some lines to the filter module, that needs to be removed before the filter can operate. The lines are

```
$if r1[0:4] == 'part':  
    r1='%s' % r1
```

The lines are located in the `/src/python/golem/topology/objects.py` file. This is essential for proper selection of diagrams, but not for source code generation etc. The GoSam collaboration has been informed of the bug.

D.2 Test program manual

Once the tar balls from GoSam are in the subdirectory GoSam, change directory to the DiBosonStudy working directory. Here the user must type

```
$make DiBosonStudy
```

This will unpack the GoSam tar balls, compile the GoSam Fortran90 source codes, setup the Fortran90 interface to GoSam, compile the Fortran90 interface source codes, compile the additional matrix element source codes and the C++ binding, in the end making available the executable DiBosonStudy.

DiBosonStudy takes as input choice of matrix element generator, the case one wishes to study, the ROOT input ntuple, the ROOT output ntuple and (optional) the number of events for reweighting. It then calculates the next-to-leading order corrections to the leading order amplitude and saves the event weight as a branch in the tree created in the output file.

The calculation is done in one of three matrix element generators: the BHO generator (next-to-leading order), the BR generator (leading order) or the GoSam generator (next-to-leading order), the default being the last. The first two are designed for reweighting diboson events and has been used for cross checks of the amplitude generated by GoSam. If one chooses to use one of the two first additional information must be given to the executable in form of the anomalous couplings. If one wishes to use the GoSam matrix element generator for diboson events, these couplings must also be specified. They are required to be in the following format and order:

For the BHO matrix element	:
WW :	dg1z, dkz, lz, dkg, lg
WZ :	dg1z, dkz, lz
W γ :	dkg, lg
ZZ :	f4g, f4z, f5g, f5z
Z γ :	h1z, h2z, h3z, h4z, h1g, h2g, h3g, h4g
For the BR matrix element	:
ZZ :	f4g, f4z, f5g, f5z
Z γ :	h1z, h2z, h3z, h4z, h1g, h2g, h3g, h4g
For the GoSam matrix element	:
WW :	g1g, kg, g4g, g5g, lg, ktg, ltg, g1z, kz, g4z, g5z, lz, ktz, ltz
WZ :	g1z, kz, g4z, g5z, lz, ktz, ltz
W γ :	g1g, kg, g4g, g5g, lg, ktg, ltg
ZZ :	f4g, f4z, f5g, f5z
Z γ :	h1z, h2z, h3z, h4z, h1g, h2g, h3g, h4g

The couplings must be specified with opening and closing quotation marks and parentheses and with commas between coupling values, eg. "(0., 1., ..., N.)"

The case choices are a to e, the default being a. This case calculates the next-to-leading order corrections to the leading order amplitude. The case b reweights a $q\bar{q}$ process to the next-to-leading order induced gg process. The cases c to e are meant for diboson events, and will reweight the Standard Model couplings to the anomalous coupling (c), reweight the anomalous couplings to the Standard Model couplings (d) or reweight the real part of the anomalous couplings to the imaginary part (e). Thus a valid input for diboson reweighting would be

```

$./DiBosonStudy gosam c sherpa.root testGoSam.root "(1.,0.,0.,0.)"
while for next-to-leading order reweighting (a, b) it is only necessary to type

```

```

$./DiBosonStudy gosam a sherpa.root testGoSam.root
or
$./DiBosonStudy gosam b sherpa.root testGoSam.root

```

It is important to know that the C++ program flags on the word `sherpa` or `madgraph` in the input file name. The program is currently only capable of analysing ROOT ntuples from either of these generators, but can easily be expanded to include the generator of your choice.

List of Figures

2.1	Cube showing the fundamental theories of physics. The ones in red are yet to be constructed [1]	4
2.2	Illustrative example of Feynman diagram drawing. To the left the line styles for the various particles are shown. The middle top figure shows two fermions annihilating into a higgs then creating a pair of bosons. The middle bottom figure shows two quarks emitting two bosons and a gluon, making the process a real emission diagram, showing itself as a two boson plus a jet system. The right figure shows two quarks annihilating into a boson creating a pair of bosons. But notice here that before annihilation the quarks exchange a gluon, making the process less likely, since it is now suppressed with the coupling squared with respect to the diagram without such gluon exchange.	7
2.3	Table showing the particles of the Standard Model and their quantum numbers [5]	12
2.4	Schematic view of a proton-proton collision	18
2.5	Distributions for partons inside a proton at different momentum fractions $x = \frac{p_{parton}}{p_{proton}}$ carried by the parton [7].	19
2.6	The tadpole diagram in $\hat{\lambda}\phi^3$ theory.	23
2.7	The running of α_S at different energies [6]	24
3.1	Tree level diagrams of Z boson pair production excluding diagrams with the Higgs. The two first diagrams are the Standard Model contribution, while the last includes the TGC vertex, not allowed in the Standard Model.	28
3.2	The Feynman rules needed in the process $q\bar{q} \rightarrow ZZ \rightarrow 4l$ [3].	29
3.3	Z pair production with momenta and helicities for all particles.	30
3.4	The differential cross section per scattering angle for the various Standard Model Z helicity configurations with a fixed $u\bar{u}$ helicity configuration of $u(+)\bar{u}(-)$ and $u(-)\bar{u}(+)$ [15].	31
3.5	The differential cross section per scattering angle for the various TGC Z helicity configurations with a fixed $u\bar{u}$ helicity configuration of $u(+)\bar{u}(-)$ and $u(-)\bar{u}(+)$ and the sum of the Standard Model and TGC contributions summed [15].	32
3.6	Z pair production in a single resonant diagram.	37
3.7	The Feynman rules for QCD [3]. The t^a are the structure constants of QCD, just as $\frac{\sigma^i}{2}$ was for the Yang Mills lagrangian described in Sec. 2.1.2 and ϵ^{ijk} was for the electroweak lagrangian described in Sec. 2.2.4. The fermion lines can be seen in Sec. 3.2	38

3.8	QCD next-to-leading order contributions to diboson production without jets. The u-channel diagrams can be found by an appropriate change of boson momenta in the t-channel diagrams, thus resulting in 10 unique diagrams. . .	39
3.9	Virtual QCD corrections to single resonant Z pair production.	39
3.10	Real gluon emission contributions to $q\bar{q}$ diboson production. The u-channel diagrams can be found from the top three with an appropriate change of Z-boson momentum $q_1 \rightarrow q_2$	40
3.11	Real emission corrections to single resonant Z pair production.	40
3.12	Real (anti)quark emission contributions to $q\bar{q}$ diboson production.	41
3.13	Gluon induced Z pair production. The upper two diagrams correspond to two gluons interfering through box quark exchange, whereas in the bottom left, the virtual quarks emits the Z-bosons before connecting with the gluon. The bottom right diagram is the triangle diagram and includes the TGC vertex. .	41
5.1	Flow chart of the generic algorithm.	52
6.1	Matrix element comparison between BR and BHO generators in a $pp \rightarrow ZZ \rightarrow e^+e^-\mu^+\mu^-$ sample.	61
6.2	Matrix element comparison between GoSam and BHO generators (left) and GoSam and BR generators (right) in a $pp \rightarrow ZZ \rightarrow e^+e^-\mu^+\mu^-$ sample. . . .	61
6.3	Matrix element comparison between GoSam and BR generators in a $pp \rightarrow ZZ \rightarrow e^+e^-\mu^+\mu^-$ sample including the coupling $f_4^\gamma = 0.25$ diagram in the matrix element.	62
6.4	A BSM sample generated with SHERPA with the anomalous coupling $f_4^\gamma = 0.25$ is reweighted down to the Standard Model value of $f_4^\gamma = 0$ with the three generators BHO (upper left), BR (upper right) and GoSam (bottom) and compared to the Standard Model sample. The dashed red line indicates a ratio of one.	63
6.5	The scattering angle, $\cos\theta$ of the bosons in the center-of-mass frame of the bosons. A BSM sample with f_4^γ have been reweighted down to the Standard Model value of $f_4^\gamma = 0$ and compared to a Standard Model sample. The dashed red line indicates a ratio of one.	64
6.6	A Standard Model sample generated with SHERPA is reweighted up to the value of $f_5^Z = -0.25$ with the three generators BHO (upper left), BR (upper right) and GoSam (bottom) and compared to the BSM sample generated with SHERPA at the same coupling value. The dashed red line indicates a ratio of one.	65
7.1	Four samples showing the off-shell structure of the Z^*/γ^* pair-production in the distribution of the invariant mass of both Z's.	68
7.2	Four samples showing the off-shell structure of the Z^*/γ^* pair-production in the mass distribution of one Z.	69
7.3	p_T of the leading lepton in a SHERPA $pp \rightarrow e^+e^-\mu^+\mu^-(j)$ sample. The dashed red line indicates a ratio of one.	70
7.4	$\delta\eta$ in a SHERPA $pp \rightarrow e^+e^-\mu^+\mu^-(j)$ sample. The dashed red line indicates a ratio of one.	71
7.5	p_T of the leading lepton obtained by varying the CKKW-scale in SHERPA. Left is shown the distributions obtained with the cut at 10 GeV, right the distributions obtained with a cut of 100GeV. The dashed red line indicates a ratio of one.	72

7.6	p_T distributions of the electron and the muon generated by MCFM without the single resonant diagrams included. The dashed red line indicates a ratio of one.	73
7.7	p_T distributions of the two Z bosons generated by MCFM without the single resonant diagrams included. The dashed red line indicates a ratio of one. . .	74
7.8	p_T of the electron generated with MadGraph+MadLoop at leading and next-to-leading order.	74
7.9	The initial test of the two integral libraries implemented in GoSam. The upper two figures show the K-factor extracted from the integral libraries Golem95 (left) and Samurai (right). The bottom two show the ratio between the weights obtained with each of the generators for LO (left) and NLO (right).	76
7.10	The initial test of the two integral libraries implemented in GoSam. Shown is the p_T distribution of the electron at leading order (blue) and next-to-leading order (red). The dashed red line indicates a ratio of one.	76
7.11	The ratio of the NLO weights obtained with Golem95 and Samurai.	77
7.12	The p_T spectrum of the electron obtained with the reweighting method (left) and MCFM (right).	77
7.13	The comparison of the two ratios (LO/(LO+VIRT)) and (LO/Reweightd) obtained from MCFM and the reweighting method.	78
7.14	The χ^2 obtained when scaling the reweighted distribution in steps of 0.1%.	78
7.15	The comparison of the two ratios (LO/(LO+VIRT)) and (LO/Reweightd) obtained from MCFM and the reweighting method where the reweighting method has been scaled with 4.4%.	79
7.16	The p_T spectrum of the electron obtained with the reweighting method with a dynamic factorisation and renormalisation scale of $\mu_F = \mu_R = M_{VV}$. The dashed red line indicates a ratio of one.	79
8.1	The left figure shows a comparison of the leading order $pp \rightarrow e^+e^-\mu^+\mu^-$ sample to the sample $pp \rightarrow e^+e^-\mu^+\mu^-j$ reweighted to include next-to-leading order corrections. The right figure shows the same comparison performed in MadGraph+MadLoop. The dashed red line indicates a ratio of one and the distribution show the p_T of the electron.	84
8.2	The comparison of the two ratios (LO/NLO) and (SM/Reweightd) obtained from MadGraph+MadLoop and the reweighting method.	84
8.3	The χ^2 obtained when scaling the reweighted sample in steps of 0.001. The upper left figure includes the first bin in the fit, the upper right does not. The bottom figure shows the distribution when applying the scaling factor of 4.4%.	85
8.4	A BSM sample generated with SHERPA with the anomalous coupling $f_5^Z = -0.25$ is reweighted down to the Standard Model value of $f_5^Z = 0$ with the two generators BHO (left), BR (right) and GoSam (bottom) compared to the Standard Model sample. The dashed red line indicates a ratio of one and the distribution show the p_T of the electron.	86
8.5	A BSM sample generated with SHERPA with the anomalous coupling $f_5^Z = -0.25$ is reweighted down to the Standard Model value of $f_5^Z = 0$ with the three generators BHO (upper left), BR (upper right) and GoSam (bottom) and compared to the Standard Model sample after the selection cuts given in Table 8.3 on page 87. The dashed red line indicates a ratio of one. The distribution show the p_T of the electron.	87
8.6	The distribution show the p_T of the electron in the leading order sample (blue) and in the real emission sample (red) both with TGC coupling $f_5^Z = -0.25$. The dashed red line indicates a ratio of one.	88

8.7	The distribution show the p_T of the electron in the real emission sample (blue) and in the reweighted sample (red) with a nonzero value of f_5^Z coupling and the dashed red line indicates a ratio of one.	89
8.8	The distribution show the p_T of the electron in the real emission sample (blue) and in the reweighted sample (red). The reweighted sample now includes the full next-to-leading order contributions to the TGC sample (3) from Table 8.1. The dashed red line indicates a ratio of one.	90
8.9	The distribution show the M_{VV} spectrum of the two bosons in the real emission sample (blue) and in the reweighted sample (red). The reweighted sample now includes the full next-to-leading order contributions to the TGC sample (3) from Table 8.1. The dashed red line indicates a ratio of one.	91
8.10	The distribution show the M_{VV} spectrum of the two bosons in the real emission sample (blue) and in the reweighted sample (red). The left figure shows the sample with only f_5^Z being non-zero, the right the TGC sample (3) from Table 8.1. The dashed red line indicates a ratio of one.	92
A.1	Matrix element comparison between GoSam and BR generators in a $pp \rightarrow ZZ \rightarrow e^+e^-\mu^+\mu^-$ sample including the coupling $f_4^Z = 0.25$ diagram in the matrix element.	iv
A.2	Matrix element comparison between GoSam and BR generators in a $pp \rightarrow ZZ \rightarrow e^+e^-\mu^+\mu^-$ sample including the coupling $f_5^\gamma = 0.25$ diagram in the matrix element.	iv
A.3	Matrix element comparison between GoSam and BR generators in a $pp \rightarrow ZZ \rightarrow e^+e^-\mu^+\mu^-$ sample including the coupling $f_5^Z = 0.25$ diagram in the matrix element.	v

List of Tables

2.1	List of particle properties from [6]. - indicates no measurements has been made.	13
3.1	The coefficients C_L, C_R in different interactions. Here $g_f^- = \frac{I_3 - \sin^2 \theta_W Q}{\sin \theta_W \cos \theta_W}$, $g_f^+ = -\frac{\sin \theta_W Q}{\cos \theta_W}$.	29
3.2	The coefficients $A_{\lambda_1, \lambda_2}^\sigma, B_{\lambda_1, \lambda_2}^\sigma$ from the ZZ production amplitude [14] and the coefficients $l_{\lambda_1}^\rho, l_{\lambda_2}^\rho$ from the Z decay amplitude at different helicity combinations [13]. Notice the factor of i on the f_4^V couplings. This is responsible for the coupling being CP-violating and hence they will not interfere with the Standard Model. The couplings f_5 are CP-conserving and will thus interfere with the Standard Model.	33
5.1	The time it takes GoSam to create and compile the process tar balls. - indicates that at the writing of the thesis, the process was not done yet.	56
5.2	Compiling time for the test programs used in the thesis.	57
5.3	Compiling time for the test programs used in the thesis. A subset of 1000 events was reweighted from $f_4^\gamma = 0.25$ to $f_4^\gamma = 0$ (from LO to NLO) for each matrix element generator.	57
6.1	The SHERPA input	60
6.2	The SHERPA cuts	60
7.1	The cross sections obtained with MCFM when varying the factorisation and renormalisation scales.	75
7.2	The cross sections obtained with the reweighting method when varying the factorisation and renormalisation scales.	79
7.3	The cross sections obtained with the reweighting method when varying the factorisation and renormalisation scales.	80
7.4	The squared difference in cross sections obtained with the reweighting method when varying the PDF eigenvectors and the total uncertainty due to PDF choice.	81
8.1	The SHERPA input	83
8.2	The cross sections obtained with the reweighting method when varying the factorisation and renormalisation scales.	85
8.3	The reweighting cuts	87
8.4	The cross sections obtained with the reweighting method when varying the factorisation and renormalisation scales.	90

8.5	The cross sections obtained with the reweighting method when varying the factorisation and renormalisation scales.	91
-----	--	----

Bibliography

- [1] http://abyss.uoregon.edu/~js/images/physics_cube.gif.
- [2] C. Burgess and G. Moore. *The Standard Model, A Primer*. 2007.
- [3] M. Böhm, A. Denner, and H. Joos. *Gauge Theories of the Strong and Electroweak Interaction*. 3rd edition edition, 2001.
- [4] M.E. Peskin and D.V. Schroeder. *An Introduction to Quantum Field Theory*. 1995.
- [5] http://en.wikipedia.org/wiki/Standard_Model.
- [6] <http://pdg.lbl.gov/2012/figures/asq-2011.eps>.
- [7] D. Green. *High PT Physics at Hadron Colliders*. 2005.
- [8] Personal communications with Peter Hansen.
- [9] Cullen et. al. Automated one-loop calculations with gosam. *arXiv:1111.2034v2 [hep-ph]*, 2012.
- [10] Binoth et. al. Golem95: A numerical program to calculate one-loop tensor integrals with up to six external legs. *Comp. Phys. Com.*, (180):2313–2330, 2009.
- [11] Mastrolia et. al. Scattering amplitudes from unitarity-based reduction algorithm at the integrand-level. *arXiv1006.0710v1 [hep-ph]*:, 2010.
- [12] Denner et. al. Electroweak radiative corrections to $e^+e^- \rightarrow ww \rightarrow 4$ fermions in double-pole approximation - the racoonww approach. *arXiv:hep-ph/0006307v1*, 2000.
- [13] Hagiwara et. al. Probing the weak sector in $e^+e^- \rightarrow w^+w^-$. *Nucl. Phys. B.*, (282):253–307, 1987.
- [14] Gounaris et. al. Signatures of the anomalous $z\gamma$ and zz production at the lepton and hadron colliders. *arXiv:hep-ph/9910395v5*, 2000.
- [15] K. Gregersen. Ph.d. thesis. 2013.
- [16] Gounaris et. al. Off-shell structure of the anomalous z and γ self-couplings. *arXiv:hep-ph/0005269v5*, 1999.
- [17] D0 Collaboration. Studies of gauge boson pair production and trilinear couplings. *Phys. Rev. D.*, (56):6742–6778, 1997.

- [18] Bierweiler et. al. Vector-boson pair production at the lhc to order $(\alpha(\text{ew}))$ cubed accuracy. *arXiv:1305.5402v1[hep-ph]*, 2013.
- [19] Dixon et. al. Helicity amplitudes for $\mathcal{O}(\alpha(s))$ production of ww , wz , zz , $w\gamma$ or $z\gamma$ pairs at hadron colliders. *arXiv:hep-ph/9803250v1*, 1998.
- [20] Personal communications with Gavin Cullen.
- [21] <https://sherpa.hepforge.org/trac/wiki/MonteCarloGenerators>.
- [22] Riley et. al. *Mathematical methods for physics and engineering*. 2006.
- [23] R. Kleiss and R Pittau. Weight optimisation in multichannel monte carlo. *arXiv:hep-ph/9405257v2*, 1994.
- [24] Catani et. al. A general algorithm for calculating jet cross sections in nlo qcd. *arXiv:hep-ph/9605323v3*, 1997.
- [25] Binoth et. al. A proposal for a standard interface between monte carlo tools and one-loop programs. *Comp. Phys. Com.*, (181):1612–1622, 2010.
- [26] Gleisberg et. al. Event generation with sherpa 1.1. *arXiv:0811.4622v1 [hep-ph]*, 2008.
- [27] Alwall et. al. Madgraph 5: Going beyond. *arXiv:1106.0522v1 [hep-ph]*, 2011.
- [28] Hirschi et. al. Automation of one-loop qcd corrections. *arXiv:1103.0621v1 [hep-ph]*, 2011.
- [29] Christensen et. al. Feynrules - feynman rules made easy. *arXiv:0806.4194v1 [hep-ph]*, 2008.
- [30] A.V. Semenov. Lanhep - a package for the automatic generation of feynman rules in field theory. version 3.0. *arXiv:0805.0555v1 [hep-ph]*, 2008.
- [31] Sjostrand et. al. Pythia 6.4 physics and manual. *JHEP*, 05:26, 2006.
- [32] Sjostrand et. al. A brief introduction to pythia 8.1. *arXiv:0710.3820*, 2008.
- [33] Aquino et. al. Aloha: Automatic libraries of helicity amplitudes for feynman diagram computations. *arXiv:1108.2041v2 [hep-ph]*, 2012.
- [34] <https://amcatnlo.web.cern.ch/>.
- [35] J.M Campbell and R.K. Ellis. An update on vector boson pair production at hadron colliders. *arXiv:hep-ph/9905386v2*, 1999.
- [36] Baur et. al. *Phys. Rev. D.*, 48:5140, 1993.
- [37] Baur et. al. Probing neutral gauge boson self-interactions in zz production at hadron colliders. *arXiv:hep-ph/0008063v1*, 2000.
- [38] The GoSam Collaboration. Gosam manual. <http://www.hepforge.org/archive/gosam/gosam-1.0.pdf>, 2012.
- [39] <http://hepforge.cedar.ac.uk/lhapdf/>.
- [40] <http://www.nikhef.nl/~form/>.
- [41] Thomas Reiter. Optimising code generation with haggies. *arXiv:0907.3714v2 [hep-ph]*, 2009.

- [42] Pumplin et. al. New generation of parton distributions with uncertainties from global qcd analysis. *arXiv:hep-ph/0201195v3*, 2002.
- [43] Personal communications between Steffen Schumann and Jørgen Beck Hansen.
- [44] Artoisenet et. al. Automation of the matrix element reweighting method. *arXiv:1007.3300v2 [hep-ph]*, 2011.